MATTER-LIGHT ENTANGLEMENT WITH COLD ATOMIC ENSEMBLES

A Thesis
Presented to
The Academic Faculty

by

Shau-Yu Lan

In Partial Fulfillment
of the Requirements for the Degree
Doctor of Philosophy in the
School of Physics

Georgia Institute of Technology
May 2009

MATTER-LIGHT ENTANGLEMENT WITH COLD ATOMIC ENSEMBLES

Approved by:

Professor Alex Kuzmich, Advisor
School of Physics
Georgia Institute of Technology

Professor Chandra Raman
School of Physics
Georgia Institute of Technology

Professor T. A. Brain Kennedy
School of Physics
Georgia Institute of Technology

Professor David S. Citrin
School of Electrical and Computer Engineering
Georgia Institute of Technology

Professor Michael Chapman
School of Physics
Georgia Institute of Technology

Date Approved: December, 4, 2008

To my parents

ACKNOWLEDGEMENTS

Here, I would like to take this opportunity to express my appreciation to those who supported me throughout my Ph.D. career.

First I would like to thank my advisor Prof. Alex Kuzmich for his invaluable advice and constant encouragement. His ideas and passion for the research were a great source of inspiration for me.

Next, I want to thank Dr. Thierry Chanelière, Dr. Dzmitry Matsukevich, and Dr. Stewart Jenkins who taught me much of what I know about AMO physics. I am grateful for their help, as this work would not be possible without it.

A special thank you goes to Corey Campbell, Ran Zhao, and Alexander Radnaev, who worked closely with me on the experiments. It was a joy working with them. I would also like to express my appreciation for insightful discussions with and aid from other labmates, past and present, including Ryan Smith, Tamar Neumann, Andrew Cheung, Mishkat Bhattacharya, Yaroslav Dudin, and David Naylor.

I also want to acknowledge our theoretical collaborators, Prof. Brian Kennedy, Austin Collins, and Hsiang-Hua Jen for fruitful discussions.

Finally, I would like to express immense gratitude and appreciation to my parents, Kuo-Lien Lan and Chou-Mei Liao, my brother, Dr. Chao-Chieh Lan, and all of my family for always supporting and encouraging me in my education.

TABLE OF CONTENTS

LIST OF TABLES

LIST OF FIGURES

SUMMARY

In this thesis I present the investigations of matter-light entanglement in cold atomic samples. Particularly, entanglement of mixed species ensembles and bichromatic light fields is proposed and demonstrated experimentally. This approach avoids the use of two interferometrically separate paths for qubits entanglement distribution. I also present the first implementation of multiplexed quantum memory, and experimentally demonstrate entanglement involving arbitrary pairs of elements within this memory array. Finally, quantum interference of electromagnetic fields emitted by remote quantum memory elements separated by 5.5 m is realized.

CHAPTER I

INTRODUCTION

One of the fundamentals of quantum mechanics is the superposition principle, which states that a linear superposition of solutions to the Schrödinger equation is also a solution. Though at first glance it may seem simple, the superposition principle has amazing consequences. One of them is quantum entanglement, to which this thesis is dedicated. Phenomenologically speaking, quantum entanglement is an effect in which the states of two or more systems are coupled so that no system can be described without accounting for its counterparts, even if they are spatially separated. This phenomenon has interesting philosophical aspects and real life applications. In this introductory chapter I will give a brief history of entanglement, provide its quantum mechanical description, and discuss its applications to cryptography, particularly quantum repeaters with atomic ensembles based on the so-called DLCZ protocol.

1.1 Brief History of Entanglement

In the early development of quantum mechanics, Einstein, Podolsky, and Rosen (EPR) came up with a paradoxical thought experiment (Gedankenexperiment) to show the incompleteness of quantum theory. They posed the question, *"Can quantum-mechanical description of physical reality be considered complete?"* [1]. They claimed that because the signal between two objects cannot propagate faster than the speed of light, the measurement performed on the first object cannot instantaneously influence the measurement outcome of the other, unless there is some *"element of reality"*(local hidden variables) which cannot be explained by quantum mechanics. In 1964, Bell used local hidden variables to show mathematically that the results predicted by quantum mechanics could not be explained by any theory which preserved locality

[2]. The result since has been named Bell's inequality. It limits the correlations of the objects that have interacted and then separated. Violation of Bell's inequality confirms the non-local properties of quantum mechanics.

The first experimental tests of local hidden variables were carried out using radiative cascade transitions [3, 4]. Polarization correlations of the emitted photon pairs were measured. Later on, a more efficient method of parametric down conversion (PDC) in nonlinear crystals was developed [5, 6]. Violation of Bell's inequality has also been observed in several other systems, such as atomic ensembles and ions ([7, 8] and references therein).

Although the experiments described above can violate Bell's inequality, they are still not ideal. There are two main loopholes: detection and locality. The detection loophole is the possibility that a violation of Bell's inequality could be mimicked by low detection and collection efficiency. The locality loophole arises if the separation between the measured systems is not sufficient to prevent information exchange during the experiment. The detection loophole was closed in a trapped ion system [9], and the locality loophole was closed in photon systems [10, 11]. Simultaneous closure of these two loopholes in a single experiment remains an outstanding goal [12].

In the 1980s, quantum entanglement began attracting attention of many physicists, mathematicians, and computer engineers with the promise of dramatically new technologies. In particular, it has the potential to provide more secure transmission of messages and exponentially faster computing [13].

1.2 Qubits and Entanglement

The superposition principle in QM leads to the concept of a quantum bit (qubit) as a new information carrier. The unit of classical information is a bit, which is a system in a state 0 *or* 1; on the contrary, a unit of quantum information can be in the states

0 and 1 *simultaneously*:

$$|\Psi\rangle = \alpha|0\rangle + \beta|1\rangle, \quad \text{where} \quad |\alpha|^2 + |\beta|^2 = 1. \tag{1}$$

This coherent superposition of quantum states with *complex* probability amplitudes α and β provide rich possibilities for quantum computation and quantum communication. States $|0\rangle$ and $|1\rangle$ could be encoded in many ways: spin, polarization, frequency, time, squeezing, etc. In the following, I will use spin 1/2 particles as an example and define the orthogonal basis with $|\uparrow\rangle = |1\rangle$ and $|\downarrow\rangle = |0\rangle$.

An intriguing phenomenon occurs when two qubits, $|\Psi\rangle_A$ and $|\Psi\rangle_B$, are linked to result in a state $|\Psi\rangle_{AB}$ that cannot be factorized as a tensor product of single particle states:

$$|\Psi\rangle_{AB} = \frac{1}{\sqrt{2}}(|\uparrow\rangle_A|\downarrow\rangle_B - |\downarrow\rangle_A|\uparrow\rangle_B) \neq |\Psi\rangle_A \otimes |\Psi\rangle_B. \tag{2}$$

Such a state is called an entangled state of two qubits. A measurement performed on one of the qubits will instantaneously label the other qubit with a value opposite to the probabilistic outcome of the first measurement; without measurement, neither qubit possesses a definite value.

1.3 Bell's Inequality

There are many forms of Bell's theorem. In this section, I will formulate the Clauser, Horne, Shimony, and Holt (CHSH) type Bell's theorem [14], relying on Refs. [15] and [16] to quantify the degree of entanglement. The inequality will be used to verify entanglement in the experiments discussed throughout this thesis.

Consider a source emitting entangled pairs of qubits observed by A and B, respectively, as shown in Fig. 1. The observers A and B perform measurements on their particles in one of the two measurement bases defined by the vectors $\vec{a}$ and $\vec{a}'$ and $\vec{b}$ and $\vec{b}'$, respectively. We normalize the two possible eigenvalues of some observable and assign the value +1 and -1, individually. In the theories of supplementary parameters, all measurement results are determined by a set of unknown local hidden

variables λ. According to the theories, even for identically prepared particles, the corresponding hidden variables are in an unknown statistical distribution $p(\lambda)$ of possible values λ which results in the probabilistic nature of measurements in quantum mechanics. The normalization condition of the probabilities requires

$$\int p(\lambda)d\lambda = 1. \tag{3}$$

The observables $A_{\vec{a}}$, $A_{\vec{a'}}$ and $B_{\vec{b}}$, $B_{\vec{b'}}$ describe the measurement outcomes for observers A and B, respectively. Based on the locality assumption, the outcome of measurement A (B) is only determined by the value of the hidden variables λ and the analyzer setting $\vec{a}$ $(\vec{b})$, $\vec{a}'$ $(\vec{b'})$, and not by the analyzer setting of the observer B (A). Therefore, the expectation value of the joint measurement $A_{\vec{a}}(\lambda) \cdot B_{\vec{b}}(\lambda)$ is given by

$$E(\vec{a}, \vec{b}) = \int A_{\vec{a}}(\lambda) B_{\vec{b}}(\lambda) p(\lambda) d\lambda. \tag{4}$$

We now use another analyzer setting $\vec{a}'$ and $\vec{b'}$ and introduce the parameter S

$$\begin{aligned} S(\vec{a}, \vec{a'}, \vec{b}, \vec{b'}) &\equiv E(\vec{a}, \vec{b}) - E(\vec{a}, \vec{b'}) - E(\vec{a'}, \vec{b}) - E(\vec{a'}, \vec{b'}) \\ &= \int A_{\vec{a}}(\lambda) B_{\vec{b}}(\lambda) p(\lambda) d\lambda - \int A_{\vec{a}}(\lambda) B_{\vec{b'}}(\lambda) p(\lambda) d\lambda \\ &\quad - \int A_{\vec{a'}}(\lambda) B_{\vec{b}}(\lambda) p(\lambda) d\lambda - \int A_{\vec{a'}}(\lambda) B_{\vec{b'}}(\lambda) p(\lambda) d\lambda \\ &= \int A_{\vec{a}}(\lambda)(B_{\vec{b}}(\lambda) - B_{\vec{b'}}(\lambda)) p(\lambda) d\lambda \\ &\quad - \int A_{\vec{a'}}(\lambda)(B_{\vec{b}}(\lambda) + B_{\vec{b'}}(\lambda)) p(\lambda) d\lambda. \end{aligned} \tag{5}$$

Since the measurement outcomes are $A_{\vec{a}}(\lambda) = \pm 1$ and $B_{\vec{b}}(\lambda) = \pm 1$, the above equation can be written as an inequality

$$-2 \leq S(\vec{a}, \vec{a'}, \vec{b}, \vec{b'}) \equiv E(\vec{a}, \vec{b}) - E(\vec{a}, \vec{b'}) - E(\vec{a'}, \vec{b}) - E(\vec{a'}, \vec{b'}) \leq 2. \tag{6}$$

This is the CHSH (or BCHSH) inequality, *i.e.*, Bell's inequality as generalized by Clauser, Horne, Shimony, and Holt.

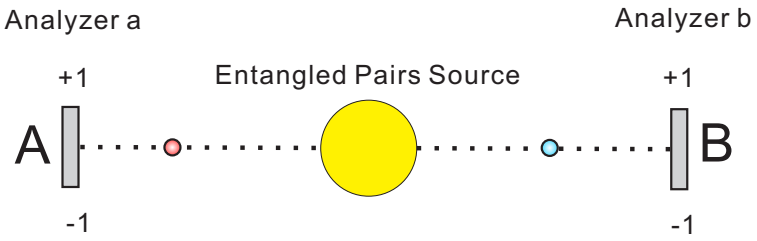

Figure 1: Einstein-Podolsky-Rosen-Bohm experiment with photons. The two photons emitted in the state $|\Phi\rangle$ are analyzed by linear polarizers in orientations a and b. One can measure the probabilities of single or joint detections in the output channels of the polarizers.

Consider more specifically the quantum state

$$|\Phi\rangle = \frac{1}{\sqrt{2}}(\hat{a}_+^\dagger \hat{b}_+^\dagger + \hat{a}_-^\dagger \hat{b}_-^\dagger)|0\rangle, \tag{7}$$

where $\hat{a}_+^\dagger$, $\hat{b}_+^\dagger$, $\hat{a}_-^\dagger$, and $\hat{b}_-^\dagger$ are the creation operators for the corresponding orthogonal states. We are free to rotate the measurement bases by the angles ϕ_1 and ϕ_2. Consider the following orthogonal transformation:

$$\begin{aligned}
\hat{a} &= \hat{a}_+ \cos\phi_1 + \hat{a}_- \sin\phi_1; \\
\hat{a}^\perp &= -\hat{a}_+ \sin\phi_1 + \hat{a}_- \cos\phi_1; \\
\hat{b} &= \hat{b}_+ \cos\phi_2 + \hat{b}_- \sin\phi_2; \\
\hat{b}^\perp &= -\hat{b}_+ \sin\phi_2 + \hat{b}_- \cos\phi_2.
\end{aligned} \tag{8}$$

We define the correlation function E:

$$E(\phi_1,\phi_2) = \frac{C(\phi_1,\phi_2) - C(\phi_1,\phi_2^\perp) - C(\phi_1^\perp,\phi_2) + C(\phi_1^\perp,\phi_2^\perp)}{C(\phi_1,\phi_2) + C(\phi_1,\phi_2^\perp) + C(\phi_1^\perp,\phi_2) + C(\phi_1^\perp,\phi_2^\perp)}, \tag{9}$$

where

$$\begin{aligned}
C(\phi_1,\phi_2) &= \eta^2 \langle : \hat{a}^\dagger \hat{a} \hat{b}^\dagger \hat{b} : \rangle \\
C(\phi_1,\phi_2^\perp) &= \eta^2 \langle : \hat{a}^\dagger \hat{a} \hat{b}^{\perp\dagger} \hat{b}^\perp : \rangle \\
C(\phi_1^\perp,\phi_2) &= \eta^2 \langle : \hat{a}^{\perp\dagger} \hat{a}^\perp \hat{b}^\dagger \hat{b} : \rangle \\
C(\phi_1^\perp,\phi_2^\perp) &= \eta^2 \langle : \hat{a}^{\perp\dagger} \hat{a}^\perp \hat{b}^{\perp\dagger} \hat{b}^\perp : \rangle,
\end{aligned} \tag{10}$$

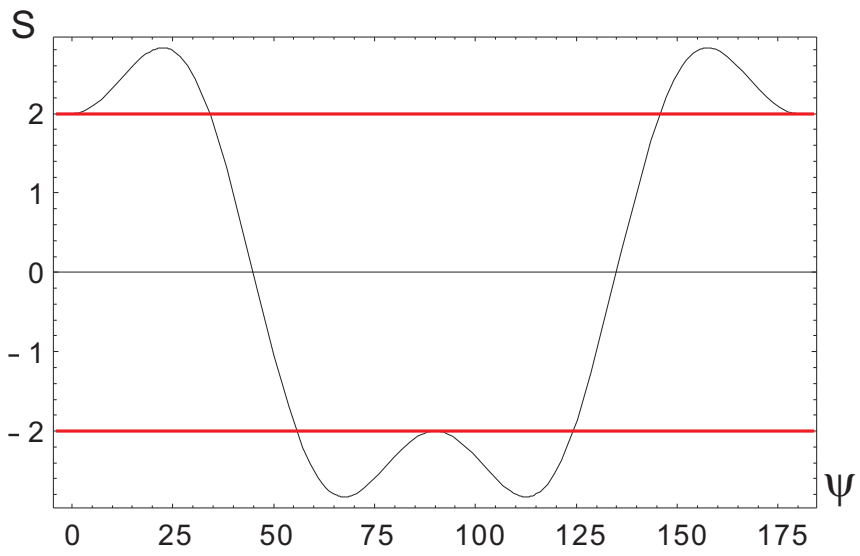

Figure 2: Bell parameter S as function of ψ The conflict with Bell's inequality happens when $|S| > 2$, and it is maximized for the sets of orientations $\psi = \pm\frac{\pi}{8}$ and $\psi = \pm\frac{3\pi}{8}$

.

$\phi^{\perp}_{1[2]} = \phi_{1[2]} + \pi$, and η is the detection efficiency. Using Eqs. (7) and (8), the correlation function can be represented as

$$E(\phi_1, \phi_2) = \cos[2(\phi_1 - \phi_2)], \tag{11}$$

where $\phi_1 - \phi_2$ represents the angle between the measurement bases. The parameter S becomes

$$S = \cos[2(\phi_1 - \phi_2)] - \cos[2(\phi_1 - \phi'_2)] - \cos[2(\phi'_1 - \phi_2)] - \cos[2(\phi'_1 - \phi'_2)]. \tag{12}$$

This function has three independent parameters. In order to analyze the maximum conflict of the parameter S, we set the three partial derivatives of S equal to zero. We find that

$$(\phi_2 - \phi_1) = (\phi'_1 - \phi_2) = (\phi'_1 - \phi'_2) \equiv \psi \tag{13}$$

and

$$\sin\psi = \sin 3\psi. \tag{14}$$

The parameter S becomes

$$S = 3\cos 2\psi - \cos 6\psi. \tag{15}$$

The maximum conflict occurs when

$$\psi = \pm\frac{\pi}{8}, \qquad S_{MC} = 2\sqrt{2}; \tag{16}$$

$$\psi = \pm\frac{3\pi}{8}, \qquad S_{MC} = -2\sqrt{2}. \tag{17}$$

Fig. 2 shows the Bell parameter S as a function of ψ. There are many sets of orientations that conflict with Bell's inequality.

The characterization of entanglement using the violation of Bell's inequality is not only of fundamental interest, but can also has practical applications, such as quantum cryptography based on entanglement distribution.

1.4 Quantum Cryptography

Quantum communication is a process of transmission of quantum information. Its important application is distribution of keys for classical cryptography. Unlike traditional key distribution by a human courier, where there is no way to detect eavesdropping, the quantum scheme allows for eavesdropping detection; according to the no-cloning theorem, performing a measurement on the transmitted information will unavoidably alter the state [17]. This can be discovered by the remote parties in a subsequent public communication, and hence, eavesdropping is detected.

The realization of quantum cryptography can be illustrated with the BB84 protocol (Charles H. Bennett and Gilles Brassard (1984)), which employs a single qubit to distribute a key [18]. If Alice wants to share a secret key with Bob, she sends a stream of single photon qubits, which are encoded in two polarization bases ($0^\circ - 0_1$, $90^\circ - 1_1$, $45^\circ - 0_2$, $135^\circ - 1_2$, where the index represents the basis number) arbitrarily. Bob measures the polarization of the photon stream in randomly selected measurement bases. Then, they compare the measurement bases in the public channel. If the bases coincide, then the measured state 0 or 1 is considered as one bit of the shared key. This key can be used to perform classical cryptography.

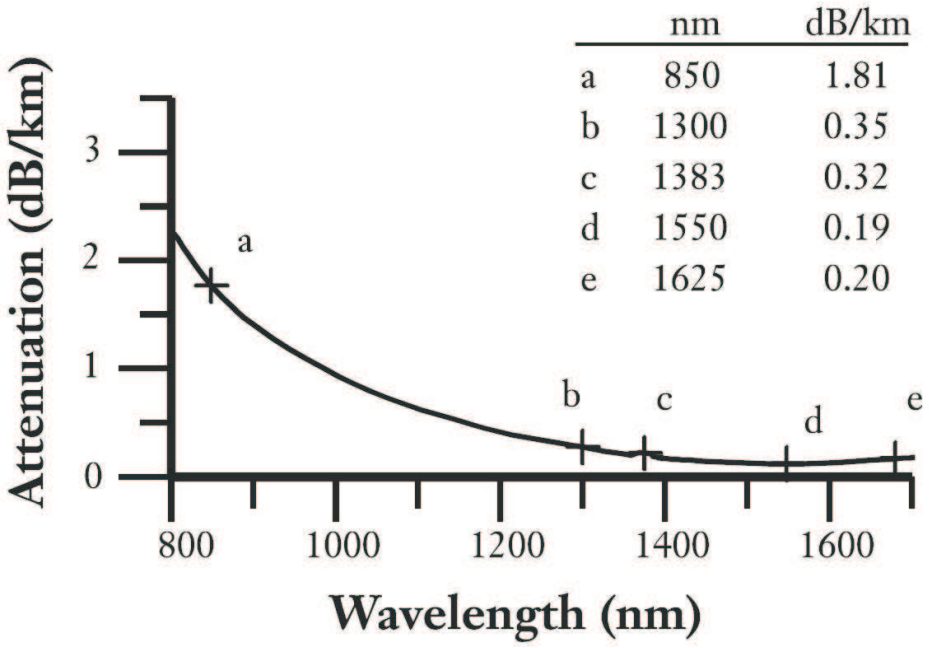

Figure 3: Attenuation spectrum of a standard single-mode fiber [19].

If we want to transmit a single photon from site A to site B, due to the fiber loss the successful probability will be $p(l) = e^{-l/\mathrm{L}}$, where L is the absorption length of the fiber. The average number of trials to transmit a photon successfully is

$$n(l) = \frac{1}{p(l)} = e^{l/\mathrm{L}}. \tag{18}$$

For instance, as shown in Fig. 3, the attenuation of a 1550 nm wavelength photon in an optical fiber is about 0.19 dB/km, corresponding to an absorption length of 23 km. The average number of trials to send the photon over 1000 km without being absorbed is on the order of 10^{19}! As a result of the inevitable signal losses in optical fibers, the communication rate decreases exponentially with distance.

The distance over which quantum keys can be distributed can be extended using the Eckert protocol, based on entanglement [20]. Alice and Bob perform the measurement on one of the two entangled qubits respectively. As in BB84 protocol, the two measurement bases are selected randomly and they compare their bases in public

channel. The key is established when both of them use the same measurement basis. Unlike direct transmission of a qubit, which is limited by the absorption length, entanglement can be established without this limitation using an operation called entanglement swapping. For example, if we prepare two pairs (p1, p2) of entangled qubits and then perform a measurement on two qubits: one is from pair p1, and the other from pair p2. This measurement projects the remaining qubits, whose separation distance can be twice that of each pair, to an entangled state [21, 22] as shown in Fig. 4. To prove this, consider two qubits defining a four-dimensional Hilbert space, where a possible basis is defined by the four separable product states $|\uparrow\rangle_A|\uparrow\rangle_B$, $|\uparrow\rangle_A|\downarrow\rangle_B$, $|\downarrow\rangle_A|\uparrow\rangle_B$, and $|\downarrow\rangle_A|\downarrow\rangle_B$. Alternatively, a basis can be defined by four entangled states (also termed Bell states) [23]:

$$|\Psi^+\rangle = \frac{1}{\sqrt{2}}(|\uparrow\rangle_A|\downarrow\rangle_B + |\downarrow\rangle_A|\uparrow\rangle_B) \tag{19}$$

$$|\Psi^-\rangle = \frac{1}{\sqrt{2}}(|\uparrow\rangle_A|\downarrow\rangle_B - |\downarrow\rangle_A|\uparrow\rangle_B) \tag{20}$$

$$|\Phi^+\rangle = \frac{1}{\sqrt{2}}(|\uparrow\rangle_A|\uparrow\rangle_B + |\downarrow\rangle_A|\downarrow\rangle_B) \tag{21}$$

$$|\Phi^-\rangle = \frac{1}{\sqrt{2}}(|\uparrow\rangle_A|\uparrow\rangle_B - |\downarrow\rangle_A|\downarrow\rangle_B), \tag{22}$$

where $|\Psi^-\rangle$ is the antisymmetric singlet state and the other three entangled states correspond to the symmetric triplet states. Each of the Bell states is a maximally entangled state and results in the maximum possible violation of Bell's inequality.

Consider two entangled pairs of particles 1-2 and 3-4 in the following state:

$$\begin{aligned} |\Psi\rangle_{1234} &= |\Psi^-\rangle_{12} \otimes |\Psi^-\rangle_{34} \\ &= \frac{1}{2}(|\uparrow\rangle_1|\downarrow\rangle_2 - |\downarrow\rangle_1|\uparrow\rangle_2)(|\uparrow\rangle_3|\downarrow\rangle_4 - |\downarrow\rangle_3|\uparrow\rangle_4), \end{aligned} \tag{23}$$

where the state of pair 1-2 can still be factorized from the state of pair 3-4. If we rearrange the above equation with the Bell states, the joint state can be rewritten as

$$\begin{aligned} |\Psi\rangle_{1234} &= \frac{1}{2}(|\Psi^+\rangle_{14}|\Psi^+\rangle_{23} - |\Psi^-\rangle_{14}|\Psi^-\rangle_{23} \\ &\quad -|\Phi^+\rangle_{14}|\Phi^+\rangle_{23} + |\Phi^-\rangle_{14}|\Phi^-\rangle_{23}). \end{aligned} \tag{24}$$

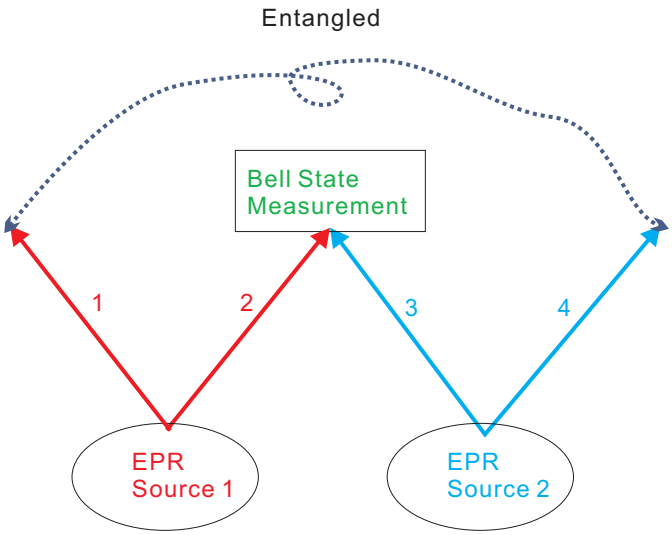

Figure 4: Principle of entanglement swapping. Two EPR sources produce two pairs of entangled photons, pair 1-2 and pair 3-4. Photons 2 and 3 are subjected to a Bell-state measurement. This results in a projection of the other two photons, 1 and 4, onto an entangled state.

We can do the measurement in the Bell state basis between particles 2 and 3 which automatically projects the states of particles 1 and 4 onto one of the four entangled Bell states described above, depending on the measurement outcome. This protocol is called "entanglement swapping" or "entanglement connection."

Based on entanglement swapping, the concept of the quantum repeater was proposed to overcome fiber loss and enable quantum communication over longer distances [24, 25]. Unlike in classical communication, one cannot use a middle station to reconstruct the state because no-cloning theorem prohibits manipulation of an arbitrary quantum state [17]. The idea of the quantum repeater is to insert quantum memory elements into the quantum channel every attenuation length or so and create qubits in each element. Entanglement between neighboring pairs of qubits can be generated efficiently, as light is not appreciably absorbed between them. Consider a serial link consisting of quantum memory elements with the dividing points C_1, C_2, C_3.....C_{N-1} between A and B as shown in Fig. 5 are connected by an optical fiber. The first

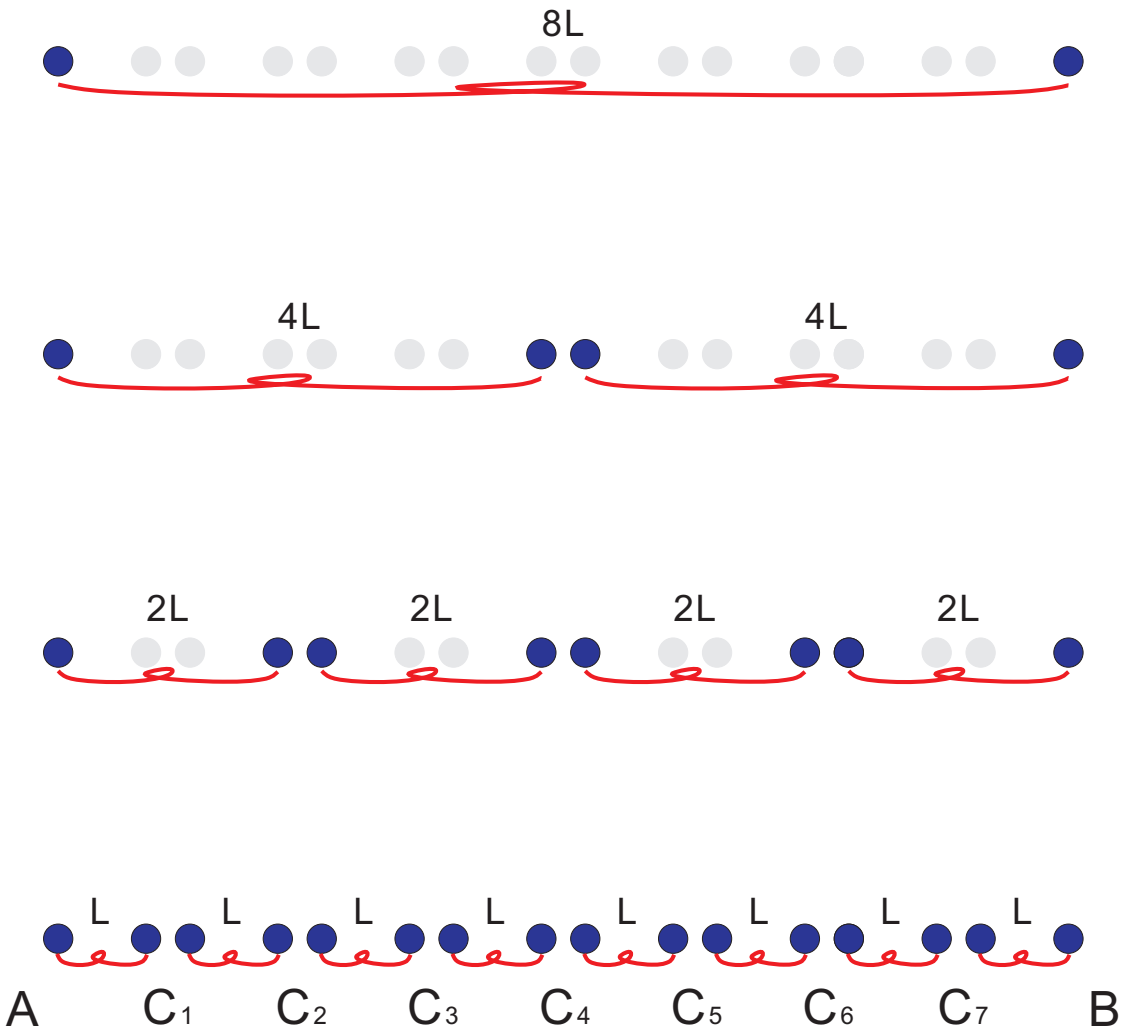

Figure 5: Architecture of quantum repeater. L is the fundamental distance of the adjacent nodes which is defined by the absorption length of fiber.

step of the quantum repeater is to generate entanglement between adjacent memory elements and then simultaneously perform appropriate joint measurements on neighboring internal qubit pairs at C_1, C_3, ..., C_{N-1} to double the entangled length. This leaves us with longer pairs (A-C_2),(C_2-C_4), ...,(C_{N-2}-B). Next we connect simultaneously these longer pairs at C_2, C_6,...,C_{N-2}. In this way, we iterate the procedure to higher and higher levels until we reach the outermost qubits at the remote ends of the link. As a result, we have obtained a final entangled pair between A and B. The communication rate in this case scales polynomially with the distance [24, 26].

In general, a quantum information network should therefore consist of spatially separated nodes to store and process quantum information and channels to connect the nodes. Photons, ideal carriers of quantum information, can be transmitted extremely fast and interact minimally with the environment. Atoms, with the rapid development of laser cooling and trapping techniques, are excellent candidates for the storage and manipulation of qubits, because it is possible to isolate them from the environment and manipulate their internal states with laser light or external dc fields to manifest very long coherence times [27].

Important progress towards quantum communication has been made using a variety of different schemes. In atomic ensembles, the realization of coherent quantum state transfer from a matter qubit onto a photonic qubit was achieved in 2004 using a cold Rb atomic ensemble [28]. It was quickly followed by several other significant advances: efficient generation of narrowband photon pairs deep in the regime of electromagnetically induced transparency [29], Bell's inequality violation between a collective atomic qubit and a photon [30], storage and retrieval of single photons [31], collapses and revivals of quantum memory [32, 33], electromagnetically induced transparency with single-photon pulses [34], and light-matter qubit conversion and entanglement of remote atomic qubits [35]. A scheme to achieve long distance quantum communication at the absorption minimum of optical fibers, employing atomic cascade transitions, has been proposed and its critical elements experimentally verified [36]. A deterministic single-photon source based on quantum measurement, quantum memory, and quantum feedback has been proposed and demonstrated [37]. Hong-Ou-Mandel interference of photon pairs from an ensemble has been observed [38]. In addition, two remote atomic qubits have been entangled in the trapped ion system using frequency and polarization light qubits [8, 41]. In the microwave domain, single Rydberg atoms and single photons have been entangled [42]. An entangled state of a neutral atom and a near-infrared photon has been reported [43]. An approach using

photon pair sources based on parametric down-conversion and solid-state quantum memories based on controlled reversible inhomogeneous broadening is currently under investigation [78].

In a broad sense, all these developments pave the way for the realization of a distributed network of atomic qubits, linear optical elements, and single-photon detectors. Throughout this thesis, I will focus on the cold atomic ensemble-based long distance quantum communication along the lines of the Duan, Lukin, Cirac, and Zoller (DLCZ) protocol [26].

1.5 Quantum Repeater with Atomic Ensembles (DLCZ protocol)

Atomic ensembles have been used to study the connection between atomic physics and quantum optics. For example, spontaneous atomic emission can be used to generate coherent radiation [45]. Recently, the utility of optically thick atomic ensembles has been explored for multiparticle entanglement, generation of non-classical states of matter [46, 47, 48], and continuous variable quantum information processing ([49] and references therein).

Optically thick atomic ensembles are promising for quantum communication because of the collective enhancement of atom-photon interaction [50, 51, 52, 53, 54, 55, 56]. Duan, Lukin, Cirac, and Zoller (DLCZ) invented a protocol that realizes the quantum repeater architecture using atomic ensembles [26]. The DLCZ protocol utilizes N identical atoms with a pair of metastable states $|g\rangle$ and $|s\rangle$. All the atoms are prepared in the upper state $|g\rangle$. A weak pulse tuned around the transition $|g\rangle \rightarrow |e\rangle$ excites the atomic ensemble. The Raman scattered (signal) photon is emitted from the ensemble along with the transfer of the atomic state from $|g\rangle$ to $|s\rangle$ as shown in Fig. 6. The collective atomic state $\hat{S}^{\dagger}|0\rangle_a$ is strongly correlated with the signal

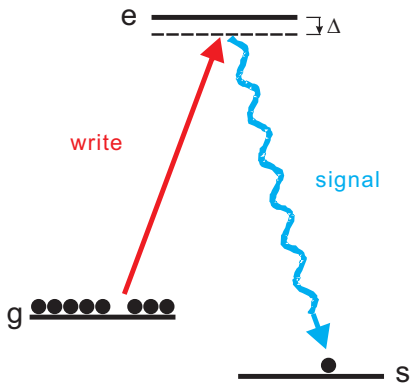

Figure 6: Write Process: All the atoms are prepared in the upper state $|g\rangle$. A weak pulse tuned around the transition $|g\rangle \rightarrow |e\rangle$ excites the atomic ensemble accompanying a Raman scattered photon which transfers the atomic state from $|g\rangle$ to $|s\rangle$.

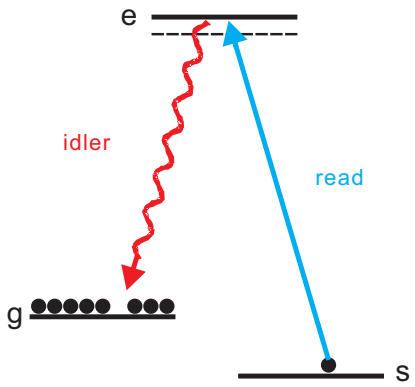

Figure 7: Read Process: A read pulse tuned on the $|s\rangle \rightarrow |e\rangle$ transition serves as the controlled field in the EIT configuration such that the atomic excitation state can be mapped into a photonic state. Due to collective enhancement, the idler photon will be emitted in the direction determined by the phase matching condition.

photon, where

$$\hat{S} = \sum_{i=1}^{N} |g_i\rangle\langle e_i| e^{i\Delta\vec{k}\cdot\vec{r_i}}, \tag{25}$$

$\Delta\vec{k} = \vec{k_w} - \vec{k_s}$ is the difference between the write and signal wavevectors, and $\vec{r_i}$ is the position of the i-th atom. The quantum state of the system is

$$|\Psi\rangle = |0\rangle_a|0\rangle_s + \sqrt{p_c}\hat{S}^\dagger\hat{a}^\dagger|0\rangle_a|0\rangle_s + O(p_c), \tag{26}$$

where $\hat{a}^\dagger$ is the creation operator of the signal field, p_c is the excitation probability, and $|0\rangle_s$ denotes the vacuum state of the signal field mode. The first term represents the

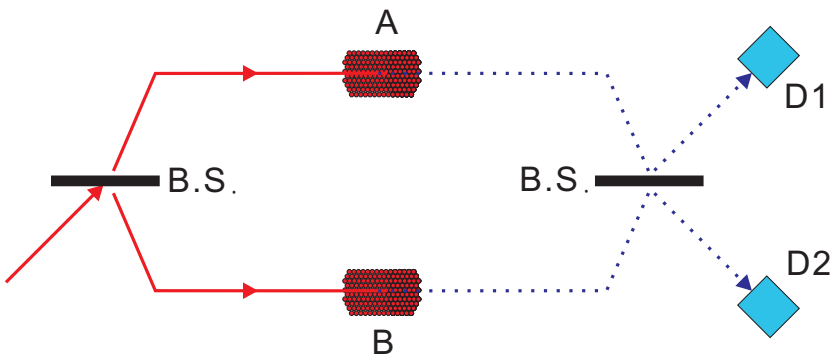

Figure 8: Set-up for generating a qubit state using two atomic ensembles A and B. The pulses after the transmission channels interfere at a 50/50 beam splitter, with the outputs detected by two single-photon detectors D1 and D2, respectively. If there is a click in D1 or D2, the process is finished and we have successfully generated entanglement between the ensembles A and B.

vacuum component and the excitation probability is sufficiently small that the higher order terms can be ignored. The mapping of the collective atomic state into a photonic state is done via the electromagnetically induced transparency (EIT) technique [56, 57, 58]. A read pulse tuned on the $|s\rangle \rightarrow |e\rangle$ transition serves as the control field in the EIT configuration, such that the atomic excitation state can be mapped into a photonic state by changing the control field intensity, as shown in Fig. 7. It also enables the idler field to propagate through the dense atomic gas.

Due to collective enhancement, the idler field is emitted in the direction determined by the phase matching condition $\vec{k_s} + \vec{k_i} = \vec{k_w} + \vec{k_r}$, where $\vec{k_r}$ and $\vec{k_i}$ are the read and idler wavevectors, respectively. The corresponding quantum state is

$$|\Psi\rangle = |0\rangle_s|0\rangle_i + \sqrt{p_c}|1\rangle_s|1\rangle_i + O(p_c), \tag{27}$$

where $|0\rangle_i$ denote, the vacuum state of the idler field mode.

We can also encode qubits into atomic ensembles and light fields. E.g., in Fig. 8 two write pulses illuminate spatially separate ensembles simultaneously and the whole system is described as $|\Psi\rangle_A \otimes |\Psi\rangle_B$. The signal fields from the two ensembles are combined on a beam splitter. If the two optical channels are symmetric, the beam

splitter erases the distinguishability of two signal photons. The detection on either beam splitter port D1 or D2 measures the superposed information from these two channels with $\hat{a}_+^\dagger \hat{a}_+$ or $\hat{a}_-^\dagger \hat{a}_-$ where $\hat{a}_\pm = \hat{a}_A \pm e^{i\varphi}\hat{a}_B$. The phase φ accounts for all the phase differences in this Mach-Zehnder type interference between two channels. Once the signal photon is detected, the quantum state becomes

$$|\Psi_\pm\rangle = \frac{(\hat{S}_A^\dagger \pm e^{i\varphi}\hat{S}_B^\dagger)}{\sqrt{2}}|0\rangle_{Aa}|0\rangle_{Ba}. \tag{28}$$

One can also encode a qubit in a single ensemble with different spin states. This leads to the polarization entanglement of signal and idler photons [30]. The effective state of the photon pairs is:

$$|\Psi\rangle_{eff} = \cos\eta|H\rangle_s|V\rangle_i + \sin\eta|V\rangle_s|H\rangle_i, \tag{29}$$

where $\cos\eta$ and $\sin\eta$ are determined by the relevant Clebsch-Gordan coefficients for the transition [59]. Another way to encode the polarization qubit with a single ensemble is by collecting two different modes of the Raman field through a polarizing beam splitter [60]. In the following chapters I will describe two ways of encoding frequency qubits in the photon pairs with nonlinear optical devices.

To realize the DLCZ quantum repeater architecture, we also need to perform the entanglement connection. Consider four atomic ensembles as shown in Fig. 9, where A2 and B1 are close by, A(B)2 is separated by A(B)1 by distance L (determined by the absorption length of fiber). After there is a signal detection for each pair of ensembles, read pulses are sent to A2 and B1. If there is a detection on either D1 or D2, the system will be projected into a joint state of ensembles A1 and B2, as in Eq. (28), and the entanglement distance is doubled. In this way, a chain of atomic ensembles can be prepared and used for a quantum repeater.

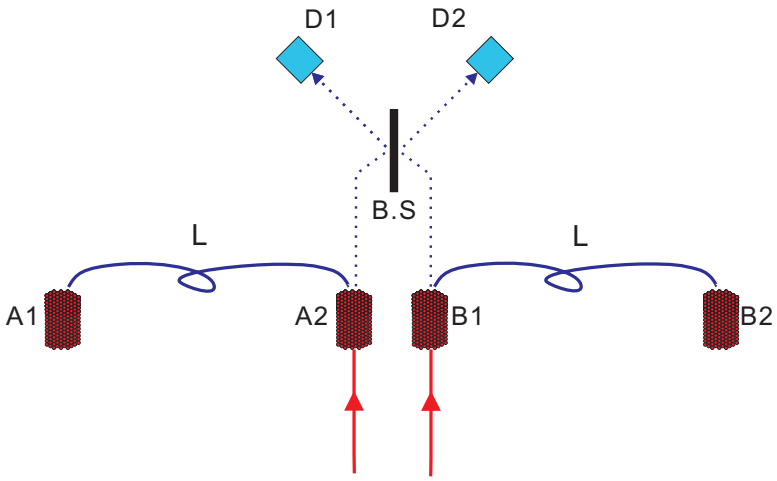

Figure 9: Set-up for entanglement connection. The read pulses are sent into nearby ensembles to convert the atomic excitations into photons. The projection measurement is made with a 50/50 beam splitter. If there is a click in either D1 or D2, an entangled state is established between A1 and B2.

1.6 Thesis Overview

This introduction has sketched the basic principles for experiments with cold atomic ensembles described in the following chapters. The second chapter will cover the details of the experimental setup, including the vacuum chamber, construction of the magneto-optical trap, and the configuration of the optics and laser. In Chapter III, I will show the first realization of a dual species matter qubit and its entanglement with a frequency-encoded photonic qubit by using co-trapped ^{85}Rb and ^{87}Rb isotopes, thereby avoiding the stringent interferometer requirement in the entanglement distribution. For a practical quantum repeater, multiple quantum elements in a single quantum node and dynamic entanglement connection will be needed, in order to obtain a realistic communication rate over long distances. Chapter IV describes the realization of a dozen memory elements in a single atomic ensemble. Additionally, matter-light entanglement with such a memory array is achieved, which shows an ability to dynamically connect different quantum elements. In Chapter V, I describe quantum interference of electromagnetic fields emitted by remote quantum memory elements.

CHAPTER II

EXPERIMENTAL TECHNIQUES

The quantum state transfer between photonic and matter-based quantum systems is an important component of this work. The retrieval efficiency of the idler field depends on the optical thickness of the atomic ensemble. The latter is proportional to the atomic density and the length of the atomic ensemble along the direction of the field propagation. In order to obtain a large value for optical thickness inside a magneto-optical trap, we construct a glass cell chamber with sizable optical access for large trapping beams. This is also convenient for beam alignment. This chapter will describe the construction of the vacuum chamber, magneto-optical trap, laser settings for co-trapping two Rb isotopes, and other experimental details.

2.1 Vacuum Chamber System

The vacuum chamber is comprised of the experiment cell, a pumping system, and a pressure gauge. The experiment cell, manufactured by Technical Glass, Inc., is a Pyrex cube with side length three inches and walls 0.25 inches thick as shown in Fig. 10. The 9 square inch windows provide optical access for all of the experimental beams. A 3 inch long tube with O.D. 1.5 inches is extended from one of the edges and connected to a 2.75 inch O.D. Conflat flange.

The pumping system utilizes an ion pump, VacIon Plus 55 StarCell® from Varian, Inc., to maintain the pressure in the entire chamber. There are two valves in the chamber. One is a right-angle, all-metal valve used to connect the vacuum chamber to the external turbo pumping station, and the other is a smaller right-angle, all-metal valve for controlling vapor diffusion from the atomic source to the chamber. An ionization gauge, UHV-24 Gauge from Varian, Inc. (detection range from 10^{-3}

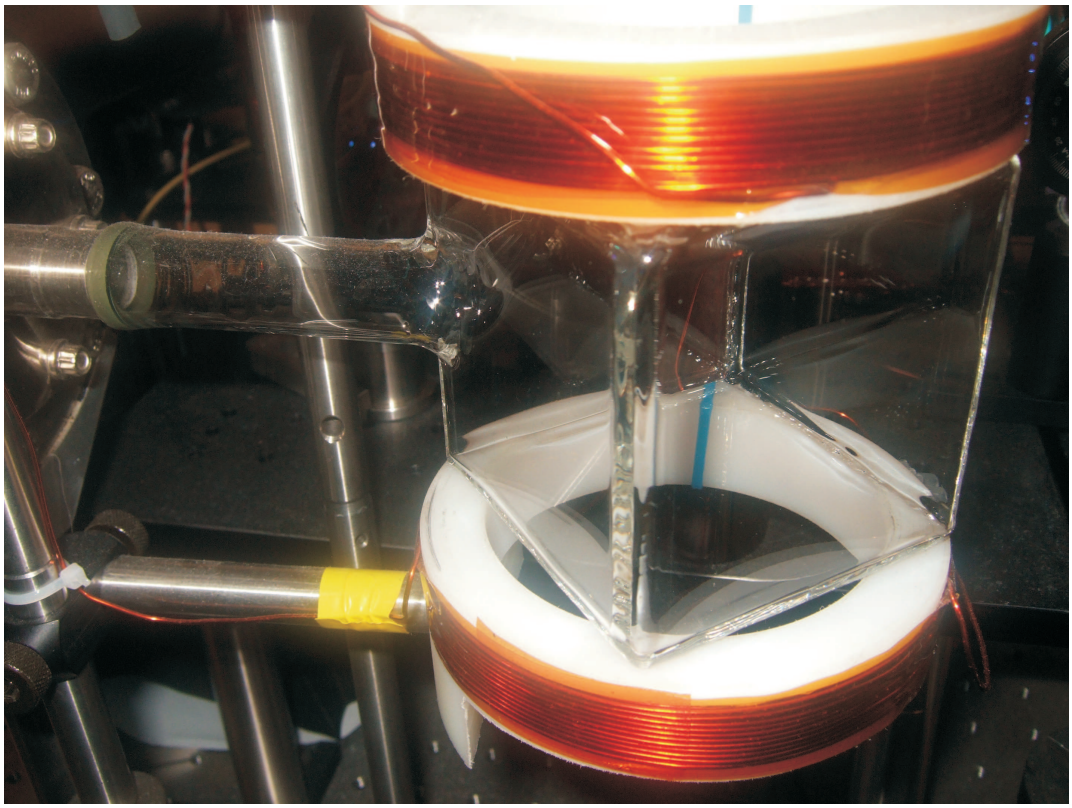

Figure 10: Glass cell made of pyrex. It is a cube of side length 3 inches. The picture also shows a pair of coils used to create magnetic field gradient for the MOT.

torr to 10^{-11} torr), is used to monitor the pressure inside chamber.

The chamber was baked out initially at 150 °C. After a week, the pressure inside the vacuum chamber stop decreasing at 10^{-7} torr and then the bakeout process was terminated. During cooling, the ionization gauge and ion pump were switched on for degassing. By the next day, the pressure dropped down to $\sim 10^{-10}$ torr. Finally, we applied 50 ft-lb torque to seal the right angle all-metal valve and the vacuum chamber was detached from the external turbo pumping station.

The atomic source is an ampoule from Alfa Aesar containing 1 g of Rubidium at natural abundance. The ampoule is stored inside the bellows connected to the chamber with the smaller right-angle valve. We broke the ampoule after the baking process by snapping it through the bellows.

2.2 Magneto-Optical Trap

Since the first experimental demonstration with sodium atoms [61], the magneto-optical trap (MOT) has been extensively used as a tool to study the spectroscopic properties of atoms. In addition to the robust design, the MOT provides low velocity of the trapped atoms, which reduces inhomogeneous broadening. The MOT operates via strong optical interactions with the atoms and typically contains a large number of atoms ($\simeq 10^6 - 10^9$) at low temperatures on the order of tens of micro-Kelvin. A standard MOT [62] consists of two gradient magnets and three sets of counter-propagating laser beams, as shown in Fig. 11. Each laser beam exerts a scattering force on the atoms. When the laser is red detuned from the atomic transition, the atoms preferentially absorb photons from a laser beam propagating opposite to their direction of motion. The energy is subsequently dissipated symmetrically in a dipole pattern through spontaneous emission. In addition to the damping force, the presence of the magnets creates a spatially dependent force. Because the magnets are operated with opposing currents, they create a quadruple field that is zero in the center of the

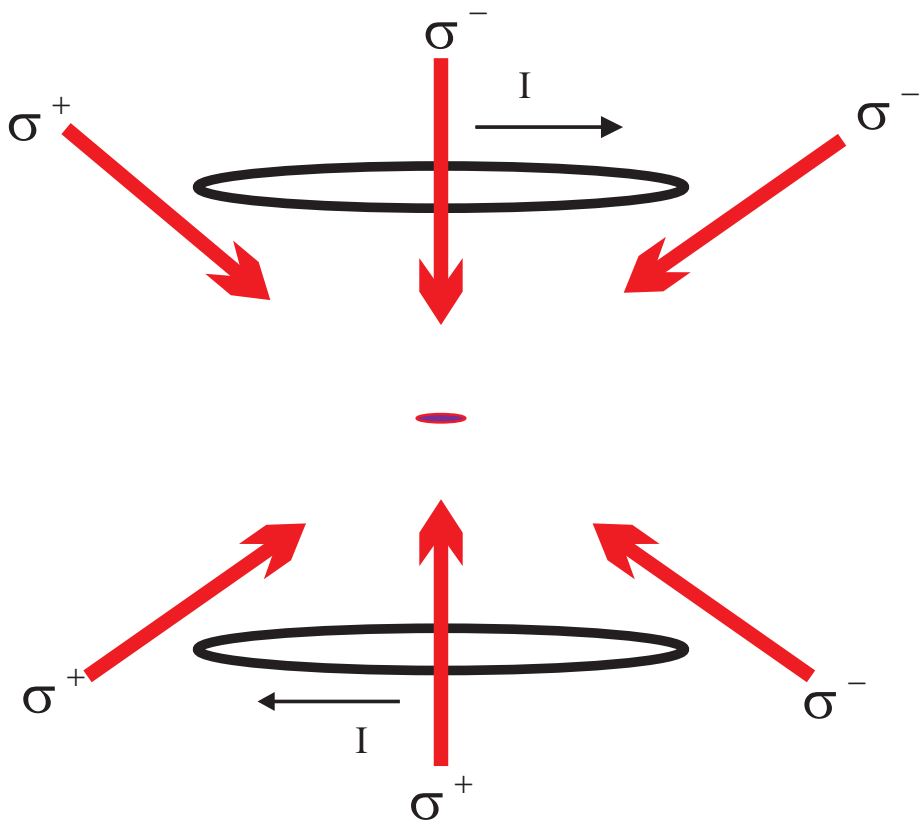

Figure 11: Representation of a magneto-optical trap setup. Three orthogonal pairs of beams with opposite circular polarizations intersect inside an ultra high vacuum (UHV) chamber to decelerate the atoms. A pair of coils with anti-Helmholtz configuration provides a magnetic quadruple field to confine the atoms.

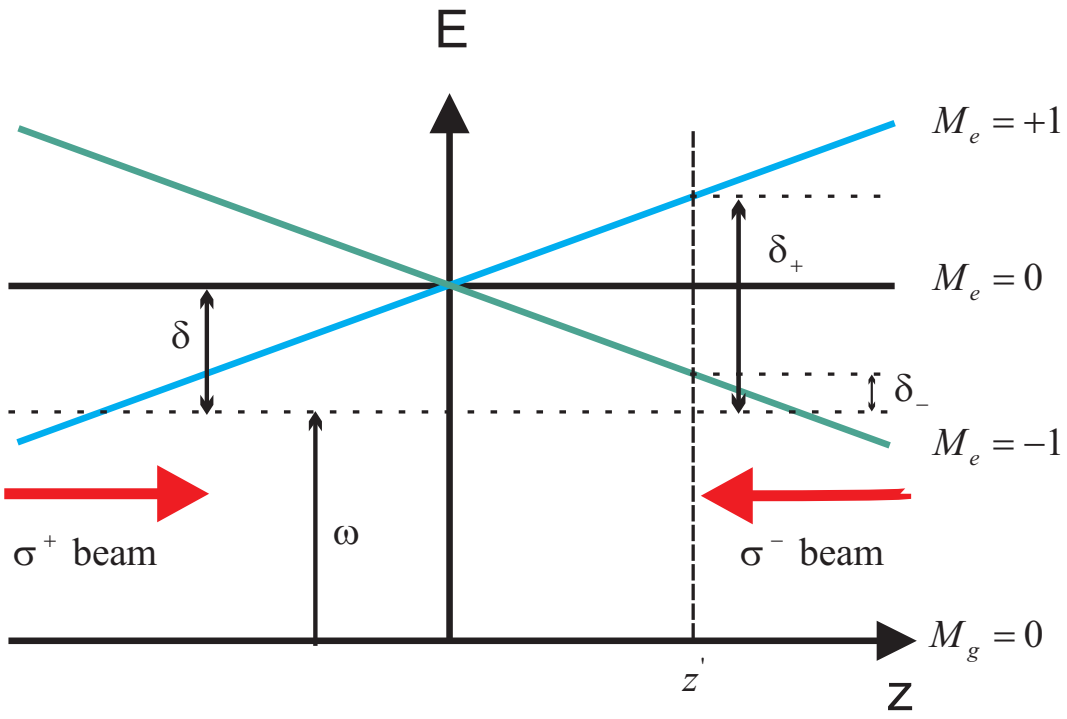

Figure 12: An atom in a 1-D configuration. The inhomogeneous magnetic field removes the excited state degeneracy and provides a spatially dependent force.

two magnets and increases approximately linearly in every direction from the center. Due to the $\sigma^{\pm}$ polarizations present in each beam, the Zeeman shifts caused by the magnets provide a spatial dependence to the scattering force. Consequently, the MOT both dampens motion and exerts a restoring force on the atoms.

The mechanism of laser cooling relies on the Doppler shift. Consider a laser of frequency ω interacting with a fixed two-level atom that has a transition frequency ω_0. The scattering force along the direction of the laser beam experienced by the atom is

$$F_s = \hbar k \frac{s_0 \gamma/2}{1 + s_0 + (2\delta/\gamma)^2}, \tag{30}$$

where $k = \frac{2\pi}{\lambda}$ is the laser wavelength, $s_0 = I/I_s$ is the on-resonance saturation parameter, γ is the linewidth of the atomic transition, and $\delta = \omega - \omega_0$. Now, if we take into account the velocity of the atom $\vec{v}$, the Doppler shift with respect to

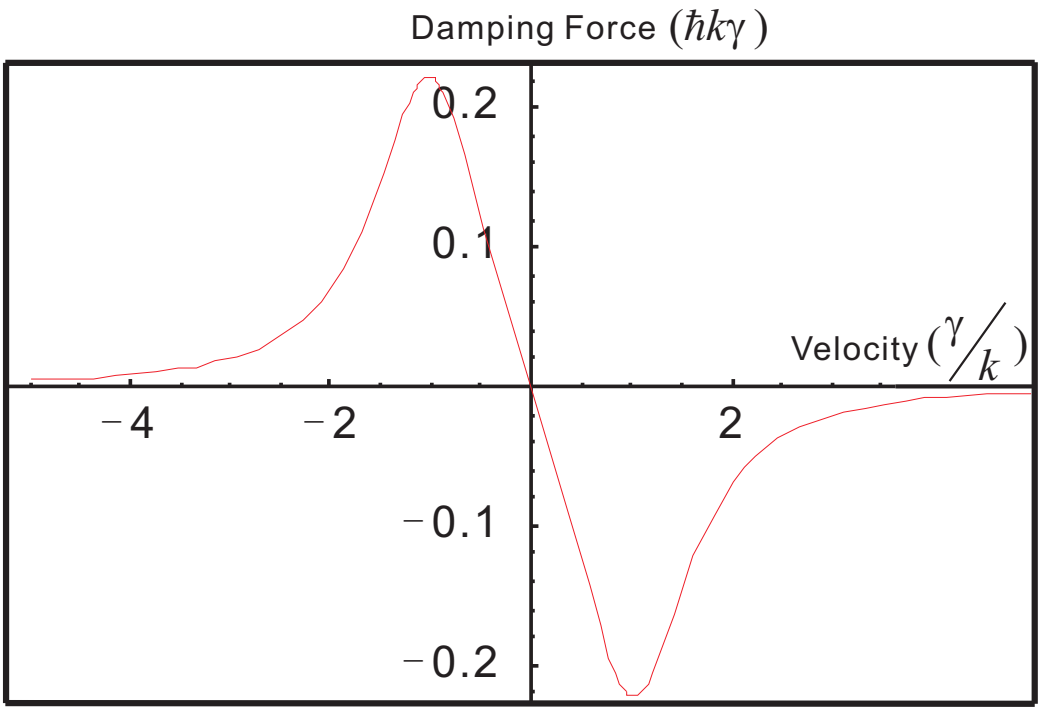

Figure 13: 1-D optical damping force $\vec{F} = \vec{F_+} + \vec{F_-}$ on an atom for $s_0 = 1$ and $\delta = -\gamma$.

the laser field will be $\delta_{Doppler}(\vec{v}) = -\vec{k} \cdot \vec{v}$. An atom moving opposite to the laser propagation will experience an increase in the scattering force. Similarly, an atom moving parallel to the laser propagation will experience a decrease in the scattering force. The combined force of the two counter-propagating beams on the atom is given by $\vec{F} = \vec{F_+} + \vec{F_-}$, where

$$\vec{F_\pm} = \pm \frac{\hbar \vec{k} \gamma}{2} \frac{s_0}{1 + s_0 + (2\delta_\pm/\gamma)^2} \tag{31}$$

and the detuning $\delta_\pm$ is

$$\delta_\pm = \delta \pm \delta_{Doppler}. \tag{32}$$

As shown in Fig. 13, the total forces near $v = 0$ can be approximated as a linear function with respect to velocity. In this linear region, the force can be modeled as damping force,

$$\vec{F} \approx \alpha \vec{v}, \tag{33}$$

where the damping coefficient is given by

$$\alpha = \frac{-8\hbar k^2 s_0 \delta}{\gamma(1 + s_0 + (2\delta_\pm/\gamma)^2)^2}. \tag{34}$$

When $\alpha > 0$, this is a viscous force.

A MOT is able to trap atoms because it produces a position-dependent optical force on an atom inside the trapping region. A magnetic quadruple field modifies the scattering rate by introducing the position-dependent Zeeman shift δ_{Zeeman} on the atomic transition. We start with a 1-D MOT: the inhomogeneous magnetic field can be described as $\vec{B}(z) = B'\vec{z}$, where $B' = \frac{dB}{dz}$ is the gradient of the magnetic field. The resulting Zeeman shift is

$$\delta_{Zeeman} = \frac{\mu m_J}{\hbar} B' z = \beta z, \tag{35}$$

where μ is the magnetic dipole moment of the atom and m_J is the quantum number of the electron total angular momentum J. A simple example, as shown in Fig. 12, is an atom with spin J = 0 in the ground state and spin J = 1 in the excited state; this atom is placed in the field of two counter-propagating σ^+ and σ^- polarized laser beams. If the atom has a position with z > 0, then it preferentially absorbs σ^- polarized light propagating in the -z direction and is coupled to the $m_J = -1$ magnetic sublevel. Consequently the atom will scatter more photons from the σ^- beam and experience a net force directed toward z = 0. A similar process occurs when z < 0. Due to the Doppler and Zeeman effects, the detuning of these lasers beams becomes

$$\delta_\pm = \delta \pm \delta_{Doppler} \pm \delta_{Zeeman}. \tag{36}$$

Assuming the Doppler and Zeeman shift relative to the detuning is small, the total force on the atom can be expressed as

$$\vec{F} = \alpha\vec{v} - \frac{\alpha\beta}{k}\vec{z}. \tag{37}$$

The atomic species used in these experiments generally have an energy structure that is more complicated than the two-level example above. For example, the hyperfine splitting of the ground state of Rb provides two decay channels from the excited

state. Thus, all of the atoms will eventually decay to the state that is not in resonance with the trapping lasers, and the trapping process will cease. Another laser known as the repumping laser is needed to prevent the atoms from accumulating in the other hyperfine ground state (dark state) which does not participate in the cooling cycle. In general, the cooling laser is set on the cyclic transition $|5S_{1/2}, F = 3\rangle \rightarrow |5P_{3/2}, F = 4\rangle$ for ^{85}Rb and $|5S_{1/2}, F = 2\rangle \rightarrow |5P_{3/2}, F = 3\rangle$ for ^{87}Rb in the D_2 line. The repumping laser depopulates the dark state, $|5S_{1/2}, F = 2\rangle$ for ^{85}Rb and $|5S_{1/2}, F = 1\rangle$ for ^{87}Rb.

2.3 Laser System

There are four main laser frequencies used. Two operate on the Rb D_2 transitions for cooling and repumping atoms. The other two are on the D_1 transition for the experiment. A practical convenience of working with Rb among all alkaline atoms is that the laser diode operating on the Rb transition is very inexpensive because it is widely used as a CD laser reader. For example, a laser diode of about 120 mW optical power from SHARP costs only about $25.

Our diode laser system is a tunable external cavity diode laser (ECDL) in Littrow configuration. An external diffraction grating is used to select the output wavelength. The fine tuning of the grating is controlled by a piezo-electric transducer (PZT). The first order diffracted beam is reflected back into the diode as an optical feedback to build up the field inside this external cavity. The zeroth order beam is directed outward to be used in the experiment. We employ holographic gratings which produce less stray light than ruled gratings. They are from Edmund Optics (part number 43221) with 1800 grooves per mm.

The nominal lasing wavelength at room temperature differs from diode to diode. Usually for SHARP GH0781JA2C, the nominal wavelength is around 784 nm. We can easily tune the laser wavelength down to 780 nm, the laser cooling transition, by properly adjusting the grating angle. It is more laborious to tune the laser up to 795

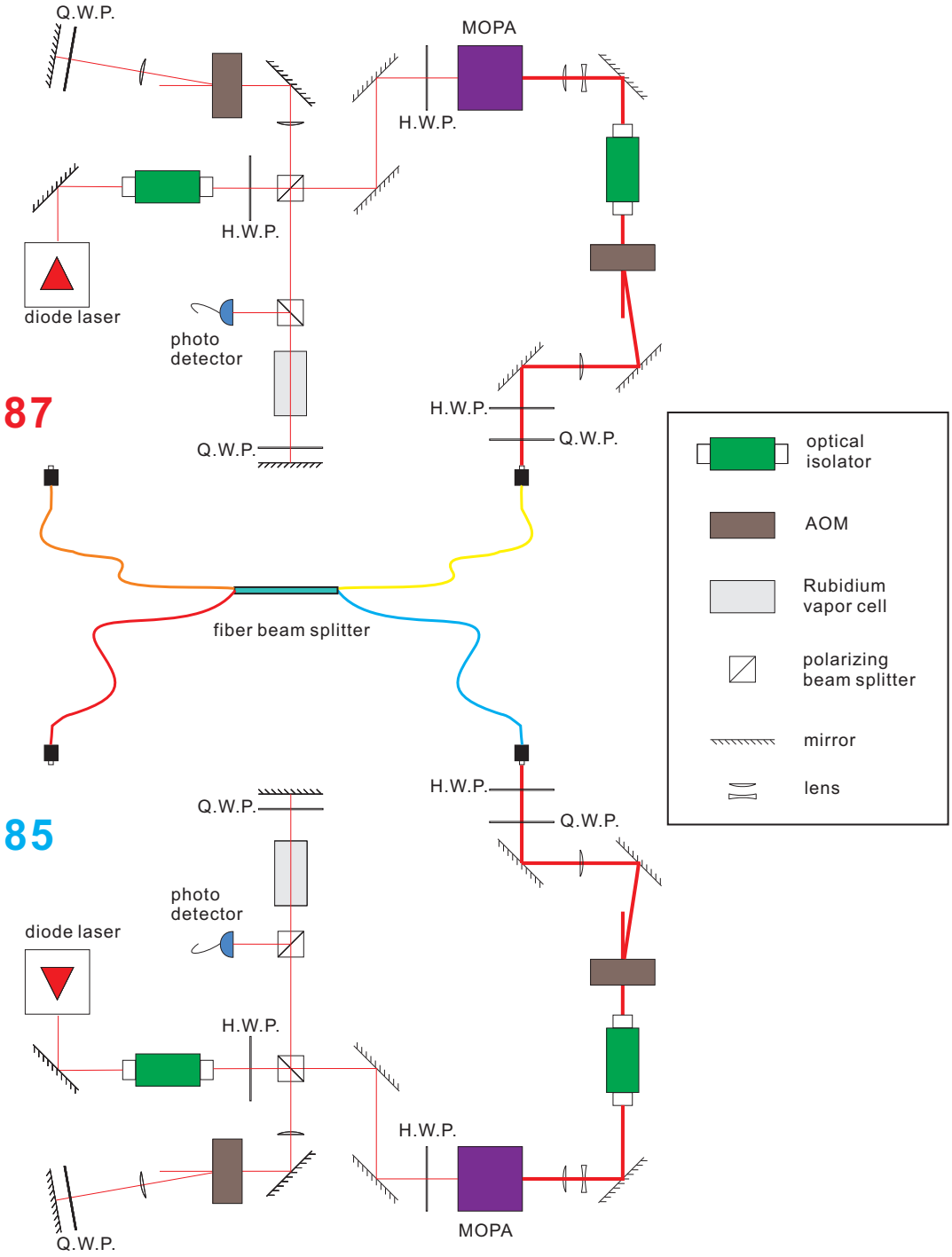

Figure 14: Schematics of MOT trapping beam setup. Two separate trapping beam systems are combined on the fiber beam splitter for ^{85}Rb and ^{87}Rb. H.W.P. is a half wave plate. Q.W.P. is a quarter wave plate.

nm. To accomplish this, the laser diode needs to be heated to about 50°C, which unfortunately reduces the laser power output and shortens the diode life time.

Larger laser powers are achieved by employing the master oscillator power amplifier (MOPA). The MOPA configuration consists of a seed laser and an optical amplifier. We use an LD 1666 tapered amplifier (TA) diode from Power Technology. The TA is mounted on an aluminum block and controlled by a Newport laser diode controller and temperature controller module. Initially, the temperature is stabilized around 25°C and then tuned to optimize the power output. The laser diode operating current is set at 1.5 A, which is below the maximum allowed current, in order to extend the lifetime of the amplifier chip. The first tapered amplifier in this setup lasted for approximately 7000 hours of operation.

The laser frequency is roughly stabilized by current control and the temperature stabilization provided by a home-built controller box. The fine tuning and locking are accomplished by using an FM spectroscopy setup. The laser current is modulated by an external rf source. The trapping frequency is locked on the crossover of $|5S_{1/2}, F = 3\rangle \rightarrow |5P_{3/2}, F = 4\rangle$ and $|5S_{1/2}, F = 3\rangle \rightarrow |5P_{3/2}, F = 2\rangle$ for the ^{85}Rb MOT. Fig. 15 shows the relevant energy transitions for locking. A double-pass configuration of acousto-optical modulators (AOM) at a frequency of 84 MHz, -1 order, is placed on the locking setup to control the detuning of the trapping frequency. Another AOM, with frequency fixed at 80 MHz, -1 order, is used as an optical switch for the experiment. In the case of ^{87}Rb, the trapping frequency is locked on the crossover of $|5S_{1/2}, F = 2\rangle \rightarrow |5P_{3/2}, F = 3\rangle$ and $|5S_{1/2}, F = 2\rangle \rightarrow |5P_{3/2}, F = 2\rangle$. The frequency of the double-pass AOM is about 93 MHz, -1 order, and the frequency of the switching AOM is fixed at 80 MHz, -1 order. As shown in Fig. 14, one of the output ports of a fiber beam splitter is used for the trapping beams in the horizontal plane. The other port provides the trapping beams along the direction of the trapping coils. The optical power of a beam in the horizontal direction is half the optical power of a beam

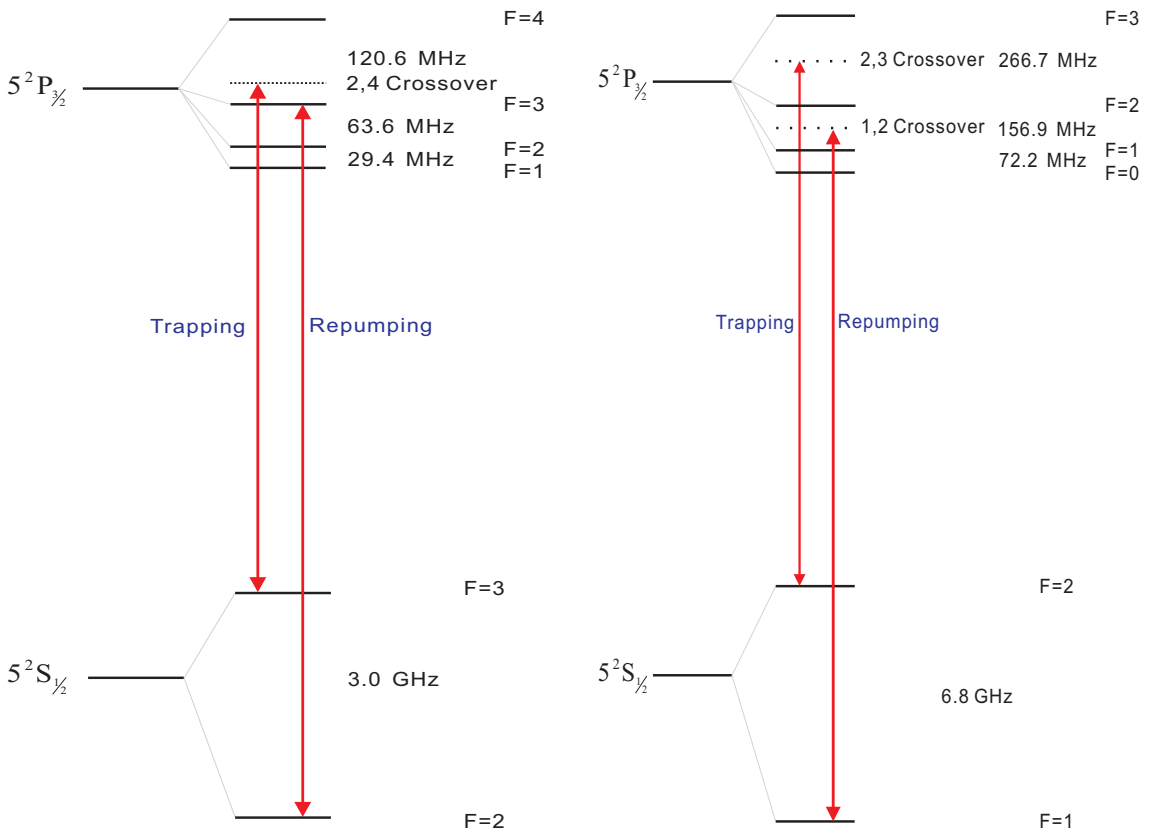

(a) For ^{85}Rb, the trapping frequency is locked on the crossover of $F = 3 \rightarrow F^{'} = 4$ and $F = 3 \rightarrow F^{'} = 2$, and the repumping frequency is locked on $F = 2 \rightarrow F^{'} = 3$.

(b) For ^{87}Rb, the trapping frequency is locked on the crossover of $F = 2 \rightarrow F^{'} = 3$ and $F = 2 \rightarrow F^{'} = 2$, and the repumping frequency is locked on the crossover of $F = 1 \rightarrow F^{'} = 2$ and $F = 1 \rightarrow F^{'} = 1$.

Figure 15: Transition of locking for ^{85}Rb and ^{87}Rb MOT.

in the direction of the trapping coils. The beam in the horizontal plane is split into four separate beams using two polarization beam splitters. The trapping beam for the vertical direction is split into two independent beams by using a polarization beam splitter. The six trapping beams are expanded to 2-inch diameters and collimated, with the intensity of about 2 to 3 saturation intensities. The repumping laser has the same layout as the trapping laser with the exception of the MOPA as shown in Fig. 16. It is locked on the $|5S_{1/2}, F = 2\rangle \rightarrow |5P_{3/2}, F = 3\rangle$ transition for ^{85}Rb and on the crossover of $|5S_{1/2}, F = 1\rangle \rightarrow |5P_{3/2}, F = 2\rangle$ and $|5S_{1/2}, F = 1\rangle \rightarrow |5P_{3/2}, F = 1\rangle$ for ^{87}Rb. The frequencies of the switching AOMs are 200 MHz, +1 order, and 80

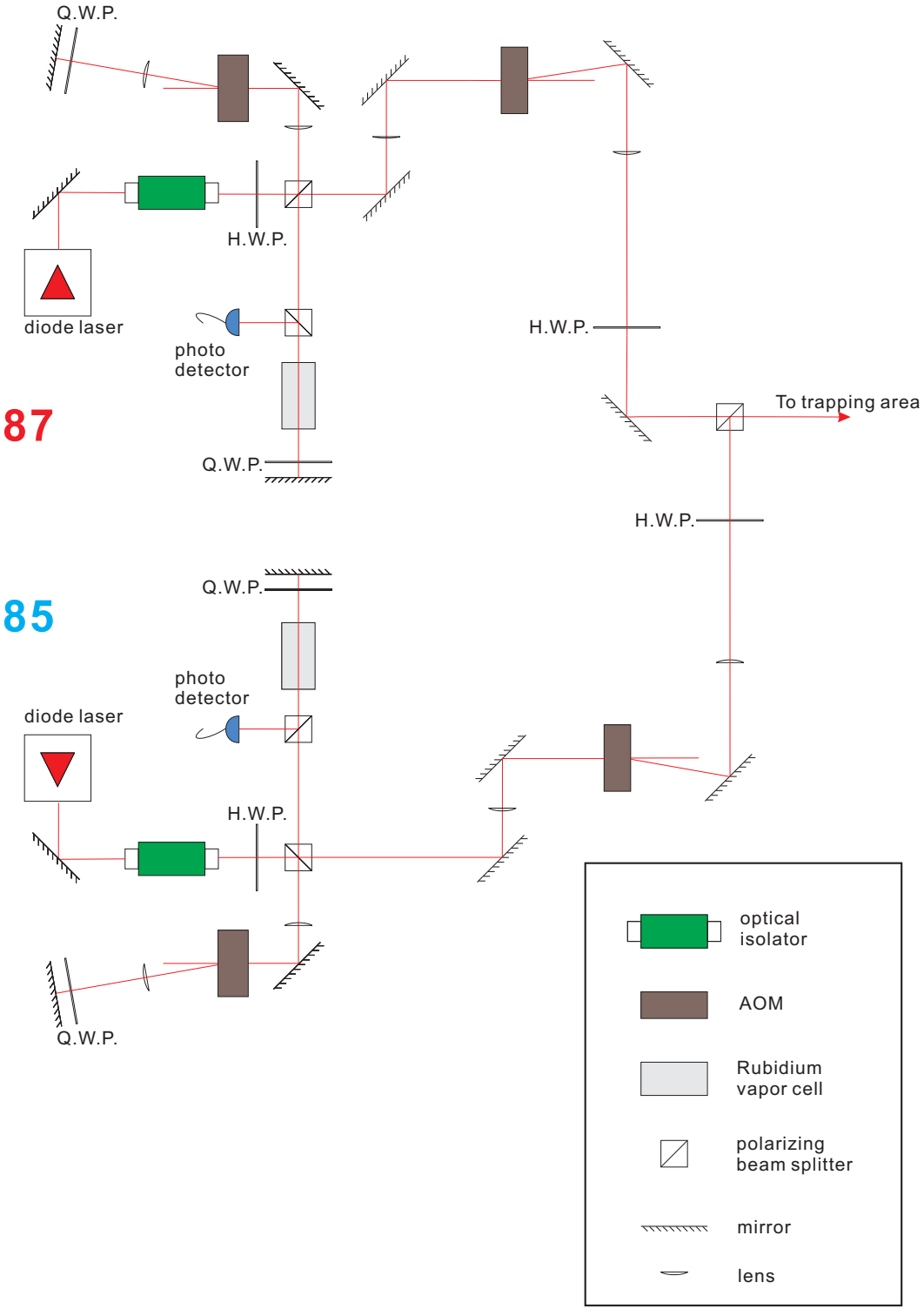

Figure 16: Schematics of MOT repumping beam setup. Two separated trapping beam systems are combined on the polarizing beam splitter for ^{85}Rb and ^{87}Rb. H.W.P. is a half wave plate. Q.W.P. is a quarter wave plate.

MHz, +1 order, for ^{85}Rb and ^{87}Rb, respectively. The AOM used for tuning the laser frequency is about 80 MHz, +1 order, for ^{87}Rb and 64 MHz, +1 order, for ^{87}Rb. The repumping laser beam is directed into the trapping area from a side; the beam size is the same as for the trapping beams.

The MOT coils are placed in the anti-Helmholtz configuration to generate the magnetic quadruple field. 10 layers of copper wire, with 10 turns per layer, are wrapped around a circular nylon frame. The separation between the coils is 3 inches. These coils can produce a magnetic field gradient of 6.6 Gauss/cm while operating at a current of 4 A.

2.4 Tunable Optical Filter

We use Fabry-Perot etalons to filter out Rayleigh-scattered light as well as the scattering by optical surfaces. Fabry-Perot etalons are narrow-band optical filters made-up of two partially reflecting mirrors in parallel orientation. The standing waves created between the mirrors generate constructive interference when they exactly fit the cavity length. The transmission spectrum of an etalon is characterized by two parameters; one is the free spectral range (FSR), the other is the finesse (F). FSR is related to the thickness of the etalon d and the refractive index of the material n in the following way:

$$FSR = \frac{c}{2nd}, \tag{38}$$

where c is the speed of light. Finesse is determined by the reflectivity of the two end surfaces R_1 and R_2 and can be related to the FSR:

$$F = \frac{\pi(R_1R_2)^{\frac{1}{4}}}{1-\sqrt{R_1R_2}} = \frac{FSR}{\Delta\nu_{FWHM}}, \tag{39}$$

where $\Delta\nu_{FWHM}$ is the full width at half maximum of the transmission spectrum [63]. The transmission can be expressed as

$$T = \frac{1}{1+(\frac{2F}{\pi})^2\sin^2(\frac{2\pi nd\nu}{c})}, \tag{40}$$

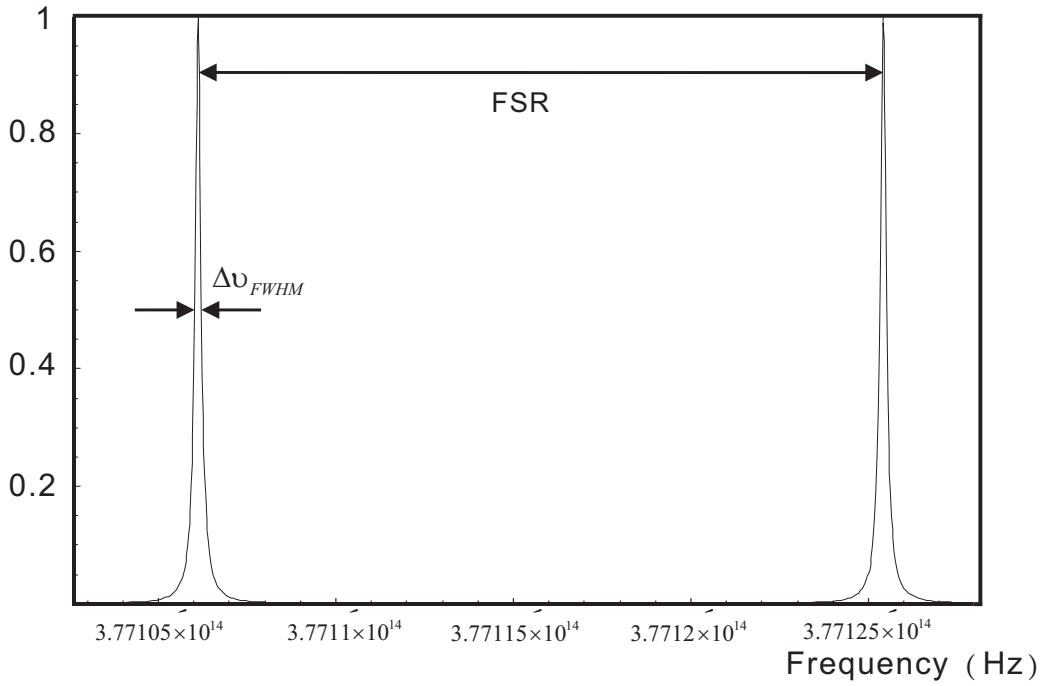

Figure 17: The transmission of a Fabry-Perot etalon with free spectral range 20 GHz.

where ν is optical frequency. In the ideal case, the maximum transmission (T_{Max}) is equal to unity as shown in Fig. 17. However, in real cavities with internal losses, surface roughness, and imperfect parallelism of the two surfaces, the maximum transmission is reduced.

The etalons are made of fused silica with 1 inch diameter and 5 mm thickness. The FSR corresponding to 5 mm thickness is 20 GHz. The finesse is about 50 to 100 corresponding to a $\Delta\nu_{FWHM}$ of 400 to 200 MHz. We mount the etalon inside a 2 inch long tube and seal it with two AR coated windows on both sides to reduce temperature fluctuations. The tube is mounted on an aluminum stage for temperature stabilization. The temperature variations cause the thermal expansion of fused silica and change its refractive index. Both effects result in a shift of the resonance peak. We use a 10 kΩ thermistor and a Newport temperature controller to stabilize the etalon temperature. The transmission of the etalon is adjusted by changing its temperature. The frequency separation of the $|5S_{1/2}, F = 2\rangle \rightarrow |5P_{1/2}, F = 3\rangle$ transition and the

$|5S_{1/2}, F = 3\rangle \rightarrow |5P_{1/2}, F = 3\rangle$ transition is about 3.036 GHz. When the etalon is on the resonance of one of the transitions, the transmission at the frequency of the other transition is on the order of 10^{-3}.

2.5 Photon Detection System

We employ silicon avalanche photodiodes from PerkinElmer. The photodiode detects in the wavelength range of 400 to 1060 nm. For our experiments, its most important characteristics are the quantum efficiency and the dark count rate. The SPCM-AQ4C has four independent channels, a quantum efficiency of about 55% at 795 nm, and a dark count rate of about 300 counts per second. After a photon is detected, the detector sends out a 25 ns TTL pulse. The electronic pulses are sent to a gating circuit. The latter is activated by an external TTL switch. The pulses after the gating circuit are guided to a photon counter (SR400 from Stanford Research Systems) and then recorded on multiple-event time digitizer (P7888 from FAST ComTec), as shown in Fig. 18.

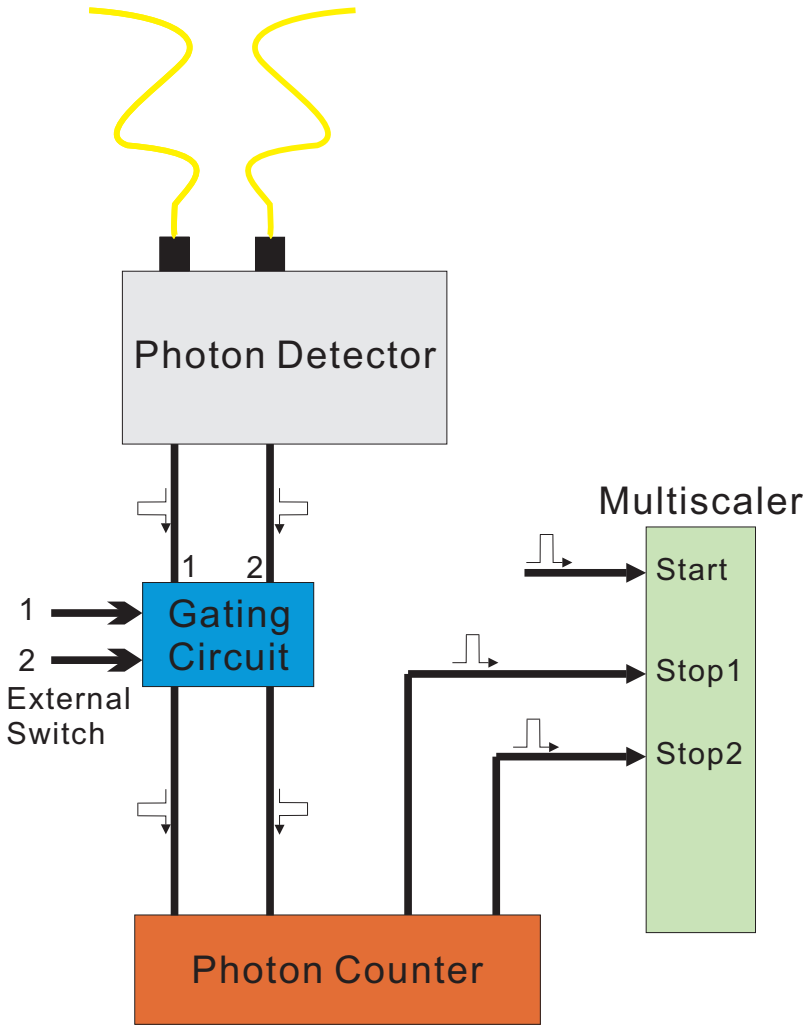

Figure 18: Diagram of a photon detection system. The multiscaler is triggered by a pulse generated on every experimental loop. The stop1 and stop2 record the detection of the signal and idler photons respectively. The external switches are TTL pulses created by a programmable TTL pulse generator.

CHAPTER III

DUAL SPECIES MATTER QUBIT ENTANGLED WITH LIGHT

Part of this chapter is based on Ref. [64].

In this chapter, I describe an interferometrically robust quantum repeater element based on entangled mixed species atomic, and frequency-encoded photonic, qubits. This scheme avoids the use of two interferometrically separate paths for qubit entanglement distribution. The qubit basis states are encoded as single spin wave excitations in each of the two atomic species co-trapped in the same special region. The spectroscopically resolved transitions enable individual addressing of the atomic species. One may therefore perform independent manipulations in the two repeater arms that share a single mode transmission channel. Phase stability is achieved by eliminating the relative ground state energy shifts of the co-trapped atomic species, as is in any case essential to successfully read out an atomic excitation [32, 33].

3.1 Two Species MOT

Two species magneto-optical traps have been realized for the study of the ultracold atoms. In boson-boson mixtures, collisional trap loss and loading dynamics have been studied with ^{85}Rb-^{23}Na [65], ^{85}Rb-^{133}Cs [66], ^{87}Rb-^{133}Cs [66], ^{7}Li-^{23}Na [67], and ^{52}Cr-^{87}Rb [68]. Bosons have also been used to sympathetically cool fermions [69, 70]. The interactions between bosons and fermions are controlled to form molecules by employing magnetic-field (Feshbach) scattering resonances [71]. Here, we use a two-isotope magneto-optical trap to produce qubit states for matter-light entanglement.

The first step for the dual species experiment is to trap two different species of

atoms within the same volume. Two sets of MOPA systems and repumping lasers are employed to trap ^{85}Rb and ^{87}Rb atoms simultaneously. The trapping beams for ^{85}Rb and ^{87}Rb are coupled into a 50-50 fiber beam splitter, as shown in Fig. 14. The polarizations of the trapping beams after the fiber beam splitter are maintained by two sets of half and quarter wave plates before the fiber beam splitter to ensure that the polarization is the same for both frequencies. This is done by optimizing the reflection or transmission of the resulting beams after the polarizing beam splitter. The repumping lasers are mixed on a polarization cube then directed to the trapping area as shown in Fig. 16.

The transitions for the experiment and locking signals are described in Chapter II. The switching of ^{85}Rb and ^{87}Rb trapping and repumping beams is driven by the same TTL pulses. One advantage of using ^{85}Rb and ^{87}Rb is that they both have substantial natural abundance : 72% and 28%, respectively. As the vapor pressures are the same, we are able to trap a comparable number of atoms of each species. Since the readout efficiency of the idler photons depends on the optical thickness of the MOT, we can obtain similar coincidence count rates for both isotopes.

3.2 Write/Read Laser Setup

The generation of qubit states requires simultaneous co-propagating laser excitation pulses for ^{85}Rb and ^{87}Rb. We generate both frequencies from a single laser by locking to the frequency halfway between transitions of the two species. First, consider the write laser. The setup is shown in Fig. 19: a double-pass AOM (shifting AOM) set at 195 MHz is used to adjust the frequency of the write beam, and a single-pass AOM (switching AOM) set at 205 MHz is used for optical switching. In this configuration, if the write field is locked on the ^{85}Rb $|5S_{1/2}, F = 3\rangle \rightarrow |5P_{1/2}, F = 2\rangle$ transition, its first sidebands will be located on the write transition of ^{85}Rb and ^{87}Rb with the correct modulation frequency. The read field is produced in a similar manner. Applying

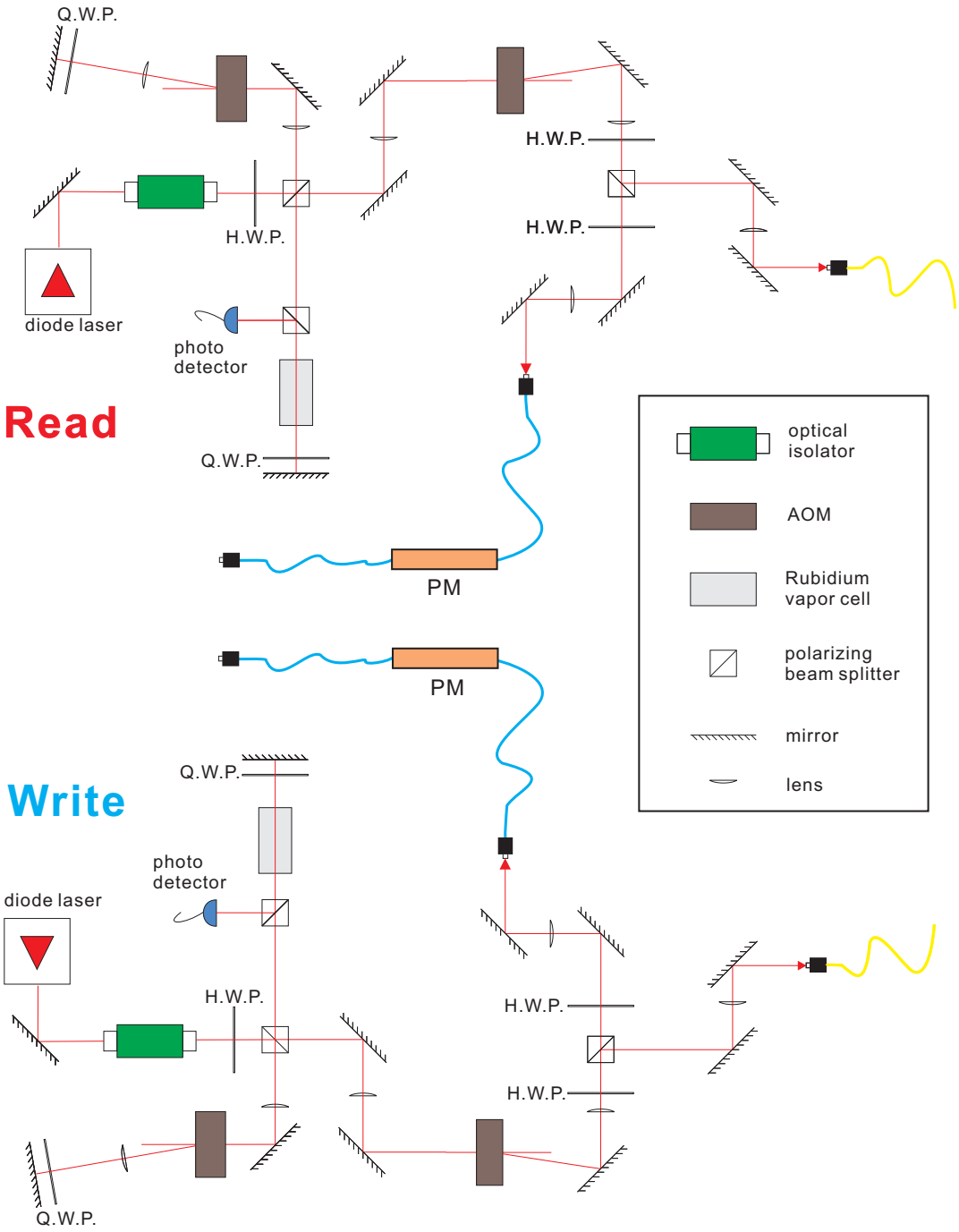

Figure 19: Schematics of write and read beam setup. A single write and read laser are coupled into a PM to generate the sidebands for ^{85}Rb and ^{87}Rb isotopes. H.W.P. is a half wave plate. Q.W.P. is a quarter wave plate.

175 MHz to the shifting AOM and 200 MHz to the switching AOM gives the first sidebands of the read phase modulator (PM) on resonance of the read transitions for both isotopes if the read beam is locked on the ^{87}Rb $|5S_{1/2}, F = 1\rangle \rightarrow |5SP_{1/2}, F = 1\rangle$ transition. We can adjust the detuning of the ^{85}Rb and ^{87}Rb write beams by changing the rf frequency applied to the shifting AOM.

3.3 Alignment

The alignment of the experimental beams is based on the four-wave mixing process. Three beams interact with a nonlinear media characterized by the third-order nonlinear susceptibility $\chi^{(3)}$ and result in the generation of a phase conjugate field from the media. This was first demonstrated in a solid state system [72] and latter developed in cold atomic ensembles with electromagnetically induced transparency [29, 73].

We use ^{85}Rb for this procedure. After the MOT is loaded, all the atoms are in the $|5S_{1/2}, F = 3\rangle$ ^{85}Rb hyperfine ground state. We use the write beam on this transition to maximize the absorption inside the MOT by adjusting the beam's position. The alignment of the four fields (write, read, signal, and idler) must satisfy the phase matching condition given by Eq. (50). Because the frequencies of these four transitions are close to each other, we can approximate this condition by

$$\mathbf{k}_w^{(\nu)} + \mathbf{k}_r^{(\nu)} = 0 \quad \text{and} \quad \mathbf{k}_s^{(\nu)} + \mathbf{k}_i^{(\nu)} = 0, \tag{41}$$

where ν denotes ^{85}Rb or ^{87}Rb. The write beam can be coupled directly into the read fiber with about 75% efficiency. Light at the frequency of the signal transition is coupled into the signal fiber. The read and the signal beams are separated by about 3°.

Using horizontal, vertical, and vertical polarizations for the write, read, and signal fields respectively, we detect a horizontally polarized auxiliary field with a CCD camera. The intensity of the auxiliary field depends on the amplitude the write, read, and signal fields. The geometrical phase mismatch $\Delta k = (-\mathbf{k}_w^{(\nu)} - \mathbf{k}_r^{(\nu)} + \mathbf{k}_s^{(\nu)} + \mathbf{k}_i^{(\nu)}) \cdot \mathbf{z}$

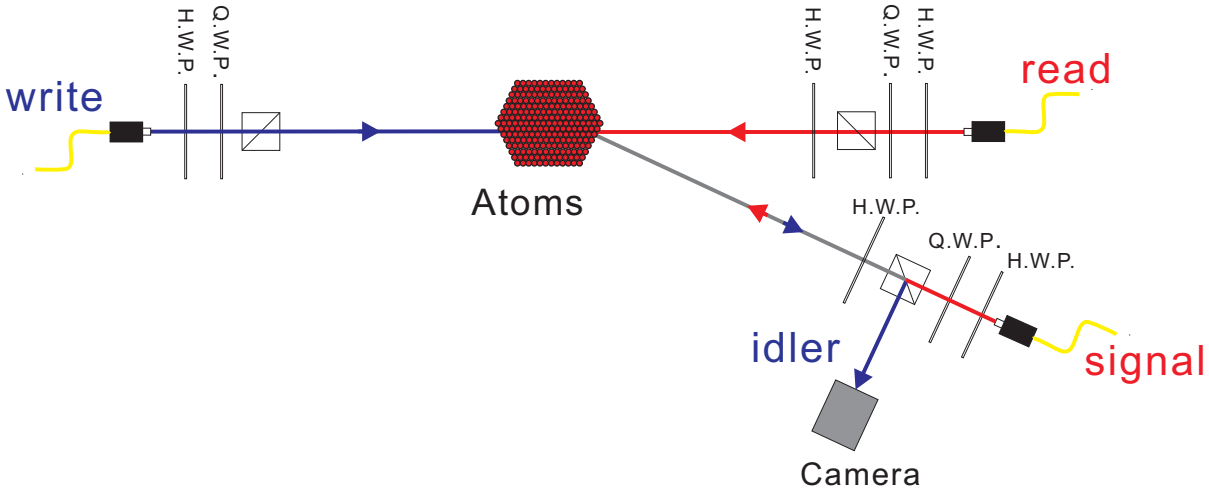

Figure 20: Four-wave mixing alignment geometry. Because the wavelength of these four fields are close, we can approximate them as a degenerate four-wave mixing case where the geometry will be a cross.

along the propagation direction of the generated auxiliary field will reduce its generation efficiency. The experimental setup is shown in Fig. 20 . The power of the auxiliary field is optimized by adjusting the signal beams position. The powers of the first three fields are initially limited to less than 100 μW in order to prevent the fields from pushing the atoms away from the position where they will be during the experiment. Once we observe the auxiliary field, we lower the powers of the other three fields, then optimize the auxiliary field by changing the position of the signal field. We repeat this process until we can barely see the auxiliary field spot on the CCD camera. The signal field then is coupled into the idler fiber with about 75% efficiency.

3.4 Phase Coherent Bichromatic Field

We produce phase coherent bichromatic fields using electro-optic modulators. The operation of the electro-optic modulator relies on the Pockels effect. The applied electric field induces birefringence in an optical medium which lacks inversion symmetry. The polarization of the optical beam is aligned along the z-axis of the electric-optic

crystal, so that the optical phase can be modulated by varying the electric field. With the applied modulation field $V(t) = V_0 \sin \Omega t$, the phase ϕ of the optical field

$$E(t) = E_0 \cos[\omega t + \phi(t)] \tag{42}$$

can be represented as

$$\phi(t) = \frac{n^3 r V_0 \sin \Omega t}{2d}, \tag{43}$$

where n is the refraction index of the crystal, r is the appropriate element of the electro-optic tensor, and d is the electrode separation [74]. The phase-modulated field amplitude can be rewritten as a set of Bessel functions

$$\begin{aligned} E(t) &= E_0 \cos(\omega t + m \sin \omega t) \\ &= E_0[\cos \omega t \cos(m \sin \omega t) - \sin \omega t \sin(m \sin \omega t)] \\ &= E_0[J_0(m) \cos(\omega t) + \Sigma_{k=1}^{\infty} J_k(m) \cos(\omega + k\Omega)t \\ &+ \Sigma_{k=1}^{\infty} (-1)^k J_k(m) \cos(\omega - k\Omega)t], \end{aligned} \tag{44}$$

where k is an integer, J_k is the ordinary Bessel function of order k, and m is the modulation depth, defined as

$$m \equiv \frac{n^3 r V_0}{2d}. \tag{45}$$

The output of the modulator not only will have the carrier frequency ω but also will have multiple orders of $\pm\Omega$. The amplitude distribution of this spectrum obeys the Bessel function as shown in Fig. 21. The fraction of power transferred to each of the first-order sidebands is $[J_1(m)]^2$, where J_1 is the first order Bessel function.

For the write and read beams, we use fiber-based PMs (JENOPTIK) that require less rf power to induce the phase shift compared to free space modulators. It takes about 800 mW of rf power to maximize the transfer of the optical power to the first sidebands. However, for the signal and idler channels, we use free space electro-optic modulators to avoid the optical loss due to fiber coupling. The maximum optical power that can be transferred to each of the first-order sidebands is about 34%. The

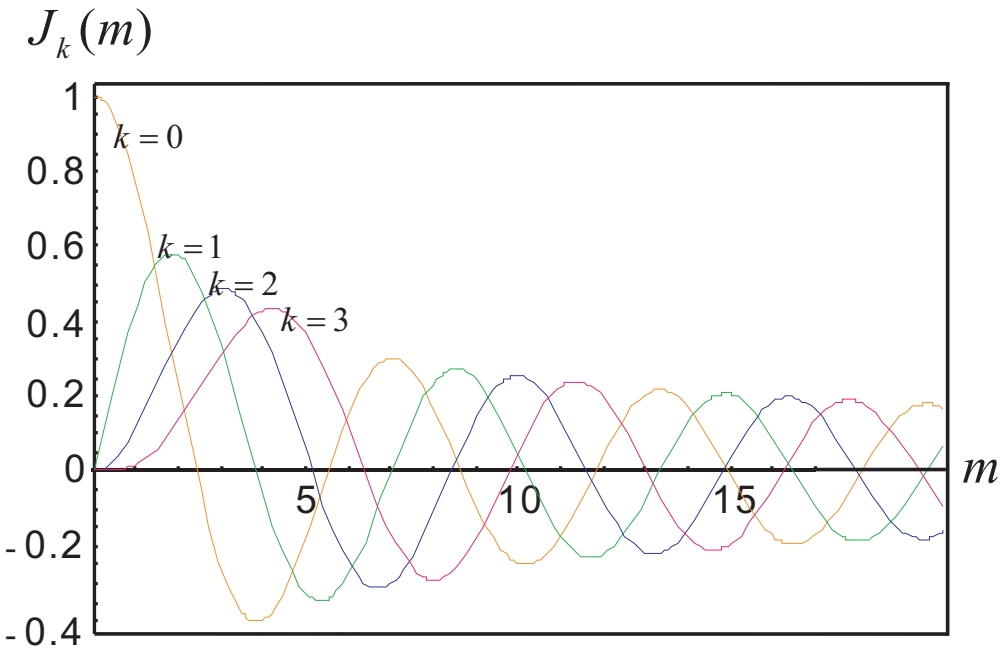

Figure 21: Bessel function of order k ($k \in$ 0,1,2, and 3) as a function of modulation depth m.

fiber-based PM will typically lose another 70 to 80 % of optical power through the fiber coupling .

3.5 Experiment

We begin by preparing a co-trapped isotope mixture of ^{85}Rb and ^{87}Rb in a magneto optical trap, as shown in Fig. 22 and described in the previous section. The experimental timing sequence is illustrated in Fig. 23. We load the magneto optical trap for about 14 ms. For the duration of the protocol, all trapping and cooling fields are switched off for 2 ms, and the atoms are essentially at rest on the time scale of the measurement process. This step is repeated at 16 Hz. The MOT coils are switched off 300 μs prior to the trapping beam being switched off. The repumping beam is switched off 200 μs after the trapping beam in order to prepare the atoms in the upper hyperfine ground state. The unpolarized atoms of isotope ν are in the ground

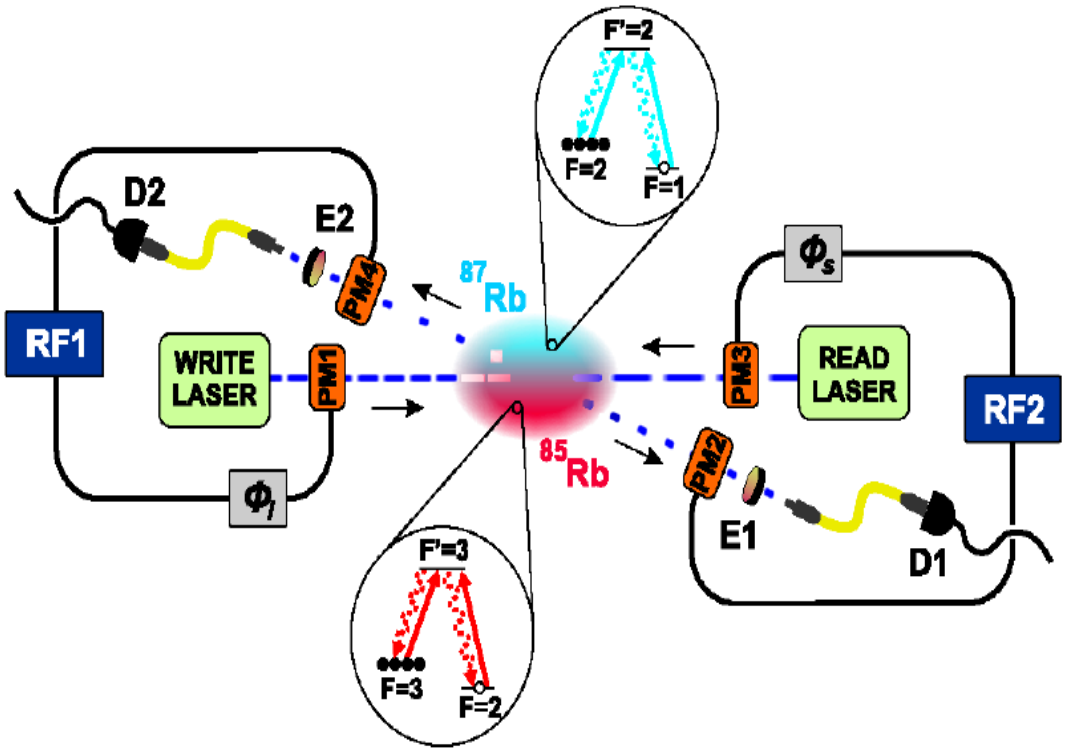

Figure 22: Schematic of the experimental setup showing the geometry of the addressing and scattered fields from the co-trapped isotope mixture of ^{85}Rb-^{87}Rb. The write and read laser fields generate signal and idler fields, respectively, detected at D1 and D2; E1 and E2 are optical frequency filters. PM1-4 are light phase modulators; ϕ_s and ϕ_i are relative phases of the driving rf fields. The insets show the relevant atomic levels.

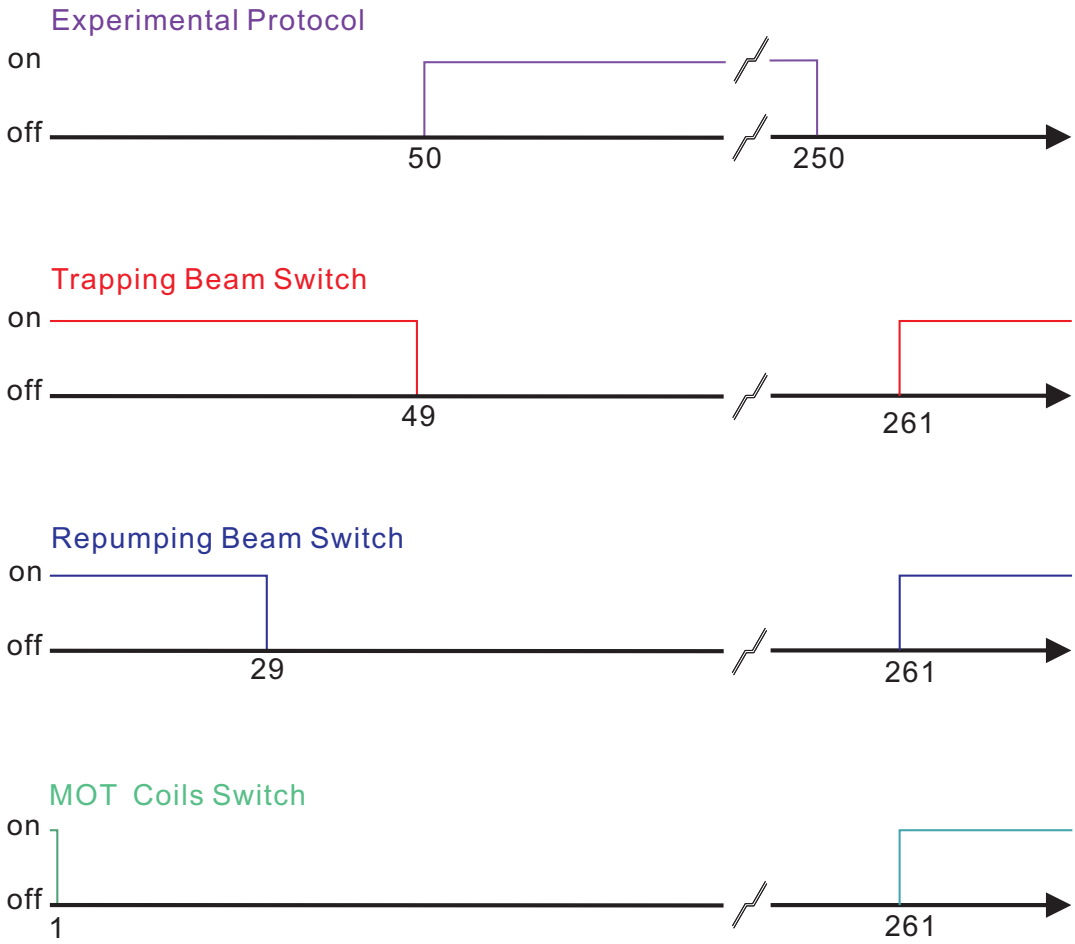

Figure 23: Illustration of experimental timing sequence. The unit of the axis is 10 μs.

hyperfine level $\left|a^{(\nu)}\right\rangle$, where

$$\left|a^{(85)}\right\rangle \equiv \left|5S_{1/2}, F_a^{(85)}=3\right\rangle, \left|a^{(87)}\right\rangle \equiv \left|5S_{1/2}, F_a^{(87)}=2\right\rangle, \tag{46}$$

and $F_f^{(\nu)}$ is the total atomic angular momentum for level $\left|f^{(\nu)}\right\rangle$. We consider the Raman configuration with ground levels $\left|a^{(\nu)}\right\rangle$ and $\left|b^{(\nu)}\right\rangle$ and excited level $\left|c^{(\nu)}\right\rangle$ with energies $\hbar\omega_a^{(\nu)}$, $\hbar\omega_b^{(\nu)}$, and $\hbar\omega_c^{(\nu)}$ respectively. Level $\left|b^{(\nu)}\right\rangle$ corresponds to the ground hyperfine level with smaller angular momentum, while level $\left|c^{(\nu)}\right\rangle$ is the $\left|5P_{1/2}\right\rangle$ hyperfine level with $F_c^{(\nu)} = F_a^{(\nu)}$.

The respective write fields for ^{85}Rb and ^{87}Rb are generated using phase modulation of a single-frequency laser pulse of wave vector $\mathbf{k}_w = k_w\hat{y}$; horizontal polarization is

Table 1: Timing sequence of experimental protocol. The protocol is repeated with a frequency of 1 MHz.

	Starting time (ns)	Ending time (ns)
Write Beam Switch	100	250
Signal Field Gate Switch	660	880
Read Beam Switch	400	800
Idler Field Gate Switch	980	170

$\mathbf{e}_H = \hat{z}$. The pulse length of the write field is 150 ns, achieved by chopping the write switching AOM. As illustrated in Fig. 22, phase modulation is accomplished by an electro-optical phase modulator PM1, which produces sidebands with frequencies

$$ck_w^{(85)} = ck_w + \delta\omega_w \quad \text{and} \quad ck_w^{(87)} = ck_w - \delta\omega_w \ (\delta\omega_w = 531.5\text{MHz}), \tag{47}$$

nearly resonant on the respective isotopic D_1 ($\left|a^{(\nu)}\right\rangle \leftrightarrow \left|c^{(\nu)}\right\rangle$) transitions (Figs. 24 and 25). The corresponding detunings $\Delta_\nu = ck_w^{(\nu)} - (\omega_c^{(\nu)} - \omega_a^{(\nu)}) \approx -10$ MHz and the generated signal fields have frequencies

$$ck_s^{(\nu)} = ck_w^{(\nu)} + (\omega_b^{(\nu)} - \omega_a^{(\nu)}). \tag{48}$$

The write field mode is focused inside the MOT with waist 450 μm.

Signal fields at two distinct frequencies are produced by spontaneous Raman scattering of the near-resonant write laser fields from each of the isotopes. We detect the vertically polarized ($\mathbf{e}_V$) components of the signal field from each isotope. The collecting mode of the signal field is about 150 μm waist inside the MOT.

Referring to Fig. 22, PMs 1 and 4 are driven at 531.5 MHz, and PMs 2 and 3 are driven at 1368 MHz. The phase shift is monitored by using two additional rf sources that differ from the driving frequencies by several MHz, then combining the two signals on a frequency mixer. Let us take the signal rf as ω_1 with some initial phase ϕ_0 and the reference rf as ω_2 with the initial phase 0. The mixer will transform

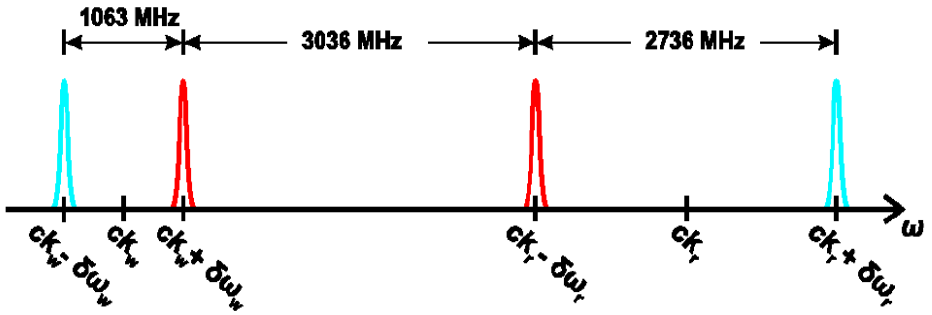

Figure 24: The left red peak is ^{85}Rb $F = 3 \rightarrow F' = 3$; the right red peak is ^{85}Rb $F = 2 \rightarrow F' = 3$; the left cyan peak is ^{87}Rb $F = 2 \rightarrow F' = 2$; and the right cyan peak is ^{87}Rb $F = 1 \rightarrow F' = 2$

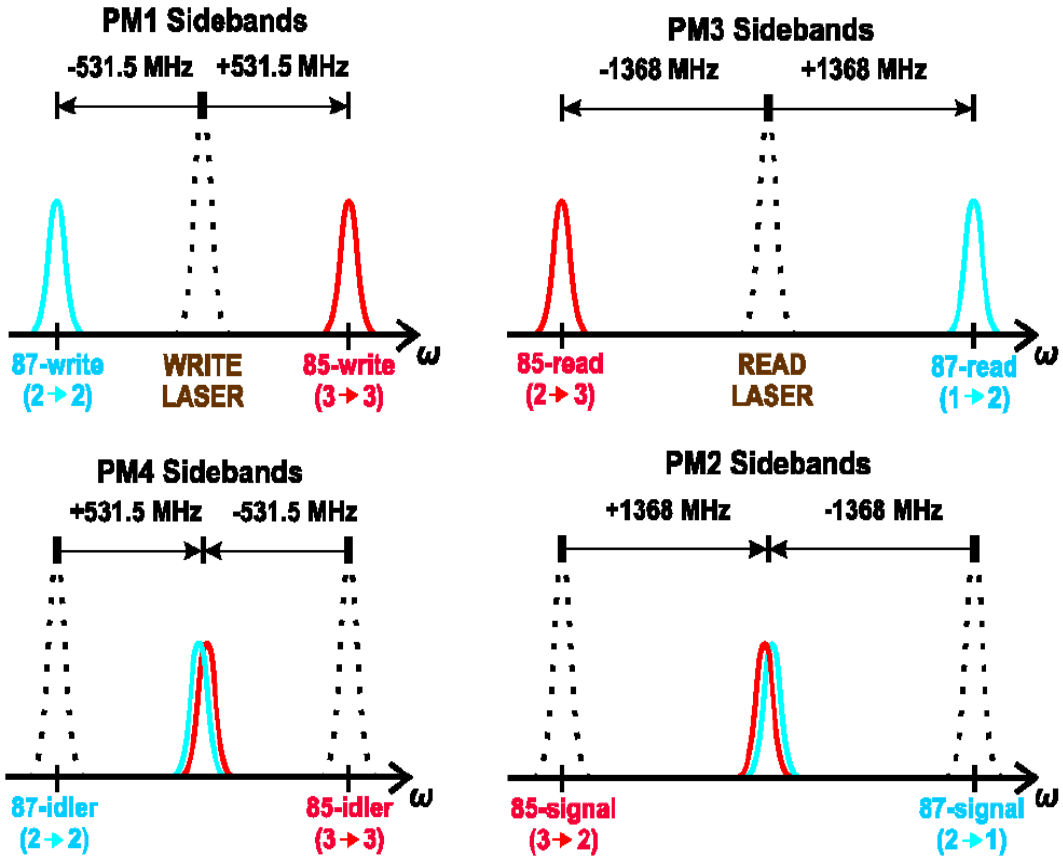

Figure 25: Representation of the PMs for write, read, idler and signal.

the signals in the following way:

$$\sin(\omega_1 + \phi_0)\sin(\omega_2) = \frac{1}{2}[\cos(\omega_1 - \omega_2 + \phi_0) - \cos(\omega_1 + \omega_2 + \phi_0)]. \tag{49}$$

The second term of the sum frequency component at the mixer output is filtered out by a regular 100 MHz bandwidth oscilloscope. The difference frequency component is monitored with appropriate resolution. In this way, the phase of the driving frequency is transferred to the phase of the difference frequency component. We choose a 5 MHz difference for the beating, which corresponds to a 20 ns period in the time domain.

The phase shift is controlled by a mechanical phase shifter (Pasternack PE8243) with a frequency range from DC to 2 GHz and phase adjustment of 60° per GHz. As the range of the phase shifter is not sufficient to rotate the whole period, we employ BNC extensions to accomplish a coarse phase shift and use the mechanical phase shifter for fine adjustment. As shown in Fig. 26, the rf signal in each channel is split in half. One half is used to drive the PM and the other half is used for the phase monitor. The rf insertion loss from a phase shifter depends on the phase change between input and output rf signals; we compensate for this effect with a passive rf attenuator.

To characterize the nonclassical correlations of this system, the signal field is sent to an electro-optic phase modulator (PM2 in Fig. 22) driven at a frequency of $\delta\omega_s = \delta\omega_w - \left[\left(\omega_a^{(87)} - \omega_b^{(87)}\right) - \left(\omega_a^{(85)} - \omega_b^{(85)}\right)\right]/2 = 1368$ MHz. The modulator combines the two signal frequency components into a central frequency $ck_s = c(k_s^{(85)} + k_s^{(87)})/2$ with a relative phase ϕ_s. The statistics of the signal are measured by a photodetector, preceded by an optical cavity filter E1 (Fig. 22) which reflects all but the central signal frequency component.

The spin-wave qubit is measured by Raman conversion with strong vertically polarized read pulses, followed by photoelectric detection of the generated idler fields. The read pulses are produced by phase modulation of a single frequency 400 ns laser pulse using PM3 (Fig. 22). This read laser pulse is generated by the read laser

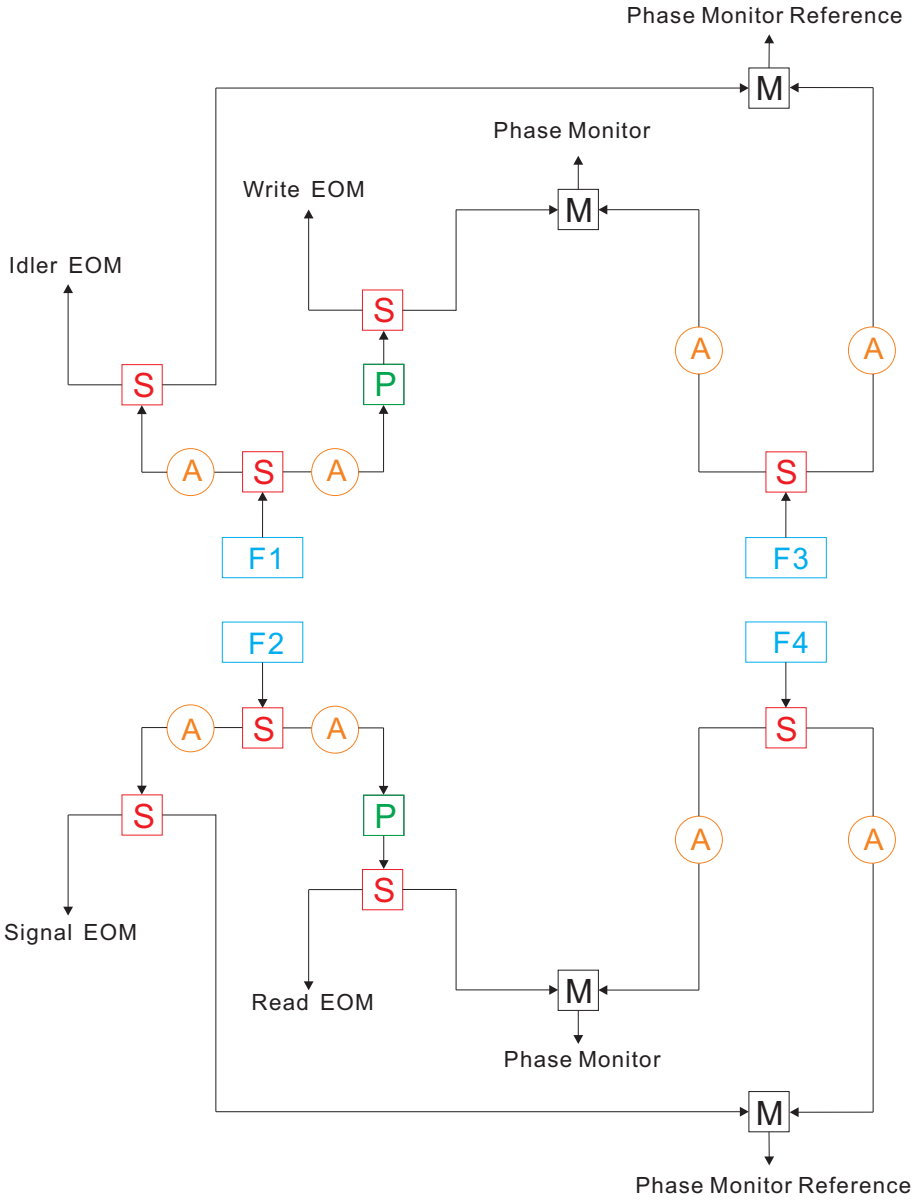

Figure 26: Diagram of the phase shifter setup. F1, F2, F3, and F4 are 531.5, 536.5, 1368, and 1363 MHz, respectively. S is the rf power splitter. P is the phase shifter. M is the frequency mixer. A is the attenuator.

switching AOM with a delay of 300 ns with respect to the write laser. The read field is coupled to the write field fiber to make sure the write and read fields are mode matched. The two sideband frequencies $ck_r^{(85)}$ and $ck_r^{(87)}$ from PM3 are resonant on the $\left|b^{(85)}\right\rangle \leftrightarrow \left|c^{(85)}\right\rangle$ and $\left|b^{(87)}\right\rangle \leftrightarrow \left|c^{(87)}\right\rangle$ transitions, respectively. The read process results in the transfer of the spin-wave excitations to horizontally polarized idler photons emitted in the phase matched directions

$$\mathbf{k}_i^{(\nu)} = \mathbf{k}_w^{(\nu)} - \mathbf{k}_s^{(\nu)} + \mathbf{k}_r^{(\nu)}. \tag{50}$$

This relation is satisfied by coupling the signal field collection fiber into the idler field collection fiber with 75% coupling efficiency.

A fourth phase modulator, PM4, driven at a frequency $\delta\omega_i = \delta\omega_w - (\Delta_{85} + \Delta_{87})/2 = 531.5$ MHz, combines the idler frequency components into a sideband with frequency $ck_i = c(k_i^{(85)} + k_i^{(87)})/2$ with a relative phase ϕ_i. The combined idler field is measured by a photon counter preceded by a frequency filter (an optical cavity, E2 in Fig. 22) which only transmits fields of the central frequency ck_i. The write-read protocol in our experiment is repeated $2 \cdot 10^5$ times per second.

The effective state of this process can be written in the following form [59]:

$$|\psi\rangle_{eff} \sim \cos\eta|85\rangle_s|85\rangle_i + \sin\eta e^{i(\phi_i - \phi_s + \phi_o)}|87\rangle_s|87\rangle_i, \tag{51}$$

where $|85\rangle_s$ and $|87\rangle_s$ represent the Raman photon scattered from ^{85}Rb and ^{87}Rb, respectively. The states of the idler fields are $|85\rangle_i$ and $|87\rangle_i$.

3.6 Analysis

3.6.1 Coincidence Detection

The unitary operator responsible for scattering into the collected signal mode is given, following Ref. [59], by

$$\hat{U} = \exp(\chi\cos\eta\ \hat{a}^{(85)\dagger}\hat{s}^{(85)\dagger} + \chi\sin\eta\ \hat{a}^{(87)\dagger}\hat{s}^{(87)\dagger} - H.c.), \tag{52}$$

where χ is a dimensionless interaction parameter, $\hat{a}^{(\nu)}$ is the discrete signal mode bosonic annihilation operator, η is the parametric mixing angle, and $\hat{s}^{(\nu)}$ is the atomic spin-wave annihilation operator. Here, $\hat{a}^{(\nu)} = \int dt \varphi^*(t) \hat{\psi}_s^{(\nu)}(t)$ is the discrete signal mode bosonic annihilation operator, $\varphi(t)$ is the temporal profile of the field, and $\hat{\psi}_s^{(\nu)}(t)$ is the signal field annihilation operator.

When the write pulse is sufficiently weak, the fields can be approximated as

$$\hat{a}^{(85)out} \simeq \hat{a}^{(85)in} - \chi \cos\eta \hat{s}^{(85)\dagger in}, \tag{53}$$

$$\hat{a}^{(87)out} \simeq \hat{a}^{(87)in} - \chi \sin\eta \hat{s}^{(87)\dagger in}, \tag{54}$$

$$\hat{s}^{(85)out} \simeq \hat{s}^{(85)in} - \chi \cos\eta \hat{a}^{(85)\dagger in}, \tag{55}$$

$$\hat{s}^{(87)out} \simeq \hat{s}^{(87)in} - \chi \sin\eta \hat{a}^{(87)\dagger in}. \tag{56}$$

The detected signal field is described by the bosonic field operator

$$\begin{aligned} \hat{a}_s(\phi_s) &= \sqrt{\frac{\epsilon_s^{(85)}}{2}} e^{-i\phi_s/2} \hat{a}^{(85)out} + \sqrt{\frac{\epsilon_s^{(87)}}{2}} e^{i\phi_s/2} \hat{a}^{(87)out} \\ &+ \sqrt{\frac{1-\epsilon_s^{(85)}}{2}} e^{-i\phi_s/2} \hat{\xi}_s^{(85)} + \sqrt{\frac{1-\epsilon_s^{(87)}}{2}} e^{i\phi_s/2} \hat{\xi}_s^{(87)}, \end{aligned} \tag{57}$$

where $\epsilon_s^{(\nu)} \in [0,1]$ is the signal efficiency including propagation losses and losses to other frequency sidebands within PM2, and $\hat{\xi}_s^{(\nu)}$ represents concomitant vacuum noise.

We treat the retrieval dynamics using the effective beam splitter relations

$$\hat{b}^{(\nu)} = \sqrt{\epsilon_r^{(\nu)}} \hat{s}^{(\nu)out} + \sqrt{1-\epsilon_r^{(\nu)}} \hat{\xi}_r^{(\nu)}, \tag{58}$$

where $\epsilon_r^{(\nu)}$ is the retrieval efficiency of the spin wave stored in the isotope $^{\nu}$Rb, $\hat{b}^{(\nu)} = \int dt \varphi_i^{(\nu)*}(t) \hat{\psi}_i^{(\nu)}(t)$ is the discrete idler bosonic operator for an idler photon of frequency $ck_i^{(\nu)}$, $\varphi_i^{(\nu)}(t)$ is the temporal profile of an idler photon emitted from the $^{\nu}$Rb spin wave (normalized to unity), and $\hat{\psi}_i^{(\nu)}(t)$ is the annihilation operator for an idler photon emitted at time t.

The detected idler field is described by the bosonic field operator

$$\begin{aligned}
\hat{a}_i(\phi_i) &= \sqrt{\frac{\epsilon_i^{(85)}}{2}} e^{i\phi_i/2} \hat{b}^{(85)} + \sqrt{\frac{\epsilon_i^{(87)}}{2}} e^{-i\phi_i/2} \hat{b}^{(87)} \\
&+ \sqrt{\frac{1-\epsilon_i^{(85)}}{2}} e^{i\phi_i/2} \hat{\xi}_i^{(85)} + \sqrt{\frac{1-\epsilon_i^{(87)}}{2}} e^{-i\phi_i/2} \hat{\xi}_i^{(87)} \\
&= \sqrt{\frac{\epsilon_i^{(85)}}{2}} e^{i\phi_i/2} [\sqrt{\epsilon_r^{(85)}} \hat{s}^{(85)out} + \sqrt{1-\epsilon_r^{(85)}} \hat{\xi}_r^{(85)}] \\
&+ \sqrt{\frac{\epsilon_i^{(87)}}{2}} e^{-i\phi_i/2} [\sqrt{\epsilon_r^{(87)}} \hat{s}^{(87)out} + \sqrt{1-\epsilon_r^{(87)}} \hat{\xi}_r^{(87)}] \\
&+ \sqrt{\frac{1-\epsilon_i^{(85)}}{2}} e^{i\phi_i/2} \hat{\xi}_i^{(85)} + \sqrt{\frac{1-\epsilon_i^{(87)}}{2}} e^{-i\phi_i/2} \hat{\xi}_i^{(87)}
\end{aligned} \tag{59}$$

where $\epsilon_i^{(\nu)} \in [0,1]$ is the idler efficiency including propagation losses and losses to other frequency sidebands within PM4, and $\hat{\xi}_i^{(\nu)}$ represents associated vacuum noise.

The signal-idler correlations result in phase-dependent coincidence rates given, up to detection efficiency factors, by

$$C_{si}(\phi_s, \phi_i) = \left\langle \hat{a}_s^\dagger(\phi_s) \hat{a}_i^\dagger(\phi_i) \hat{a}_i(\phi_i) \hat{a}_s(\phi_s) \right\rangle. \tag{60}$$

From the state of the atom-signal system after the write process, we calculate the coincidence rates to the second order in the dimensionless interaction parameter χ,

$$\begin{aligned}
&C_{si}(\phi_s, \phi_i) \\
&= \frac{\chi^2}{4} [\epsilon_r^{(87)} \epsilon_i^{(87)} \epsilon_s^{(87)} \sin^2\eta \left\langle \hat{b}^{(87)} \hat{b}^{(87)\dagger} \hat{b}^{(87)} \hat{b}^{(87)\dagger} \right\rangle \\
&\quad + \epsilon_r^{(85)} \epsilon_i^{(85)} \epsilon_s^{(85)} \cos^2\eta \left\langle \hat{b}^{(85)} \hat{b}^{(85)\dagger} \hat{b}^{(85)} \hat{b}^{(85)\dagger} \right\rangle \\
&\quad + \sqrt{\epsilon_r^{(85)} \epsilon_i^{(85)} \epsilon_s^{(85)} \epsilon_r^{(87)} \epsilon_i^{(87)} \epsilon_s^{(87)}} \sin\eta \cos\eta \left\langle \hat{b}^{(85)} \hat{b}^{(85)\dagger} \hat{b}^{(87)} \hat{b}^{(87)\dagger} \right\rangle e^{-i(\phi_i - \phi_s)} \\
&\quad + \sqrt{\epsilon_r^{(85)} \epsilon_i^{(85)} \epsilon_s^{(85)} \epsilon_r^{(87)} \epsilon_i^{(87)} \epsilon_s^{(87)}} \sin\eta \cos\eta \left\langle \hat{b}^{(87)} \hat{b}^{(87)\dagger} \hat{b}^{(85)} \hat{b}^{(85)\dagger} \right\rangle e^{i(\phi_i - \phi_s)}] \\
&= \frac{\chi^2}{4} [\mu^{(85)} \cos^2\eta + \mu^{(87)} \sin^2\eta \\
&+ \Upsilon \sqrt{\mu^{(85)} \mu^{(87)}} \sin 2\eta \cos(\phi_i - \phi_s + \phi_0)],
\end{aligned} \tag{61}$$

where $\mu^{(\nu)} \equiv \epsilon_r^{(\nu)}\epsilon_i^{(\nu)}\epsilon_s^{(\nu)}$ accounts for all the loss, including the retrieval efficiency of the spin wave stored in the atoms, propagation losses, and losses to other frequency sidebands. Here, Υ and ϕ_0 represent a real amplitude and phase, respectively, such that

$$\Upsilon e^{-i\phi_0} \equiv e^{-\left(\delta\phi_s^2+\delta\phi_i^2\right)/2}\int dt\varphi_i^{(85)*}(t)\varphi_i^{(87)}(t). \tag{62}$$

We account for classical phase noise in the rf driving of the phase modulator pairs PM1,4 and PM2,3, by treating ϕ_s and ϕ_i as Gaussian random variables with variances $\delta\phi_s^2$ and $\delta\phi_i^2$ respectively. When the write fields are detuned such that the rates of correlated signal-idler coincidences are equal,

$$\mu^{(85)}\cos^2\eta = \mu^{(87)}\sin^2\eta, \tag{63}$$

the fringe visibility is maximized, and Eq. (61) reduces to

$$C_{si}(\phi_s,\phi_i) = \frac{\chi^2}{2}\mu^{(85)}\cos^2\eta[1+\Upsilon\cos(\phi_i-\phi_s+\phi_0)]. \tag{64}$$

Fig. 27 shows coincidence fringes as a function of ϕ_i taken for two different values of ϕ_i. The detection rates measured separately for ^{85}Rb and ^{87}Rb were (a) 53 Hz and 62 Hz on D1 and (b) 95 Hz and 107 Hz on D2, respectively. These rates correspond to a level of random background counts about 2.5 times lower than the minima of the interference fringes. This implies that the observed value of visibility $\Upsilon = 0.86$ cannot be accounted for by random photoelectric coincidences alone. The additional reduction of visibility may be due to variations in the idler phases caused by temporal variations in the cloud densities during data accumulation, while the effects of rf phase noise are believed to be negligible.

3.6.2 Bell's Inequality Violation

Following the discussion in Chapter I, we calculate the correlation function $E(\phi_s,\phi_i)$, given by

$$E(\phi_s,\phi_i) = \frac{C_{si}(\phi_s,\phi_i) - C_{si}(\phi_s,\phi_i^\perp) - C_{si}(\phi_s^\perp,\phi_i) + C_{si}(\phi_s^\perp,\phi_i^\perp)}{C_{si}(\phi_s,\phi_i) + C_{si}(\phi_s,\phi_i^\perp) + C_{si}(\phi_s^\perp,\phi_i) + C_{si}(\phi_s^\perp,\phi_i^\perp)}, \tag{65}$$

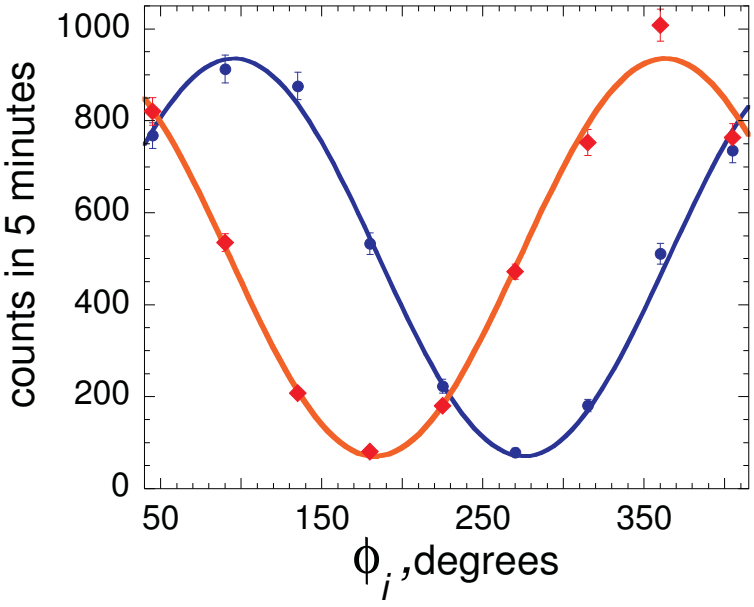

Figure 27: Measured $C_{si}(\phi_s, \phi_i)$ as a function of ϕ_i for $\phi_s = 0$, diamonds and for $\phi_s = \pi/2$, circles. The angle ϕ_0 is absorbed into the arbitrary definition of the origin, i.e., ϕ_0 is defined to be zero. Solid lines are sinusoidal fringes based on Eq. (64) with $\Upsilon = 0.86$. Single channel counts of D1 and D2 show no dependence on the phases.

where $\phi^{\perp}_{s[i]} = \phi_{s[i]} + \pi$. One finds that a classical local hidden variable theory yields the Bell inequality $|S| \leq 2$, where

$$S \equiv E(\phi_s, \phi_i) - E(\phi'_s, \phi_i) - E(\phi_s, \phi'_i) - E(\phi'_s, \phi'_i). \tag{66}$$

Using Eq. (64), the correlation function is given by

$$E(\phi_s, \phi_i) = \Upsilon \cos(\phi_s - \phi_i + \phi_0). \tag{67}$$

Choosing, e.g., the angles $\phi_s = -\phi_0$, $\phi_i = \pi/4$, $\phi'_s = -\phi_0 - \pi/2$, and $\phi'_i = 3\pi/4$, we find the Bell parameter $S = 2\sqrt{2}\Upsilon$. Table 2 presents measured values for the correlation function $E(\phi_s, \phi_i)$ using the canonical set of angles ϕ_s, ϕ_i. We find $S_{exp} = 2.44 \pm 0.04 \not\leq 2$: a clear violation of the Bell's inequality. This value of S_{exp} is consistent with the visibility of the fringes $\Upsilon \approx 0.86$ shown in Fig. 27. This agreement supports our observation that systematic phase drifts are negligible. We emphasize that no active phase stabilization of any optical frequency field is employed. Figs. 28

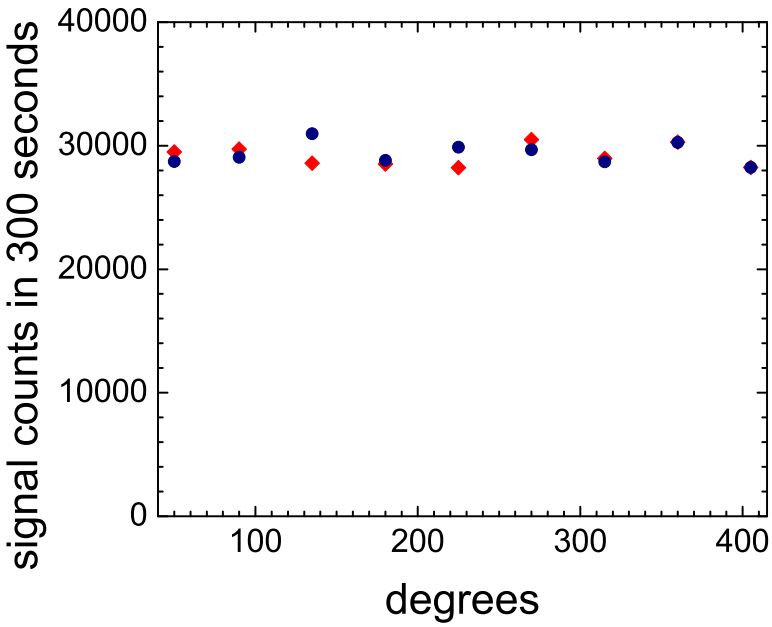

Figure 28: Measured signal counts as a function of ϕ_i for $\phi_s = 0$, diamonds and for $\phi_s = -\pi/2$, circles.

Table 2: Measured correlation function $E(\phi_s, \phi_i)$ and S for $\Delta t = 150$ ns delay between write and read pulses; all the errors are based on the statistics of the photon counting events.

ϕ_s	ϕ_i	$E(\phi_s, \phi_i)$
0	$\pi/4$	0.629 ± 0.018
0	$3\pi/4$	-0.591 ± 0.018
$-\pi/2$	$\pi/4$	-0.614 ± 0.018
$-\pi/2$	$3\pi/4$	-0.608 ± 0.018
		$S_{exp} = 2.44 \pm 0.04$

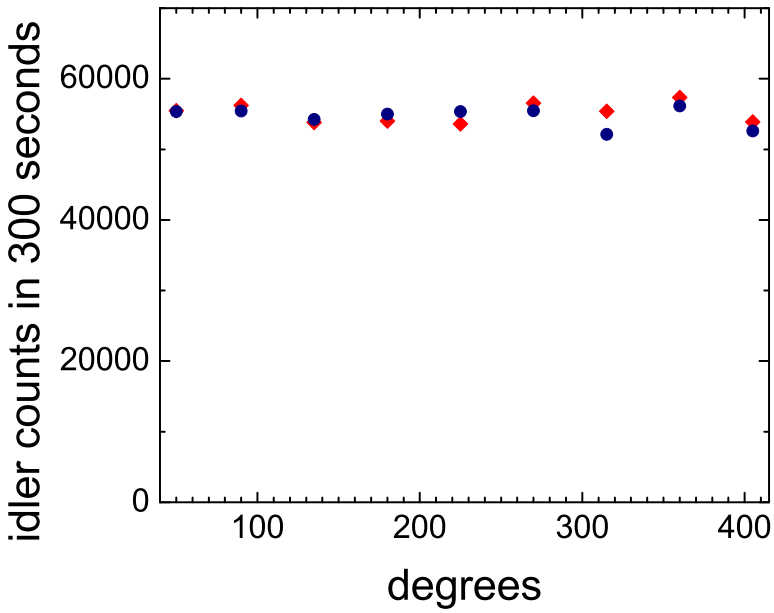

Figure 29: Measured idler counts as a function of ϕ_i for $\phi_s = 0$, diamonds and for $\phi_s = -\pi/2$, circles.

and 29 show the measured signal and idler count rates. These exhibit no discernible fringes.

CHAPTER IV

MULTIPLEXED QUANTUM ELEMENTS

Extending the communication length to continental distances is possible by employing the quantum repeater architecture [24]. However, due to the probabilistic nature of the photon sources, finite quantum memory, and other technical limitations, it is still unlikely that the communication rate will be sufficient for practical purposes. The presence of multiple memory elements per node in a quantum repeater allows dynamic reallocation of resources, improving the rate of quantum communication for short memory times [75]. Here, we describe the first implementation of multiple memory elements in a single cold atomic sample. Individual addressing is achieved by one dimensional scanning with acousto-optical deflectors (AODs). This allows for the demonstration of matter-light entanglement using an arbitrary pair of memory elements in the array.

4.1 Memory-Insensitive Multiplexed Quantum Repeater

Consider a quantum repeater consisting of n quantum elements in each node. Entanglement generation is attempted for each pair of quantum elements in each basic segment, either scanning or simultaneously. Because the time for the signal to propagate to the center station between two neighboring nodes is much longer than the switching time of the different elements, the difference of entanglement generation rates between scanning and simultaneous attempts is negligible. Once one of the element pairs is entangled, other pairs of elements are still attempting entanglement generation, while the entanglement is stored and waiting for entanglement from the neighboring node. The entanglement connection can be either parallel or multiplexed,

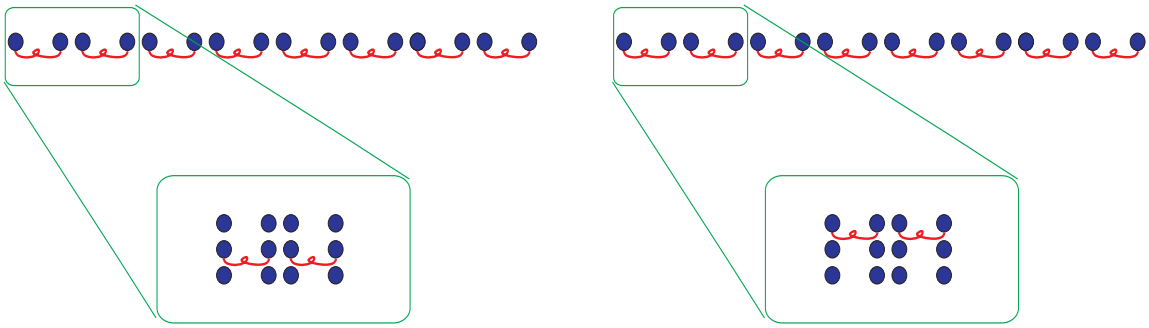

(a) Entanglement connection happens on the middle elements pair.

(b) Entanglement connection happens on the top elements pair.

Figure 30: Parallel quantum repeater.

as shown in Fig. 30 and Fig. 31. In the parallel scheme, an entanglement connection can only be made between directly neighboring elements, and the entanglement distribution rate is only n times faster than for the single quantum element scheme and requires n times more physical resources. On the other hand, an entangled element pair in the multiplexed quantum repeater connects to the element pair that is entangled first.

In Ref. [75], an example with practical parameters is analyzed to demonstrate that the difference between a parallel and a multiplexed quantum repeater is significant in the intermediate memory time regime. It compares the entanglement distribution rate of a 1000 km, N=3 quantum repeater. For multiplexing with $n \geq 10$, the rate is essentially constant for coherence times over 100 ms, while for parallel quantum repeater systems, it decreases by 2 orders of magnitude. For memory coherence times within 250 ms, a greater entanglement distribution rate is achieved by multiplexing ten memory element pairs per segment, rather than parallelizing 1000.

4.2 Quantum Memory Array

4.2.1 Scanning Tools

The acousto-optical deflector (AOD) has been widely used in scanning experiments. With its fast switching time, it is possible to scan from one mode to another in

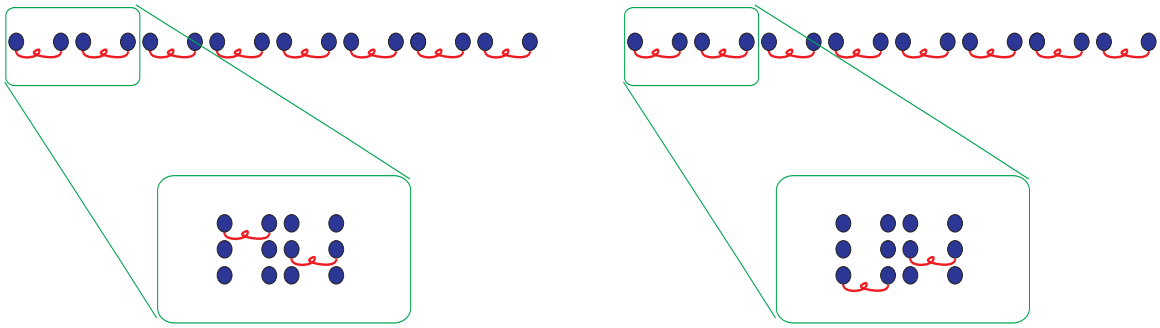

(a) (b)

Figure 31: Multiplexed quantum repeater. Entanglement connection can happen on the top elements pair.

the sub-microsecond regime. We used customized AODs (45050-5-6.5DEG-.8) from NEOS Technologies. They are designed to have flat diffraction efficiency across the full 30 MHz bandwidth. The bandwidth is centered on 50 MHz, and the acoustic speed is 0.6 mm/μs. If an acousto-optical device is operated at the Bragg angle corresponding to a drive frequency ω_s, then variation of ω_s will lead to variation in the diffraction angle, thereby serving to deflect or scan the diffracted beam. The variation from ω_s to $\omega_s + \Delta\omega_s$ will change the deflecting angle from θ to $\theta + \Delta\theta$. For small deflection angles, the Bragg condition gives

$$\Delta\theta = \frac{\Delta k_S}{k}, \tag{68}$$

where $k_S = 2\pi f_s/v_s$ and $k = 2\pi/\lambda$.

The characteristics of a beam scanner are frequently determined by the number of resolvable deflected spots N that it can contain. For a Gaussian beam of waist diameter

$$D = \frac{4\lambda}{\pi\theta_{beam}} \tag{69}$$

focused at the Bragg angle

$$N = \frac{\Delta\theta_{max}}{\theta_{beam}} = \frac{\pi D\Delta\theta_{max}}{4\lambda}, \tag{70}$$

the maximum deflection angle is

$$\Delta\theta_{max} = \frac{\Delta k_{S,max}}{k} = \frac{\lambda \Delta f_{max}}{v_s}, \tag{71}$$

where v_s is the acoustic velocity. We find that

$$N = (\frac{\pi}{4})\tau \Delta f_{max}, \tag{72}$$

where $\tau = \frac{D}{v_s}$. The maximum number of resolvable spots is approximately given by the maximum number of distinguishable angles by which the incident beam is deflected.

4.2.2 Multi-Mode Four Wave Mixing Alignment

The first task of the alignment is to change the MOT to a pancake shape in the beam steering plane. This allows for a large effective interaction area for the multi-mode elements. We apply half of the trapping light along the axis of trapping coils, which is the z-axis in our setup. This introduces more trapping force, which acts to squeeze the MOT in the z-direction.

The write beam is steered in the plane that is perpendicular to the z-axis. The center frequency of the AOD is 50 MHz, so we use this frequency as the reference to maximize the absorption position inside the MOT that is defined as the center of the scanning range. We implement the telecentric scanning method as shown in Fig. 32, where a Fourier lens is placed after the AOD so that the write beams after the lens are parallel [76]. The write beams are then coupled into the read fiber through the read AOD. In order to combine the scanning write beams into a single spatial mode after the read AOD, the latter has to be aligned in a specific configuration. An example with two spatial modes is shown in Fig. 33. The Bragg condition for the +1 or -1 order is satisfied depending on the direction of the AOD.

A signal beam on the read transition separated from the write beam by 3° is sent into the atomic ensembles. The write, read, and signal beams intersect inside the

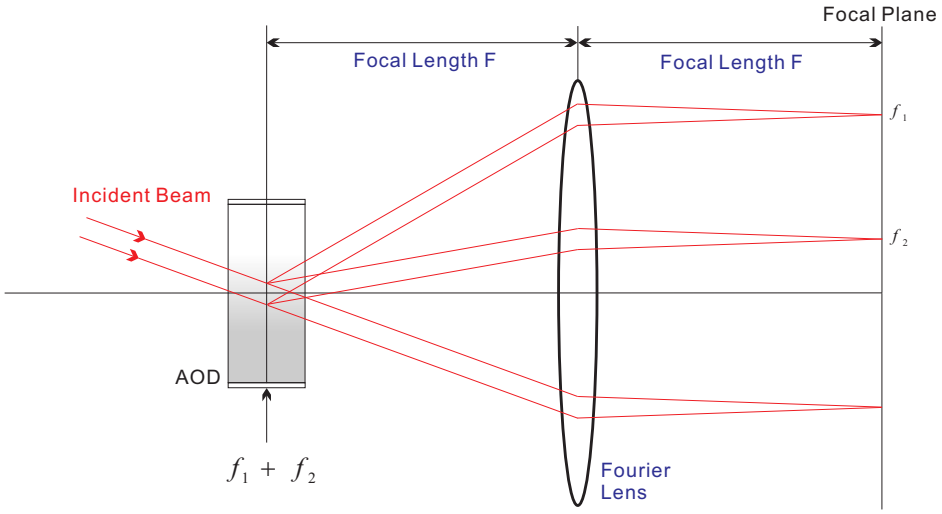

Figure 32: Setup for the telecentric scanning : The pivot (AOD) of the scanning system is located at the front focal point of the lens.

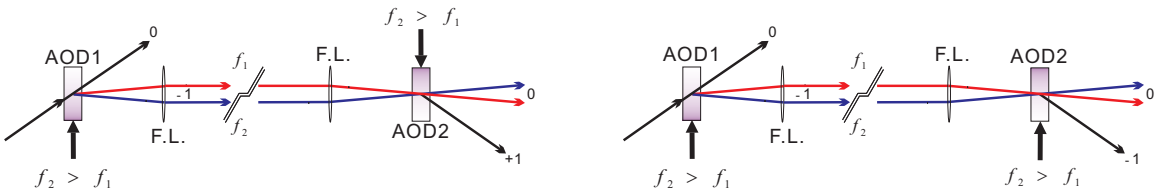

Figure 33: Backward alignment of AOD.

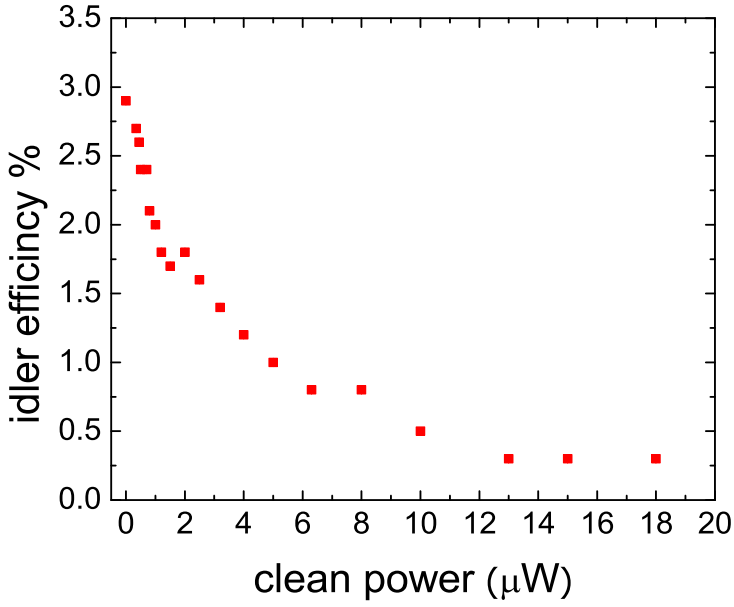

Figure 34: Measured idler efficiency as a function of optical power. A clean pulse is sent right before the read pulse to destroy the atomic excitation. The clean pulse is 200 ns long. The read pulse is 200 ns long with 300 μW power . The write/read beam waist is 115 μm.

MOT. The auxiliary field is generated in the reverse direction of the signal beam according to the phase matching condition and is detected by a CCD camera. The auxiliary field intensity is optimized by steering the signal beam. The auxiliary field signal is first checked with 50 MHz beams; then, by dialing different frequencies on the rf generator, we check corresponding interaction regions to ensure that the four wave mixing condition is still fulfilled. The signal beams are then coupled into the fiber through the idler AOD.

4.2.3 Reinitialization of Atomic Excitation

Within the DLCZ scheme, the write pulse that excites the atomic ensemble may not be accompanied by a detected signal photon. In this situation, we need to employ a clean pulse to pump the atomic excitation back to the original state and discard this trial. In a multiplexed quantum repeater, there are multiple quantum elements inside

a quantum node. When one of the quantum elements is prepared, excitations are still being attempted on the neighboring elements. In order to obtain the maximum number of elements, we need to minimize the separation distance between them. However, elements too close to each other will result in the atomic excitations being destroyed in the clean process. As a result, we need to send the minimum power required to clean the atomic excitation, which also maximizes the number of the quantum elements.

The timing sequence of the clean power measurement starts by sending a 400 ns write pulse to prepare the atomic excitation. Then, 200 ns later, a 200 ns clean pulse with a different power is used to spoil the atomic excitation. A 200 ns, 300 μW read pulse follows the clean pulse to map the atomic excitation into the idler field. The idler efficiency measured with different clean pulse powers is shown in Fig 34.

4.2.4 Laser Setup

The spatial scanning of the AOD over different quantum elements is also accompanied by frequency change of the write/read pulses. However, the photon pair correlations in the DLCZ protocol are very sensitive to the detuning of the write pulse. It is desirable to have uniform level of photon pair correlations over the quantum elements. In order to achieve this, the switching AOM of a normal laser setup is also used to compensate for the frequency change. The switching AOM is set up in the double pass configuration so that the change in frequency will not cause a change in the fiber coupling efficiency, as shown in Fig 35. The write and read switching AOMs are on the +1 order with 80 MHz driving frequency.

4.2.5 Minimization of Stray Magnetic Field with Larmor Precession

The spin wave coherence of the atomic excitation is sensitive to stray magnetic fields. In the presence of the latter, the spin wave starts to precess during storage and the coherence is lost [31, 32, 33, 35, 77, 78, 79, 80]. To prevent this, we set up 3 orthogonal

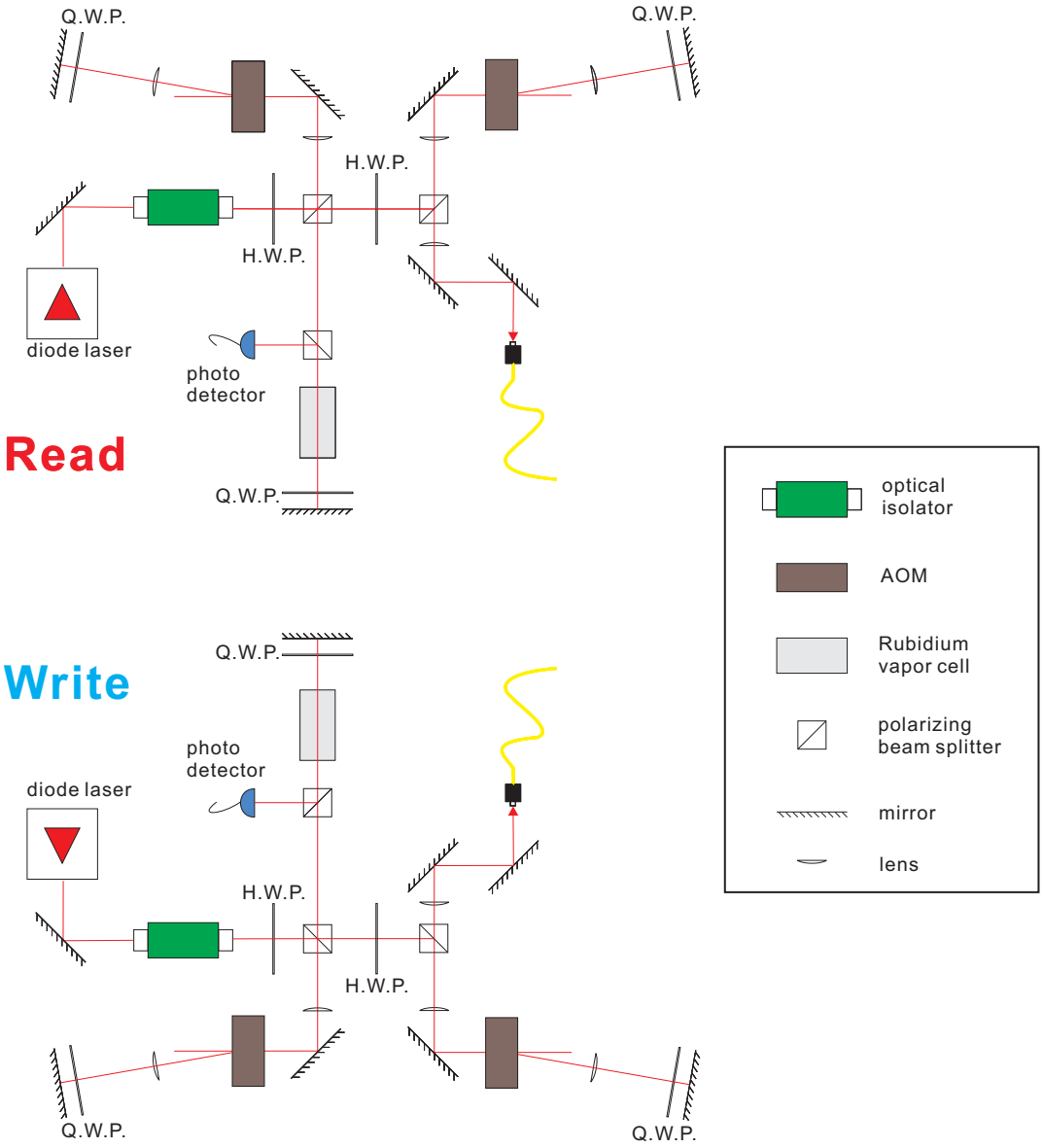

Figure 35: Schematics of write/read beam configuration. An additional switching AOM is used in the double pass configuration so that the change in frequency will not cause a change in the fiber coupling efficiency.

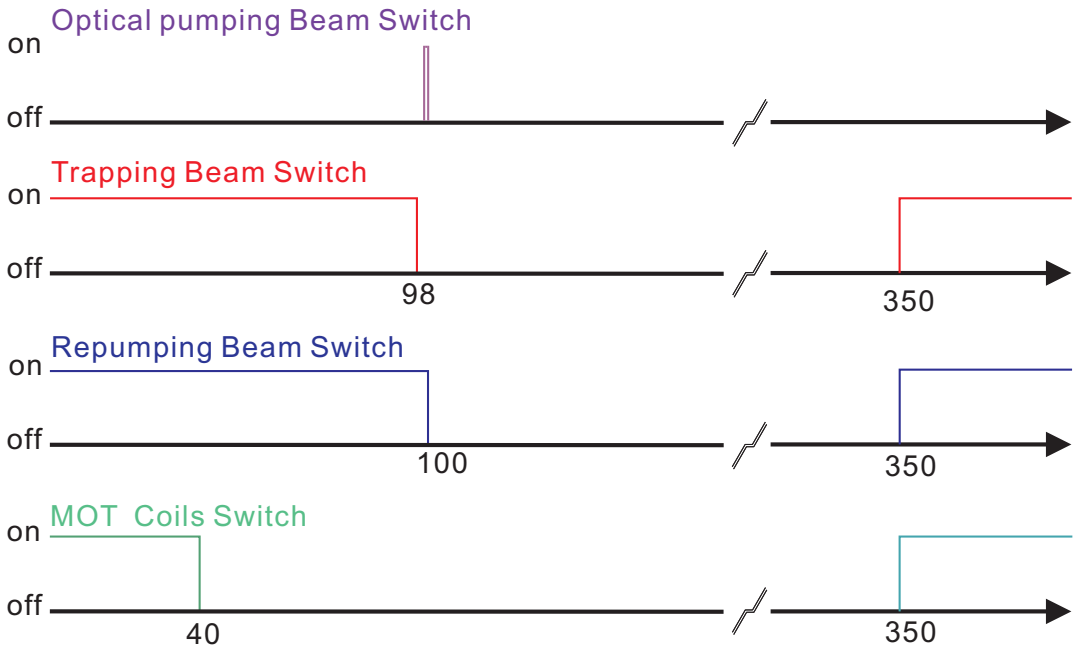

Figure 36: Timing sequence of Larmor precession measurement. The optical pumping beam is implemented for 500 ns after the trapping beam is shut off. The unit of the axis is 10 μs.

pairs of coils that compensate for any stray magnetic fields [81].

After the MOT is loaded, the ^{85}Rb atomic ensemble is initially populated equally among the $|5S_{1/2}, F = 3\rangle$ Zeeman states. The trapping beams and trapping coils are switched off during the measurement. Then, a σ^+ polarized beam with approximately 100 mW of power on the $|5S_{1/2}, F = 3\rangle \rightarrow |5P_{3/2}, F = 4\rangle$ transition is applied to prepare the atoms in the $m_F = F$ state. The polarized atoms begin to precess in the plane normal to the magnetic field as shown in Fig 37. The repumping laser of the MOT is kept on during the polarizing process. The timing sequence is shown in Fig 36.

Several microwatts of continuous wave linearly polarized laser light (probe laser) is sent into the atomic ensemble to detect the paramagnetic Faraday rotation. The probe laser is red detuned from the $|5S_{1/2}, F = 3\rangle \rightarrow |5P_{1/2}, F = 3\rangle$ transition by about 1 GHz in order to prevent the coupling of different hyperfine states. The σ^+ and σ^- polarized light experiences phase shifts ϕ_+ and ϕ_- respectively. With a given

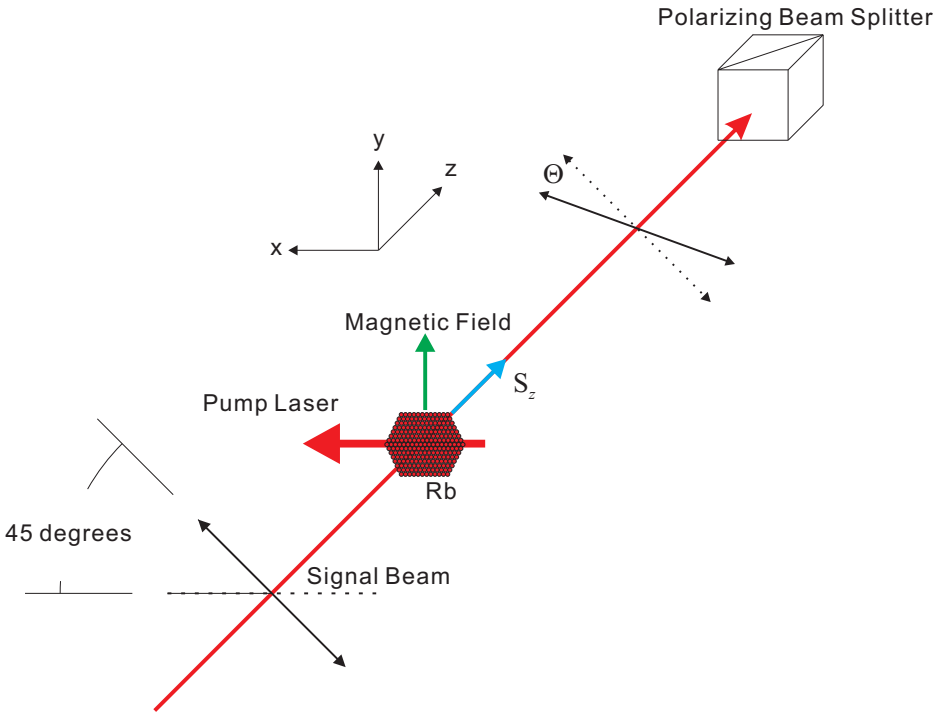

Figure 37: Setup of the Larmor precession detection in one direction. The signal beam is prepared at an angle of 45 degrees in order to gain the maximum signal.

sample length l, wavelength of the probe laser λ, and the refractive index $n^{\pm}$ of $\sigma^{\pm}$ circularly polarized light, the phase shifts are given by

$$\phi_{\pm} = \frac{2\pi l}{\lambda} n^{\pm}. \tag{73}$$

The overall rotation of the linearly polarized beam is $\Theta = (\phi_+ - \phi_-)/2$. Assuming the magnetic field $\vec{B}$ is directed along the y-axis, the atoms precess around the magnetic field $\vec{B}$ at the Larmor frequency $\omega_L = \gamma B$ in the xz-plane. In this case, the rotation angle can be expressed as

$$\Theta \sim \sin(\omega_L t) \exp(-\Gamma t), \tag{74}$$

where Γ is an introduced damping rate due to exterior influences such as a time-dependent magnetic field.

A set of polarizers is placed after the atomic ensembles and the transmitted probe signal is recorded on the photo diode. The cross section of the probe beam is approximately the size of the MOT cloud, which gives a good signal to noise ratio. The

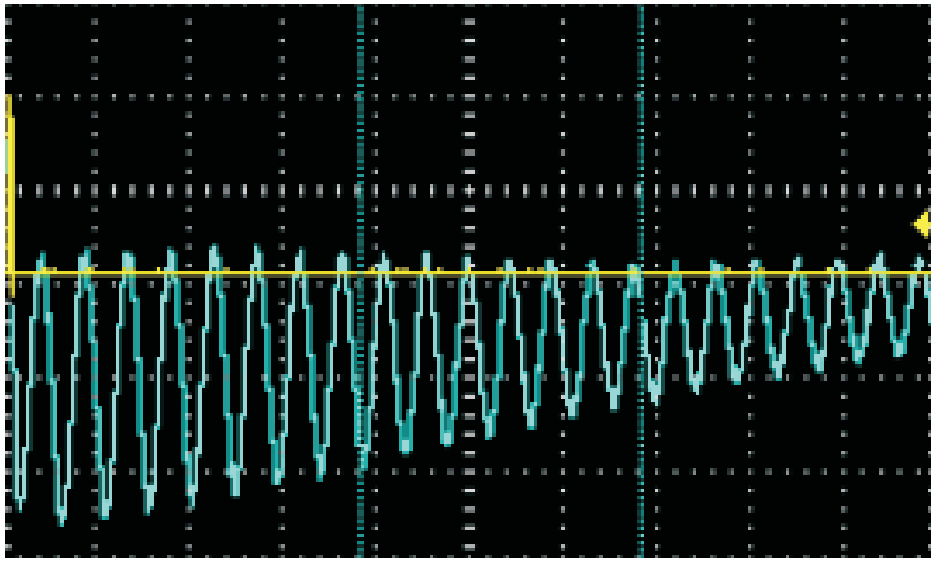

Figure 38: Averaged Larmor precession signal. The damping of the oscillation is due to a time-dependent magnetic field.

angle of the polarizer is set at 45° to the initial probe angle in order to get the best sensitivity. By adjusting currents of the three pairs of compensating coils, we are able to minimize the magnetic field in three orthogonal directions. Fig. 38 shows an example of the averaged Larmor precession signal.

4.2.6 Control System

The core of the control system in this experiment is based on a field-programmable gate array (FPGA). It is a semiconductor device containing programmable logic components and programmable interconnects. The FPGA generates the time sequence for our protocol, including the TTL pulses for the write AOM, read AOM, and clean field switching, as well as the gating for the signal and idler fields. The FPGA is also used to configure bits for the digital to analog converters (DAC). The DAC is a homemade circuit (designed by Scott Centers), as shown in Fig. 40, involving a fast setting time 8-bit DAC chip (DAC0808) combined with a high speed operational amplifier (LM7372). The DAC generates different voltage levels to drive the voltage controlled oscillator (VCO). The VCO is a commercially customized device featuring

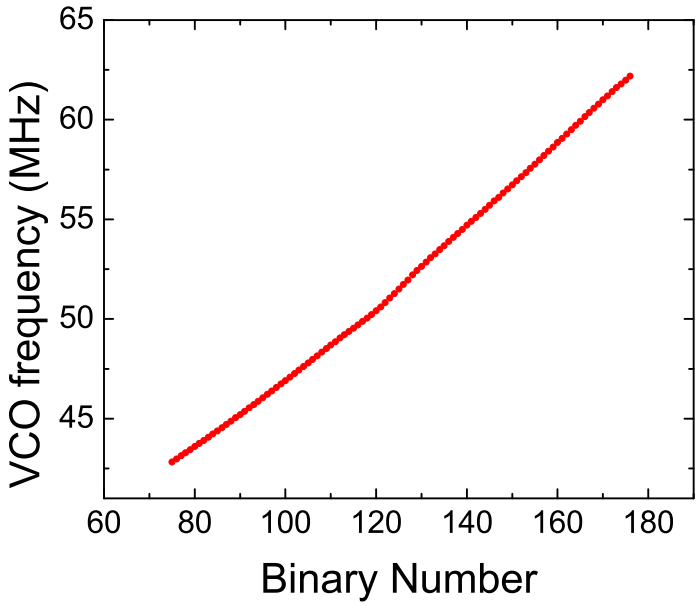

Figure 39: Output frequency as a function of DAC output binary number of the voltage controlled oscillator.

a high 3 dB bandwidth. The calibration of the frequency as the function of binary number is shown in Fig. 39.

4.2.7 Operation Protocol

The quantum memory array is illustrated in Fig. 41. The array is based on scanning the cold atomic ensemble by acousto-optical deflectors (AOD). Four separate AODs are employed to control the position of the write, read, signal, and idler beams. One pair of AODs mode-matches the write and read beam positions that constitute the addresses of micro-ensembles, while another pair collects the signal and idler photons from distinct spatial addresses. This is done by carefully aligning each write (signal) mode into the read (idler) fiber, with about 75% coupling efficiency. The positions of these four intersecting beam paths are determined by simultaneous modulation of the AOD sweeping frequencies, maintaining the requisite four-wave mixing geometry $\mathbf{k}_w^{(j)} + \mathbf{k}_r^{(j)} = \mathbf{k}_s^{(j)} + \mathbf{k}_i^{(j)}$, where the superscript j denotes a specific address.

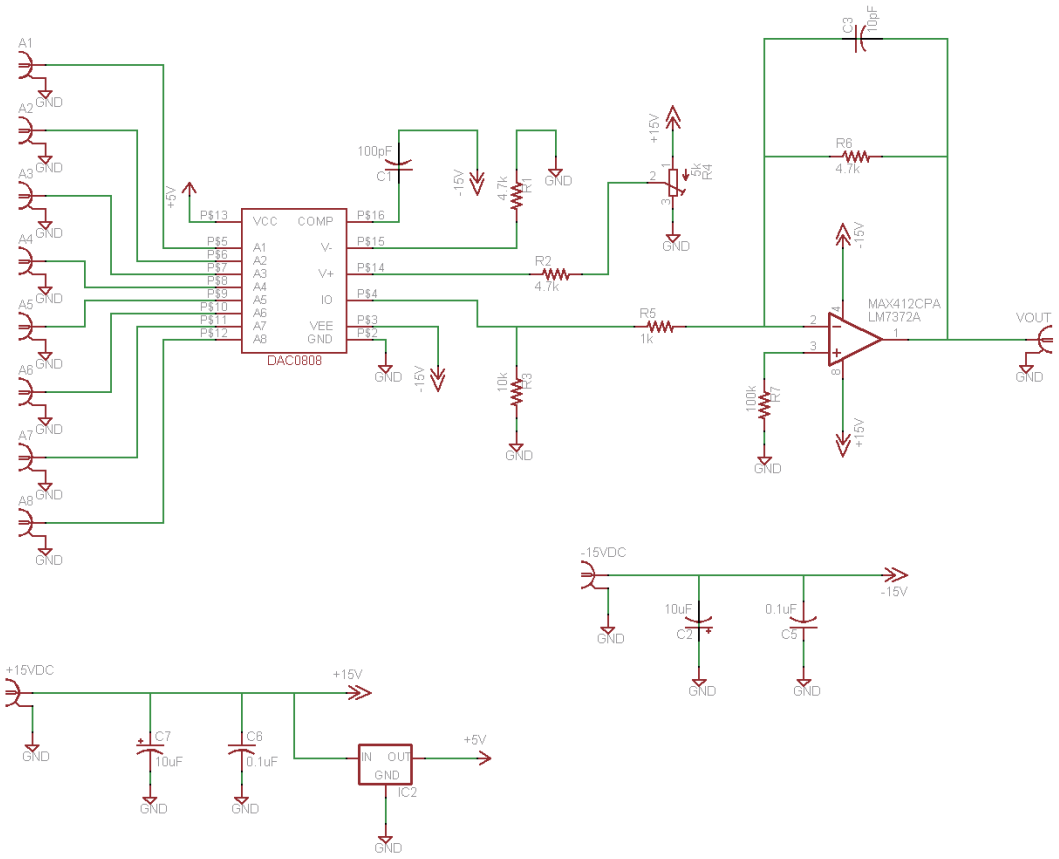

Figure 40: Circuit of digital to analog converter.

^{85}Rb atoms are prepared in the $|5S_{1/2}, F = 3\rangle$ ground level. The protocol begins when the atoms are released from the trap. The protocol control is provided by the FPGA, DAC, and VCO. We send a 12 pulse train to scan the ensemble in temporal order with the time interval 1.3 μs. The control logic changes the driving frequency of the write AOD, and in 1 μs the deflector points to the desired micro-ensemble. A 300 ns pulse, red detuned from the $|5S_{1/2}, F = 3\rangle \rightarrow |5P_{1/2}, F = 3\rangle$ transition by 10 MHz (we used an additional acousto-optical modulator to compensate the frequency shift of the write AOD), is sent to the atomic ensemble. These pulses enable individual addressing of a localized sub-region of the atomic cloud that forms a memory element. Synchronously, the signal AOD is switched to direct the signal photons from the currently addressed micro-ensemble to the single photon detector. In this way, a 12 pulse train scans the atomic array in temporal order with a time interval of 1.3 μs. Upon detection of the signal photon in the specified gate interval of 250 ns, the FPGA determines the time of this event with a resolution of 5 ns, taking into account all of the electronic and acoustic wave delays. From this time, the FPGA deduces which ensemble produced the photon.

Before reading out the excitation, in order to demonstrate the independency of each element, the control logic sends 10 read-like cleaning pulses to each of the two closest neighbors of the excited micro-ensemble. The difference in the retrieval efficiencies with and without cleaning, normalized to the original retrieval efficiency, is defined as cross-talk. Similar to the write process, read out addressing is done with the read and idler AODs. The gate interval of idler detection is 180 ns. The measured idler efficiency of different elements is shown in Fig. 42.

4.2.8 Crosstalk Measurement

The density of addressable elements is limited by the size of the write-read mode. It is 115 ± 3 μm in our case. Element addresses too close to each other increase

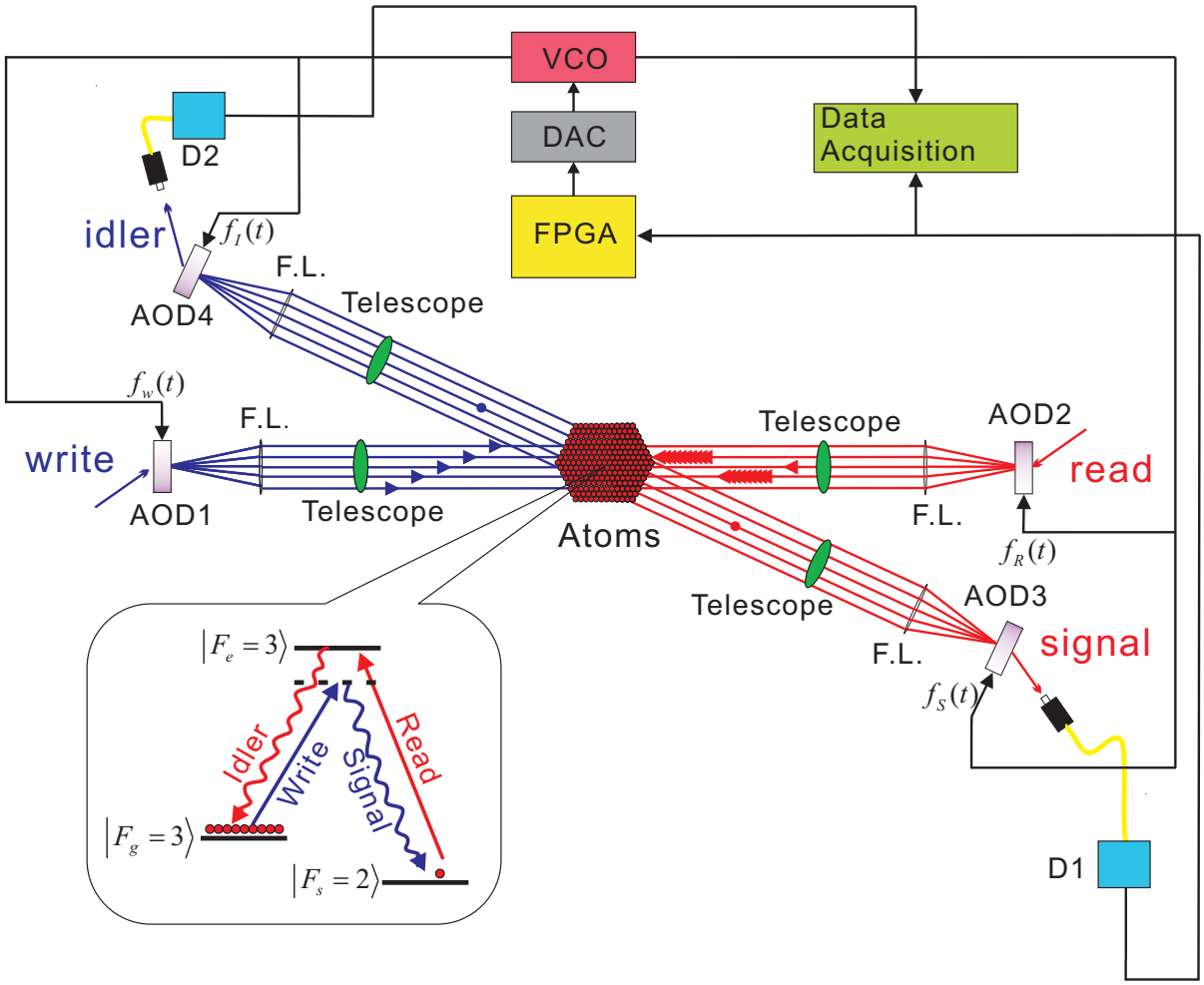

Figure 41: Experimental setup for the multimode elements: F.L. : Fourier lens; D1, D2 : photon detectors; C : fiber coupler; the inset shows the level diagram of ^{85}Rb.

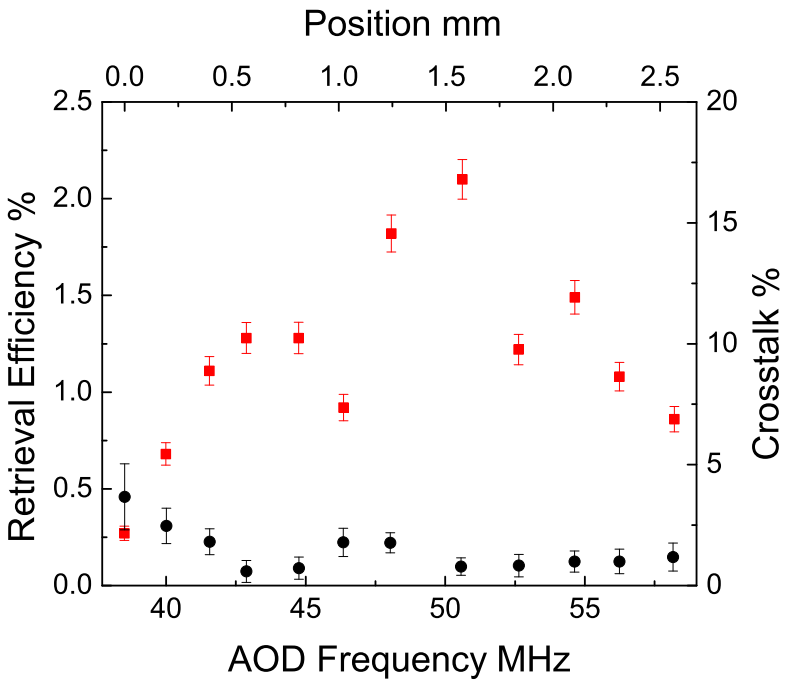

Figure 42: Measured idler efficiency for different elements: Each frequency represents a different element location. The top x-axis is AOD scanning frequencies. The bottom x-axis is the element location corresponding to an AOD scanning frequency. The right y-axis is cross-talk per clean pulse.

the probability of erasure whenever a neighboring excitation is retrieved via the read process. Separations range from a maximum of 330 μm to a minimum of 172 μm with an average of 233 μm, which results in 12 micro-ensembles overall. The measured cross-talk with a 200 ns, 10 μW clean pulse averaged over individual ensembles is $1.5 \pm 0.6\%$. We estimate the theoretical cross-talk, which comes from the excitation of the $|5S_{1/2}, F = 2\rangle$ population with the clean pulses at neighboring ensembles, by solving the optical Bloch equation numerically and integrating the scattering rate $\gamma\rho_{ee}(t)$ over the duration of a Gaussian pulse (clean pulse), where γ is the decay rate of the Rb $|5P_{1/2}, F = 3\rangle$ state, and $\rho_{ee}(t)$ is the excited state population. The expected cross-talk per clean pulse averaged over individual ensembles is $0.7 \pm 0.3\%$. The difference between the measured and expected cross-talk is due to the timing mismatch of the AOD frequency and the clean pulses. The AOD requires about 1

μs to point at the correct element. If the pulses are not perfectly positioned at the correct timing window, there is cross-talk on the target element when the AOD is switched from the left to the right neighboring element. With the cross-talk we have measured, the theoretical number of elements we should have is 14.

4.3 Matter-Light Entanglement with a Quantum Memory Array

4.3.1 Phase Control

The phase in the entanglement experiment can be easily monitored directly because the rf frequency used is only around 50 MHz, which is within the bandwidth of a typical oscilloscope. A delay generator is used to shift the phase on one of the frequencies in the entanglement experiment and capable of shifting a signal by 20 ns with a resolution of 1 ns. Accuracy under 1 ns is obtained using BNC extensions. The rf sources are provided by signal generators. They are split into different channels for different purposes. The directional couplers split 1% of rf power into the coupled output port to monitor the phase on the oscilloscope and the rest is directed to the AODs through the main output port. Symmetrization of two qubit states is the requirement of seeking a maximum entangled state. On the signal/idler AODs, we need to provide appropriate rf powers on the two frequencies in order to generate the same diffraction efficiency for the signal and idler field. We implement variable rf attenuators on each channel which provide the flexibility in rf power adjustment. The details of the phase control loop are shown in Fig. 43.

4.3.2 Experiment

The AODs can be used as dynamic beam splitters, allowing us to realize matter qubits based on pairs of elements of the memory array. The experimental setup is shown in Fig. 44. The write AOD aligned in +1 order is provided with two CW frequencies f_j and f_k ($f_j > f_k$) to generate two spatially distinct pulses. These two write pulses,

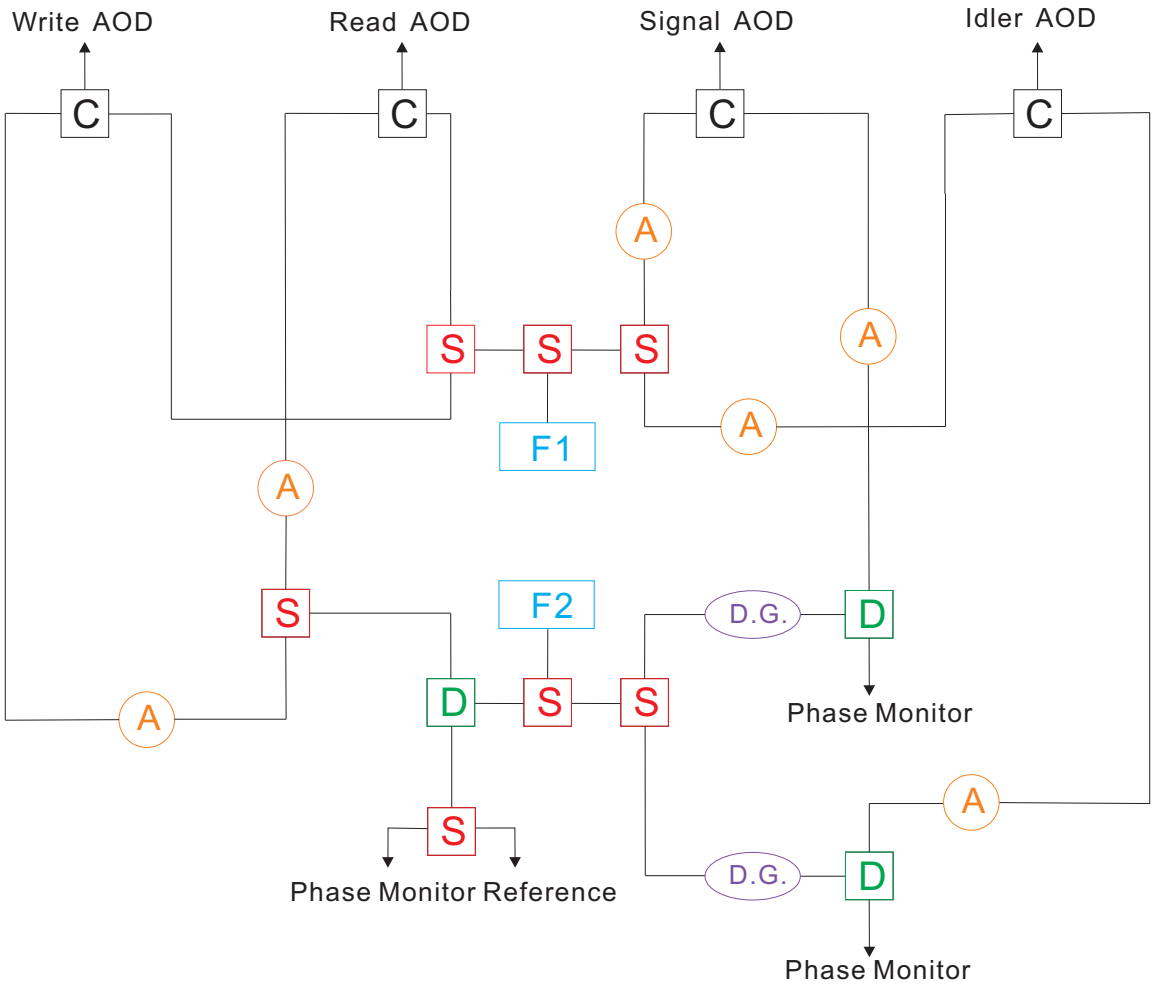

Figure 43: Diagram of the phase shift setup. F1 and F2 are the rf frequencies used to drive the AOD. A is the rf attenuator. S is the rf power splitter. C is the rf power combiner. D is the directional coupler. D.G. the is phase shifter.

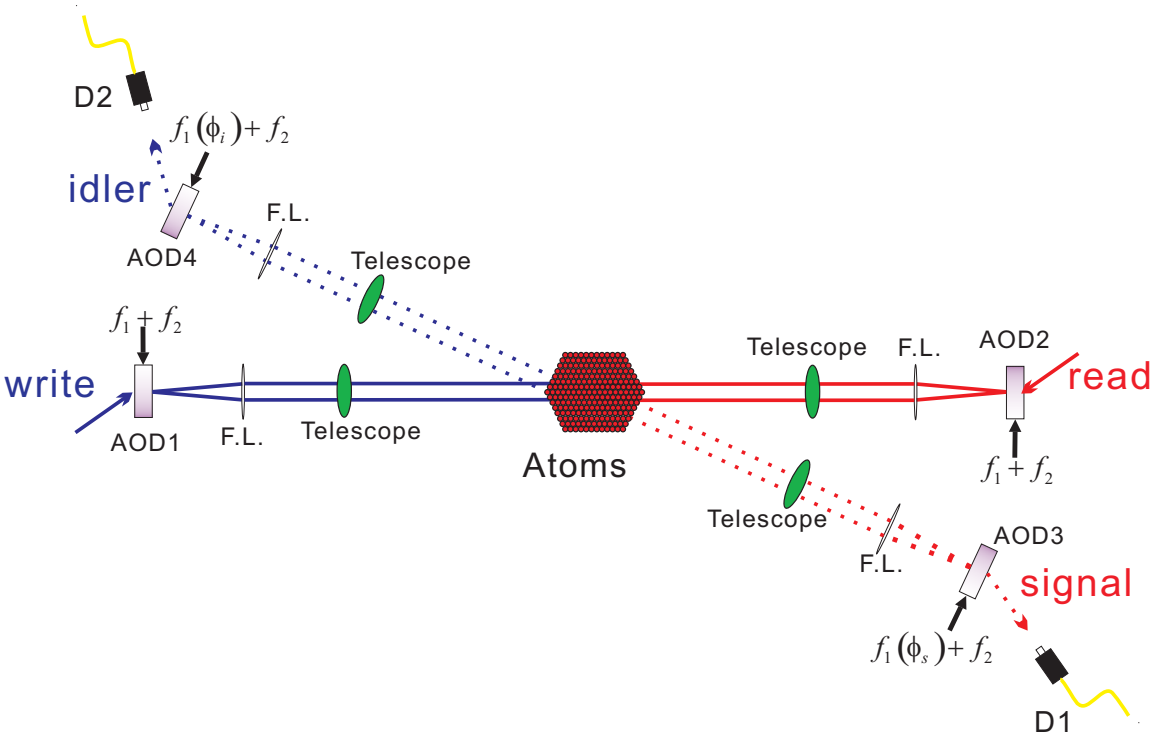

Figure 44: Set-up for entanglement generation using a memory array. The qubit basis is determined by the rf frequencies fed into the AOD. F.L. is Fourier lens; D1 and D2 are single photon detectors. The four AODs share the same two rf sources. The only difference is that there are phase shifters on f_1. ϕ_s is the phase in the signal channel and ϕ_i is the phase in the idler channel. The write/signal AOD diffraction orders are aligned oppositely to shift the signal photons into the same frequency mode. The same principle is also applied to the read/idler AODs.

both 300 ns long, red detuned from the $|5S_{1/2}, F = 3\rangle \rightarrow |5P_{1/2}, F = 3\rangle$ transition by -10 MHz and -10+(f_j-f_k) MHz, respectively, illuminate two different micro-ensembles simultaneously, and generate Raman scattered fields that are collected through the signal AOD and atomic spin waves. The signal AOD is aligned specifically in -1 order with frequencies f_j and f_k so that one of the diffracted signal fields from two different micro-ensembles has the same mode. We select this mode after the AOD and collect it into the optical fiber for detection. Raman scattering produces entanglement between the two-mode signal field (optical qubit) and the spin wave of two elements (matter qubit).

After a 150 ns delay, two read pulses generated from the read AOD aligned in +1 order with frequencies f_j and f_k are sent through these two excited micro-ensembles to map the corresponding spin wave excitations to the idler fields. They both are 250 ns long with 300 μW power. The read pulse for the f_j micro-ensemble is (f_j-f_k)/2 MHz blue detuned on the $|5S_{1/2}, F = 2\rangle \rightarrow |5P_{1/2}, F = 3\rangle$ transition. For the f_k micro-ensemble, the read pulse is (f_j-f_k)/2 MHz red detuned on the $|5S_{1/2}, F = 2\rangle \rightarrow |5P_{1/2}, F = 3\rangle$ transition. The idler fields are detected by placing another AOD in -1 order with frequencies f_j and f_k to collect the identical modes from these two idler fields. We rotate this phase by changing the rf phase on the idler AOD.

$$|\psi_{eff}\rangle \sim |1\rangle_{js}|1\rangle_{ji} + e^{i(\phi_o+\phi_s+\phi_i)}|1\rangle_{ks}|1\rangle_{ki}, \tag{75}$$

where ϕ_s is the phase of f_j on the signal channel, ϕ_i is the phase of f_j on the idler channel, and ϕ_o is the arbitrary definition of the initial phase.

4.3.3 Violation of Bell's Inequality

The rf phase shifters on the signal and idler AODs allows us to vary ϕ_s and ϕ_i. We measure the coincidence of the signal and idler fields as a function of ϕ_s and ϕ_i. Fig. 45 shows the coincidence fringe as a function of ϕ_s for two values of ϕ_i. Since the normalized signal-idler intensity correlation function g is sensitive to the excitation

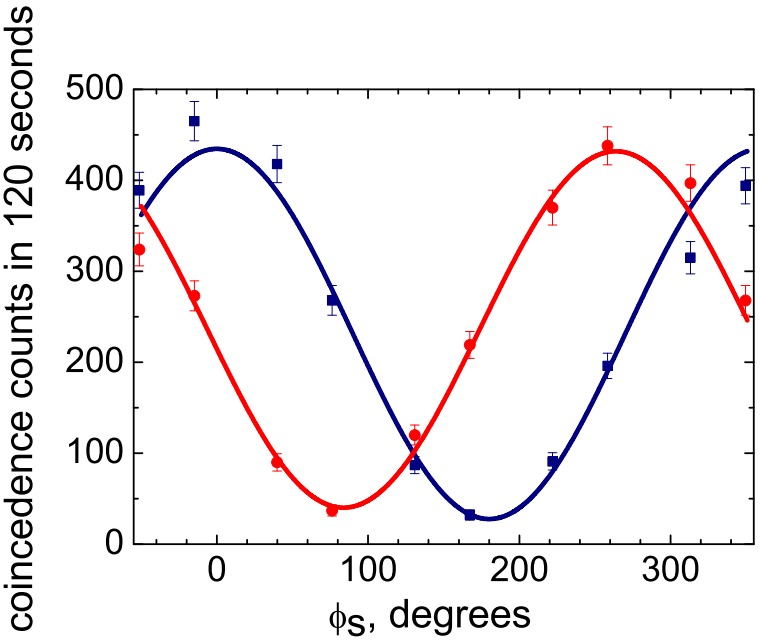

Figure 45: Interference fringe : Measured coincidence of elements of 5 and 8 as function of ϕ_s for ϕ_i=0, squares, and ϕ_i=$\pi/2$, circles.

detuning, the difference of write pulse detuning $f_j - f_k$ for micro-ensemble f_j and f_k causes the non-maximumally entangled state of the system. We compensate by adjusting the write pulse power to balance the signal-idler coincidence rates of micro-ensemble f_j and f_k. The curves are fit with a sinusoidal function, which has 89% visibility. There is no subtraction of the coincidence counts from the background. We follow the Clauser-Horne-Simony-Holt (CHSH) type Bell's inequality violation as discussed in Chapter I and measure the correlation function $E(\phi_s, \phi_i)$, given by

$$E(\phi_s, \phi_i) = \frac{C_{si}(\phi_s, \phi_i) - C_{si}(\phi_s, \phi_i^{\perp}) - C_{si}(\phi_s^{\perp}, \phi_i) + C_{si}(\phi_s^{\perp}, \phi_i^{\perp})}{C_{si}(\phi_s, \phi_i) + C_{si}(\phi_s, \phi_i^{\perp}) + C_{si}(\phi_s^{\perp}, \phi_i) + C_{si}(\phi_s^{\perp}, \phi_i^{\perp})}, \tag{76}$$

where $\phi_{s[i]}^{\perp} = \phi_{s[i]} + \pi$. We then calculate Bell's inequality $|S| \leq 2$ as listed in Table 3, where $S \equiv E(\phi_s, \phi_i) - E(\phi_s, \phi_i') + E(\phi_s', \phi_i) + E(\phi_s', \phi_i')$. We have obtained $S_{exp} = 2.38 \pm 0.03$.

Table 3: Measured correlation function $E(\phi_s, \phi_i)$ and S for ensemble 5 and 8.

ϕ_i	ϕ_s	$E(\phi_s, \phi_i)$
0	$\pi/4$	0.510 ± 0.018
0	$3\pi/4$	-0.683 ± 0.017
$-\pi/2$	$\pi/4$	0.625 ± 0.016
$-\pi/2$	$3\pi/4$	0.562 ± 0.017
		$S_{exp} = 2.38 \pm 0.03$

4.3.4 Interference Fringe of Arbitrary Quantum Elements

With the 1D scanning ability, we are able to create an entangled state of the signal field and collective atomic excitations, where the qubit states are determined by the frequency components f_j and f_k. We select different combinations of elements by changing the rf frequencies into the AODs. The lower fringe visibility for larger micro-ensemble separation is due to the imperfect balance of the signal-idler coincidence rates for the two micro-ensembles. The larger detuning difference requires the write pulse power to be balanced more carefully.

To analyze the effects of the rates imbalance on the interference visibility, we consider the low intensity limit. The normalized signal-idler intensity correlation function of micro-ensemble f can be written as [33]

$$g_{si} = \frac{\langle \Phi | \hat{a}_s^\dagger \hat{a}_i^\dagger \hat{a}_s \hat{a}_i | \Phi \rangle}{\langle \Phi | \hat{a}_s^\dagger \hat{a}_s | \Phi \rangle \langle \Phi | \hat{a}_i^\dagger \hat{a}_i | \Phi \rangle}, \tag{77}$$

where $\hat{a}_s$ and $\hat{a}_i$ are the annihilation operators for the signal and idler fields from micro-ensemble f, respectively. With the quantum state of the signal and idler fields from micro-ensemble f

$$|\Phi\rangle = \sqrt{1-\chi} \sum_{n=0}^{\infty} \chi^{\frac{n}{2}} |n\rangle_s |n\rangle_i, \tag{78}$$

where χ is the intrinsic excitation probability, and $|n\rangle_s |n\rangle_i$ denotes the Fock states of signal and idler fields, we can write g_{si} as a function of intrinsic excitation probability

χ :

$$g_{si} = 1 + \frac{1}{\chi}. \tag{79}$$

Now, considering the signal and idler fields from two micro-ensembles, j and k, interfering on the AODs with the same efficiency, we define the creation operator of signal and idler fields after the AOD in the following way:

$$\hat{a}^{\dagger}_{s+} \equiv \frac{1}{\sqrt{2}}(\hat{a}^{\dagger}_{js} + e^{-\phi_s}\hat{a}^{\dagger}_{ks}) \quad \text{and} \quad \hat{a}^{\dagger}_{i+} \equiv \frac{1}{\sqrt{2}}(\hat{a}^{\dagger}_{ji} + e^{-\phi_i}\hat{a}^{\dagger}_{ki}). \tag{80}$$

The coincidence detection rate of the signal-idler fields

$$\begin{aligned} C &\propto \langle\Psi|\hat{a}^{\dagger}_{s+}\hat{a}^{\dagger}_{i+}\hat{a}_{s+}\hat{a}_{i+}|\Psi\rangle \\ &= \frac{1}{4}\frac{\chi_j + \chi_j^2}{(1-\chi_j)^2} + \frac{1}{4}\frac{\chi_k + \chi_k^2}{(1-\chi_k)^2} + \frac{1}{2}\frac{\chi_j}{1-\chi_j}\frac{\chi_k}{1-\chi_k} \\ &+ \frac{1}{2}\frac{\sqrt{\chi_j}}{1-\chi_j}\frac{\sqrt{\chi_k}}{1-\chi_k}\cos(\phi_s + \phi_i), \end{aligned} \tag{81}$$

where $|\Psi\rangle = |\Phi\rangle_j|\Phi\rangle_k$. The visibility V of the interference fringe as a function of $g^{(j)}_{si}$ and $g^{(k)}_{si}$ without accounting for any background is

$$V \equiv \frac{c_{max} - c_{min}}{c_{max} + c_{min}} = \frac{\sqrt{(g^{(j)}_{si} - 1)(g^{(k)}_{si} - 1)}}{1 + \frac{g^{(j)}_{si}(g^{(k)}_{si} - 2)}{2(g^{(j)}_{si} - 2)} + \frac{g^{(k)}_{si}(g^{(j)}_{si} - 2)}{2(g^{(k)}_{si} - 2)}}. \tag{82}$$

The visibility is a function of $g^{(j)}_{si}$ and $g^{(k)}_{si}$. The imbalance of g_{si} will decrease the visibility. Table 4 and Fig. 46 show the fringe and visibility for different combinations of elements. The expected value of V, when $g^{(j)}_{si} = g^{(k)}_{si} = g^{max}_{si}$, is denoted by V^{max}_{bal}, where g^{max}_{si} is the measured correlation function of the maximum data point. The measured visibilities that are lower than their expected values can likely be attributed to the imbalance of $g^{(j)}_{si}$ and $g^{(k)}_{si}$.

4.4 Conclusion

We have demonstrated a multiplexed array of 12 independent addressable quantum memory elements. Such multiplexed memory elements are essential components for

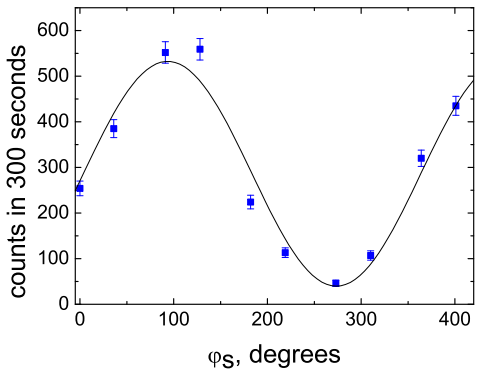

(a)

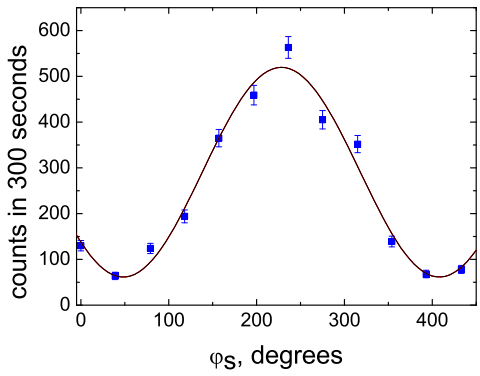

(b)

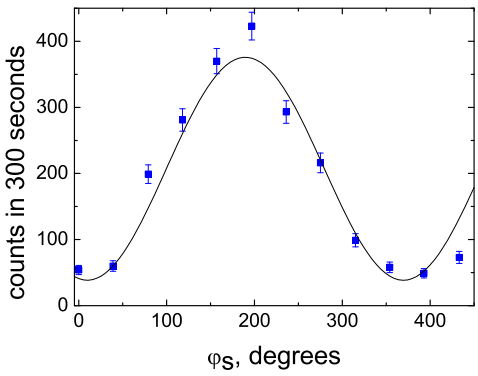

(c)

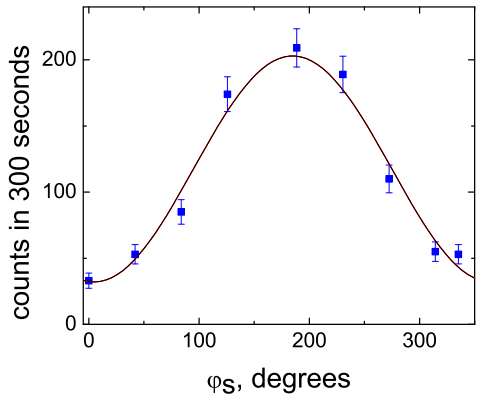

(d)

Figure 46: Measured coincident counts as function of ϕ_s with different combinations of memory elements. (a) is 7 and 8, (b) is 7 and 10, (c) is 5 and 10, and (d) is 1 and 12.

Table 4: Measured interference visibility V_{exp} for different combinations of memory elements.

j	k	V_{exp}	V_{bal}^{max}	g_{si}^{max}
5	8	$88 \pm 1\%$	88.9%	17
7	8	$86 \pm 2\%$	91.7%	23
7	10	$79 \pm 1\%$	90.5%	20
5	10	$81 \pm 2\%$	88.9%	17
1	12	$73 \pm 3\%$	88.2%	16

long-distance quantum entanglement distribution. One can increase the number of addressable elements by multiplexing in both transverse dimensions. Such memory arrays enable local entanglement generation [82, 83], which combined with cascade emission in the same atomic cloud, can produce quantum memory elements compatible with existing low-loss telecommunication channels [36]. Quantum repeaters using such arrays offer communication rates several orders of magnitude faster than those achievable through equivalent parallel systems.

CHAPTER V

QUANTUM INTERFERENCE OF ELECTROMAGNETIC FIELDS FROM REMOTE QUANTUM MEMORIES

Part of this chapter is based on Ref. [84].

Proposed approaches to scalable quantum information networks and distributed quantum computing involve linear optical elements and single-photon detectors [26, 36, 85]. Photoelectric detection events signal entanglement creation and, by postselection, eliminate undesirable components of the electromagnetic field. While postselection has a residual negative effect on the scaling of the overall efficiency of quantum information protocols, this can be offset by quantum memory, a resource which provides the capability to perform quantum state transfer from matter to light and vice versa, as demonstrated with cold atomic ensembles [28, 30, 35]. These also act as sources of entangled photon pairs, with quantum memory enabling user-controlled delays between the photons.

In order to distribute entanglement over a network configuration we must connect entangled elements at remote sites. This may be achieved by interfering photons, produced at these sites, on a beam splitter followed by coincident photoelectric detection. The anticorrelation of coincidence counts is the signature of Hong-Ou-Mandel interference (HOM), whereby single photons are simultaneously incident at two input ports of a beam splitter both exit in one or other of the output ports [86, 87]. For distinct, remote quantum memory elements, HOM is a possible method for entanglement connection operations that scale efficiently with the number of elements. Several remarkable demonstrations of HOM using parametric down-conversion (PDC) have been reported (see Refs. [87, 88, 89] and references therein). It has also been observed

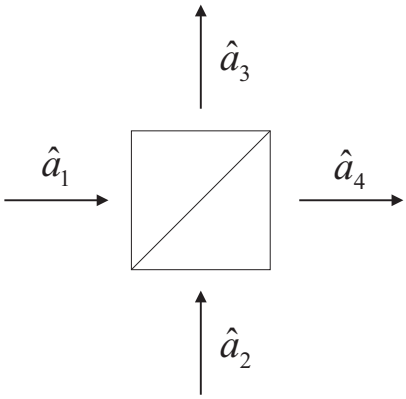

Figure 47: Representation of a lossless beam splitter showing the notation for the annihilation operators associated with the input and output fields.

using photon pairs generated locally by a single source - a quantum dot [90], an atom [91], and an atomic ensemble [38]. Moreover HOM has been demonstrated with two (a) neutral atoms [92] and (b) ions [93], in each case separated by a few microns.

In this chapter, I first describe the HOM interference using a model of 50/50 beam splitter with two single photon states on the two input port separately in Heisenberg picture. This will give a flavor of the two photon interference effect. Then I present the experiment of the quantum interference of the remote and distinct photon sources. These photon sources are generated from two cold atomic ensembles with quantum memory. We investigate the indistinguishability of these photons.

5.1 Two Photon Interference

Single photons with well-defined coherence properties have now been widely investigated because of their fundamental role in many applications in quantum information science. The first demonstration of this two photon interference was carried out by Hong, Ou, and Mandel. They employed the signal and idler photons from a parametric down-conversion source on a 50/50 beam splitter. It was designed to measure the time separation of the two photons. By varying the time delay between these two photons, they measured the coincidence rate of photodetections at the two output ports of the beam splitter. As a function of delay, the coincidence rate shows a minimum

when the photons impinge simultaneously on the beam splitter, and for otherwise identical photons, the width of this dip is the photon duration. The minimum in the coincidence rate goes to zero if the photons are identical.

Consider a symmetric beam splitter (Fig. 47) for monochromatic incidence fields with the reflection coefficient $\mathbf{r} = |\mathbf{r}| \exp(i\phi_{\mathbf{r}})$ and the transmission coefficient $\mathbf{t} = |\mathbf{t}| \exp(i\phi_{\mathbf{t}})$ that satisfies the relation

$$|\mathbf{r}|^2 + |\mathbf{t}|^2 = 1 \quad \text{and} \quad \mathbf{r}\mathbf{t}^* + \mathbf{t}\mathbf{r}^* = 0. \tag{83}$$

The relation between the input and output modes of the beam splitter is

$$\hat{a}_3 = \mathbf{r}\hat{a}_1 + \mathbf{t}\hat{a}_2 \quad \text{and} \quad \hat{a}_4 = \mathbf{t}\hat{a}_1 + \mathbf{r}\hat{a}_2, \tag{84}$$

$$\hat{a}_1^\dagger = \mathbf{r}\hat{a}_3^\dagger + \mathbf{t}\hat{a}_4^\dagger \quad \text{and} \quad \hat{a}_2^\dagger = \mathbf{t}\hat{a}_3^\dagger + \mathbf{r}\hat{a}_4^\dagger. \tag{85}$$

We assume that the input fields in arms 1 and 2 are independent, with creation operators that satisfy the boson commutation relations

$$[\hat{a}_1, \hat{a}_1^\dagger] = [\hat{a}_2, \hat{a}_2^\dagger] = 1 \quad \text{and} \quad [\hat{a}_1, \hat{a}_2^\dagger] = [\hat{a}_2, \hat{a}_1^\dagger] = 0. \tag{86}$$

From equations (83) and (85),

$$[\hat{a}_3, \hat{a}_3^\dagger] = [\mathbf{r}\hat{a}_1 + \mathbf{t}\hat{a}_2, \mathbf{r}^*\hat{a}_1^\dagger + \mathbf{t}^*\hat{a}_2^\dagger] = |\mathbf{r}|^2 + |\mathbf{t}|^2 = 1, \tag{87}$$

$$[\hat{a}_3, \hat{a}_4^\dagger] = [\mathbf{r}\hat{a}_1 + \mathbf{t}\hat{a}_2, \mathbf{t}^*\hat{a}_1^\dagger + \mathbf{r}^*\hat{a}_2^\dagger] = \mathbf{r}\mathbf{t}^* + \mathbf{t}\mathbf{r}^* = 0, \tag{88}$$

and similarly,

$$[\hat{a}_4, \hat{a}_4^\dagger] = 1. \tag{89}$$

Let's prepare the input state with one horizontally polarized photon incident on each input port as the indices represent below:

$$|\phi_{in}\rangle_{HH} = \hat{a}_{1H}^\dagger \hat{a}_{2H}^\dagger |0\rangle = |1\rangle_{1H}|1\rangle_{2H}. \tag{90}$$

We can write down the output state in the following way:

$$\begin{aligned} \hat{a}_{1H}^\dagger \hat{a}_{2H}^\dagger |0\rangle &= (\mathbf{r}\hat{a}_{3H}^\dagger + \mathbf{t}\hat{a}_{4H}^\dagger)(\mathbf{t}\hat{a}_{3H}^\dagger + \mathbf{r}\hat{a}_{4H}^\dagger)|0\rangle \\ &= [\mathbf{r}\mathbf{t}(\hat{a}_{3H}^\dagger)^2 + \mathbf{r}\mathbf{r}\hat{a}_{3H}^\dagger \hat{a}_{4H}^\dagger + \mathbf{t}\mathbf{t}\hat{a}_{3H}^\dagger \hat{a}_{4H}^\dagger + \mathbf{r}\mathbf{t}(\hat{a}_{4H}^\dagger)^2]|0\rangle]. \end{aligned} \tag{91}$$

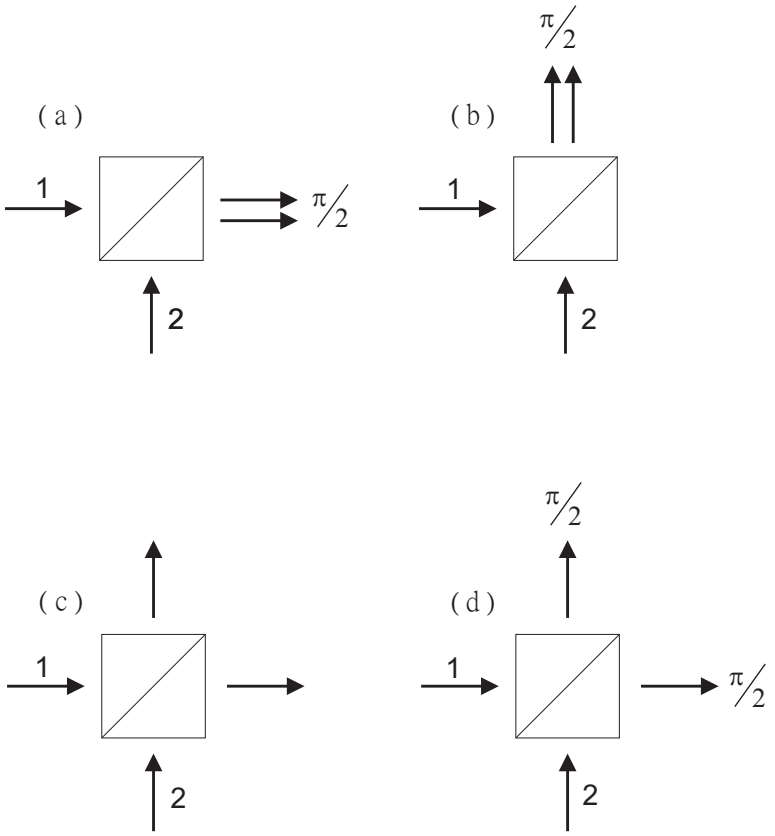

Figure 48: Two impinging photons lead to four possible photon distributions at the beam-splitter output. In (a) and (b), the photons would be found together. In (c) and (d), the photons would leave the beam splitter through different ports. Since the quantum states of (d) pick up π phase with respect to the quantum state (c), they interfere destructively.

For a 50/50 beam splitter,

$$|\mathbf{r}|^2 = |\mathbf{t}|^2 = \frac{1}{2} \quad \text{with} \quad \phi_{\mathbf{r}} - \phi_{\mathbf{t}} = \frac{\pi}{2}, \tag{92}$$

so Eq. (91) can be extended:

$$\begin{aligned} &\hat{a}^\dagger_{1H}\hat{a}^\dagger_{2H}|0\rangle \\ &= \exp(2i\phi_{\mathbf{t}})[i\frac{1}{2}(\hat{a}^\dagger_{3H})^2 + \frac{1}{2}\hat{a}^\dagger_{3H}\hat{a}^\dagger_{4H} - \frac{1}{2}\hat{a}^\dagger_{3H}\hat{a}^\dagger_{4H} + i\frac{1}{2}(\hat{a}^\dagger_{4H})^2]|0\rangle. \end{aligned} \tag{93}$$

According to Eq. (93), there are four possibilities for photons leaving the beam splitter. The first and the last terms in the summing brackets represent photons leaving

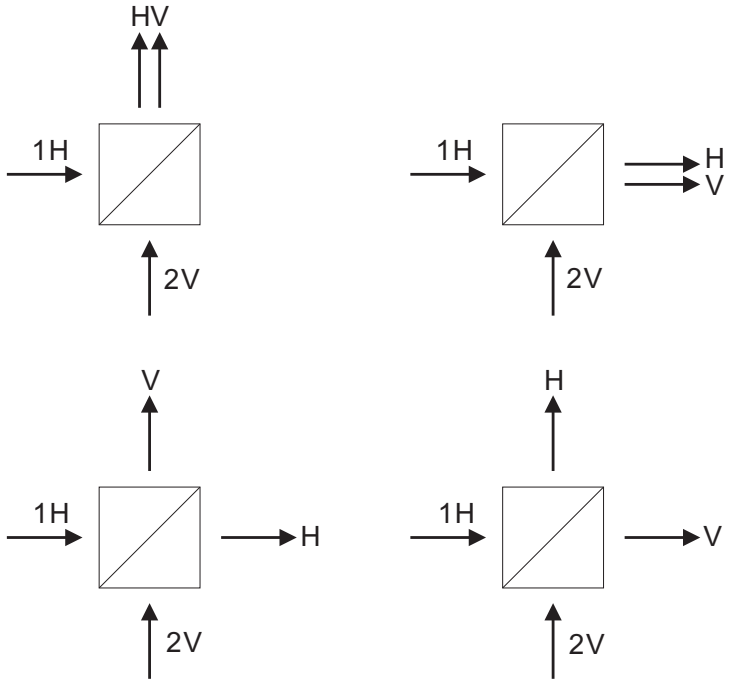

Figure 49: Two photon interference with two different polarizations at different ports. There are four distinct possibilities distinguished by their polarization.

the beam splitter through the same port, while the second and third terms represent photons leaving through different ports. These two terms are indistinguishable and have opposite sign in the expression; therefore, these two possibilities interfere destructively as shown in Fig. 48. As a consequence, the two photons always leave the beam splitter as a pair and the output state is given by the superposition

$$|\phi_{out}\rangle_{HH} = \exp(2i\phi_{\mathbf{t}})\frac{i}{\sqrt{2}}(|2\rangle_{3H}|0\rangle_{4H} + |0\rangle_{3H}|2\rangle_{4H}). \tag{94}$$

On the other hand, if we prepare two photons in orthogonal polarization, the output state will be

$$|\phi_{in}\rangle_{HV} = (\mathbf{r}\hat{a}^{\dagger}_{3H} + \mathbf{t}\hat{a}^{\dagger}_{4H})(\mathbf{t}\hat{a}^{\dagger}_{3V} + \mathbf{r}\hat{a}^{\dagger}_{4V})|0\rangle. \tag{95}$$

There are four possibilities distinguished by their polarization. These four cases are

illustrated in Fig. 49. The output state becomes

$$\begin{aligned} & |\phi_{out}\rangle_{HV} \\ = \; & \exp(2i\phi_{\mathbf{t}})\frac{1}{\sqrt{2}}(i|1\rangle_{3H}|0\rangle_4 - |0\rangle_3|1\rangle_{4H}) \\ \otimes \; & (|1\rangle_{3V}|0\rangle_4 + i|0\rangle_3|1\rangle_{4V}). \end{aligned} \tag{96}$$

5.2 Remote Independent Photon Sources

The photon sources are two cold atomic ensembles with quantum memory, located in adjacent laboratories and separated by 5.5 m (Fig. 50). Here, we use magneto-optical traps (MOTs) of ^{85}Rb to provide optically thick atomic ensembles at sites A and B (Fig. 50). The ground levels $\{|a\rangle; |b\rangle\}$ correspond to the $5S_{1/2}, F = \{3, 2\}$ levels of ^{85}Rb, and the excited level $|c\rangle$ represents the $\{5P_{1/2}, F = 3\}$ level of the D_1 line at 795 nm. In a particular ensemble signal photons are generated by Raman scattering of a write laser pulse with temporal profile $\varphi(t)$ (normalized to unity $\int dt \;\; |\varphi(t)|^2 = 1$), whose length is much greater than the ensemble dimensions. For an unpolarized ensemble of N atoms interacting with an off-resonant vertically ($\mathbf{e}_V = -\hat{\mathbf{z}}$) polarized write field propagating in the y-direction, the unitary operator $\hat{U}$ for the system can be described by [33]

$$\hat{U} = \exp(\chi \cos\eta \; \hat{a}^{\dagger}_{s,H}\hat{s}^{\dagger}_{H} + \chi \sin\eta \; \hat{a}^{\dagger}_{s,V}\hat{s}^{\dagger}_{V} - H.c.), \tag{97}$$

where $\hat{a}_{s,\lambda}$, $\lambda = H, V$ is the discrete signal mode bosonic operator and the emission of $H-$ or V- polarized signal photons creates correlated atomic spin wave excitations with annihilation operators $\hat{s}_{H,V}$. η is the parametric mixing angle and χ is the dimensionless parametric coupling constant [30, 59]. Since $\hat{a}_{\lambda}$ commutes with the Rayleigh scattering and undetected Raman scattering Hamiltonians, with the operator expansion theorem

$$e^{\hat{A}}\hat{B}e^{-\hat{A}} = \hat{B} + [\hat{A}, \hat{B}] + \frac{1}{2!}[\hat{A}, [\hat{A}, \hat{B}]] + ... \tag{98}$$

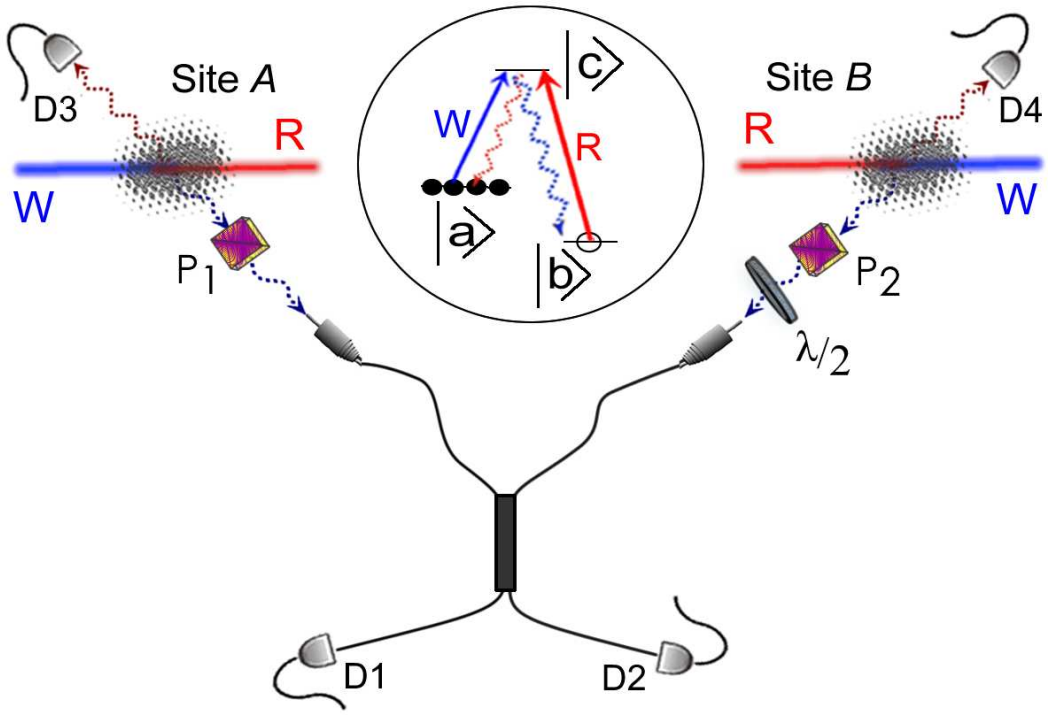

Figure 50: Schematic showing Raman scattering of write pulses (W) at sites A and B with signal fields collected by polarizers P_1 and P_2 and optical fiber beam splitter and directed towards detectors D1, D2. A half-wave plate ($\lambda/2$) may be inserted at site B to rotate light polarization. Raman scattering of delayed read pulses produces idler fields detected at D3, D4. The inset shows the atomic level structure and the write- and read-induced Raman processes.

the Heisenberg picture solutions can be written as

$$\begin{aligned}
\hat{a}_{s,H}^{(out)} &= \hat{U}^{\dagger}\hat{a}_{s,H}^{(in)}\hat{U} \\
&= \hat{a}_{s,H}^{(in)} + [\chi\cos\eta\ \hat{a}_{s,H}^{\dagger}\hat{s}_{H}^{\dagger} + \chi\sin\eta\ \hat{a}_{s,V}^{\dagger}\hat{s}_{V}^{\dagger} - H.c., \hat{a}_{s,H}^{(in)}] \\
&\quad + \frac{1}{2!}[\chi\cos\eta\ \hat{a}_{s,H}^{\dagger}\hat{s}_{H}^{\dagger} + \chi\sin\eta\ \hat{a}_{s,V}^{\dagger}\hat{s}_{V}^{\dagger} - H.c., [\chi\cos\eta\ \hat{a}_{s,H}^{\dagger}\hat{s}_{H}^{\dagger} \\
&\quad + \chi\sin\eta\ \hat{a}_{s,V}^{\dagger}\hat{s}_{V}^{\dagger} - H.c., \hat{a}_{s,H}^{(in)}]] + ... \\
&= \hat{a}_{s,H}^{(in)} - \chi\cos\eta\hat{s}_{H}^{(in)\dagger} + \frac{1}{2!}|\chi\cos\eta|^2\hat{a}_{s,H}^{(in)} - \frac{1}{3!}|\chi\cos\eta|^3\hat{s}_{H}^{(in)\dagger} + ... \\
&= \cosh(\chi\cos\eta)\ \hat{a}_{s,H}^{(in)} - \sinh(\chi\cos\eta)\,\hat{s}_{H}^{(in)\dagger}, \qquad (99)
\end{aligned}$$

$$\begin{aligned}
\hat{a}_{s,V}^{(out)} &= \hat{U}^{\dagger}\hat{a}_{s,V}^{(in)}\hat{U} \\
&= \cosh(\chi\sin\eta)\ \hat{a}_{s,V}^{(in)} - \sinh(\chi\sin\eta)\,\hat{s}_{V}^{(in)\dagger}, \qquad (100)
\end{aligned}$$

$$\begin{aligned}
\hat{s}_{H}^{(out)} &= \hat{U}^{\dagger}\hat{s}_{H}^{(in)}\hat{U} \\
&= \cosh(\chi\cos\eta)\ \hat{s}_{H}^{(in)} - \sinh(\chi\cos\eta)\,\hat{a}_{s,H}^{(in)\dagger}, \qquad (101)
\end{aligned}$$

$$\begin{aligned}
\hat{s}_{V}^{(out)} &= \hat{U}^{\dagger}\hat{s}_{V}^{(in)}\hat{U} \\
&= \cosh(\chi\sin\eta)\ \hat{s}_{V}^{(in)} - \sinh(\chi\sin\eta)\,\hat{a}_{s,V}^{(in)\dagger}. \qquad (102)
\end{aligned}$$

These solutions allow calculation of the photoelectric detection signal for an atomic quantum memory element. The signal field detected from ensemble A, generated by the write pulse with temporal mode $\varphi_A(t - z_A/c)$ and spatial mode φ_A is given by

$$\hat{E}_{s,\lambda,A}^{(+)} = \tilde{A}(k_s, t, z_A)\phi_{s,A}(\mathbf{r})\,\varphi_A\left(t - \frac{z_A}{c}\right)\hat{a}_{s,\lambda,A}^{(out)}, \qquad (103)$$

where z_A is the position coordinate and $\tilde{A}$ is a complex number depending on k_s, t, and z_A [33]. A similar expression is also valid for ensemble B.

In order to generate indistinguishable signal wavepackets from the two atomic memories, we produce their respective *write* fields by splitting a single pulse and directing the outputs into identical 100 m long optical fibers. For a linearly polarized

write field we observe that the signal field is nearly orthogonally polarized. The two Raman-scattered signal fields produced at A and B are passed through polarizing cubes to select the H-components and coupled into the ends of a fiber-based beam splitter. The outputs of the latter are connected to single-photon counting modules D1 and D2. A half-wave plate is inserted into the path of signal field B (Fig. 50) which allows us to vary the relative (linear) polarization of the detected fields. This allows us to detect parallel polarizations ($||$), which exhibit the HOM effect, and orthogonal polarizations ($\perp$), which do not.

5.3 Experiment

5.3.1 Interference of Two Thermal Fields

The fields from A and B are combined on a beam splitter $R + T = 1$ satisfy the following relations

$$\hat{E}_{s,1} = \mathbf{r}\hat{E}_{s,\lambda,A} + \mathbf{t}\hat{E}_{s,\lambda,B} \tag{104}$$

$$\hat{E}_{s,2} = \mathbf{t}\hat{E}_{s,\lambda,A} + \mathbf{r}\hat{E}_{s,\lambda,B}, \tag{105}$$

where $|\mathbf{r}|^2 = R$ and $|\mathbf{t}|^2 = T$ are its reflectance and transmittance, and the fields $\hat{E}_{s,1}$, $\hat{E}_{s,2}$ in the output ports 1 and 2 are incident on detectors D1 and D2, respectively.

We employ vertically (V) polarized write beams, derived from the same laser, and detect the horizontally (H) polarized signal fields, which are passed through polarizing cubes prior to the beam splitter. The corresponding cross-correlation function

$$G^{(12)}_{\|(\perp)}(t, t+\tau) \equiv \langle \hat{E}^{-}_{s,1}(t)\hat{E}^{-}_{s,2}(t+\tau)\hat{E}^{+}_{s,2}(t+\tau)\hat{E}^{+}_{s,1}(t)\rangle \tag{106}$$

exhibits the HOM effect:

$$\begin{aligned} & G^{(12)}_{\|}(t, t+\tau) = \\ & \mathcal{E}_A^2\mathcal{E}_B^2|T\varphi_A(t+\tau)\varphi_B(t) - R\varphi_B(t+\tau)\varphi_A(t)|^2 s_A^2 s_B^2 \\ + \quad & 2RT\left(\mathcal{E}_A^4|\varphi_A(t+\tau)\varphi_A(t)|^2 s_A^4 + \mathcal{E}_B^4|\varphi_B(t+\tau)\varphi_B(t)|^2 s_B^4,\right) \end{aligned} \tag{107}$$

where

$$s_{A[B]} \equiv \sinh(\chi_{A[B]} \cos\eta), \quad \text{and} \quad \mathcal{E}_{A[B]} = |\tilde{A}||\phi_{s,A[B]}(\mathbf{r})|. \tag{108}$$

The first, HOM, term on the right-hand side of Eq. (107) exhibits two photon interference and can be understood in terms of conventional single-photon interference conditioned on the first photoelectric detection at time t [91]. For zero delay $\tau = 0$ and a symmetric beam splitter $R = T = 1/2$, this term gives zero contribution even for $\varphi_A \neq \varphi_B$. Alternatively, for $\varphi_A = \varphi_B$ it vanishes for arbitrary τ. However, $G_{\parallel}^{(12)}(t, t+\tau)$ does not vanish completely due to contributions from multiphoton signal excitations (second term in Eq. (107)). To quantify the degree of the HOM effect, the following benchmark measurement is performed. We insert a half-wave plate into the path of the signal field from ensemble B, rotating its polarization from H to V, thus nullifying the HOM effect. Quantitatively, in this case the corresponding correlation function $G_{\perp}^{(12)}(t, t+\tau)$ is given by

$$\begin{aligned} & G_{\perp}^{(12)}(t, t+\tau) = \\ & \mathcal{E}_A^2 \mathcal{E}_B^2 |T\varphi_A(t+\tau)\varphi_B(t)|^2 + |R\varphi_B(t+\tau)\varphi_A(t)|^2 s_A^2 s_B^2 \\ + \quad & 2RT\left(\mathcal{E}_A^4 |\varphi_A(t+\tau)\varphi_A(t)|^2 s_A^4 + \mathcal{E}_B^4 |\varphi_B(t+\tau)\varphi_B(t)|^2 s_B^4\right) \end{aligned} \tag{109}$$

Particular care is taken to eliminate possible sources of spectral broadening. Magnetic trapping fields are switched off after atomic collection and cooling, and the residual ambient field is compensated by sets of Helmholtz coils. All trapping and cooling light fields are switched off during data acquisition. The trapping light is shut off about 10 μs before the repumping light, preparing unpolarized atoms in level $|a\rangle$.

In Fig. 51 we show the measured ratio of the photoelectric coincidence rates $\mathcal{R}_{\parallel}/\mathcal{R}_{\perp}$, which are integrated over the duration of the write pulses. Our measurements exclude Rayleigh scattering on the *write* transition by means of frequency filtering. The experimental ratio $\mathcal{R}_{\parallel}/\mathcal{R}_{\perp}$ is compared to the ratio of integrated correlation functions $\int\int dt d\tau G_{\parallel}^{(12)}(t, t+\tau)$ and $\int\int dt d\tau G_{\perp}^{(12)}(t, t+\tau)$, assuming identical

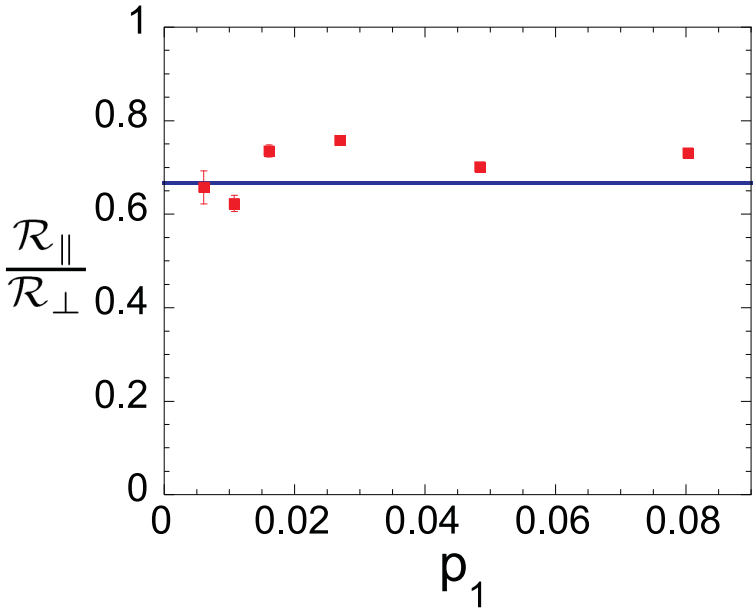

Figure 51: Ratio of measured two-fold coincidence rates for the $\perp$ and $\parallel$ configurations. The parameter $p_1 \equiv (N_1 + N_2)/N_T$ (averaged over the $\perp$ and $\parallel$ cases). Here $N_1(N_2)$ is the number of photoelectric detections in detector $D1(D2)$, N_T is the number of experimental trials. Theoretically it can be expressed as $p_1 = \epsilon_A s_A^2 + \epsilon_B s_B^2$, where $\epsilon_A(\epsilon_B) \approx 0.05 - 0.07$ is the overall probability to detect a signal photon from site A (site B) by either D1 or D2. Scatter beyond the estimated Poissonian level of uncertainty is consistent with systematic drifts in experimental conditions, in particular the single count rates from each ensemble. The solid line is our theoretical prediction based on Eq. (107), for $R = T = 1/2$ and $\epsilon_A s_A^2 = \epsilon_B s_B^2$.

wavepackets $\varphi_A = \varphi_B$. We observe scatter in the data beyond the deviations due to photoelectron counting statistics. These indicate the level of systematic drifts encountered over several hours of data acquisition.

The photoelectric coincidences arise from the signal field excitation pairs produced (I) one excitation from each ensemble; (II) both excitations from ensemble A; (III) both excitations from ensemble B. The HOM visibility of $V \equiv 1 - \mathcal{R}_\parallel/\mathcal{R}_\perp = 1/3$ reflects the deleterious effects of contributions (II) and (III). These are relatively large because in the limit of weak excitation the spin wave-signal state is dominated by the vacuum contribution. By detecting the presence of a spin wave atomic excitation in each ensemble, these contributions could be substantially suppressed, and the HOM

visibility $V \to 1$ in the limit that the excitation probability $p_1 \to 0$.

5.3.2 Interference of Single Photons

We obtain high-visibility HOM fringes by means of a four-photon delayed coincidence detection procedure. This involves conversion of the spin wave excitation to an idler field by means of an incident read laser pulse which follows the write pulse by a programmable time delay δt in the off-axis geometry [29]; δt is limited by the quantum memory coherence time τ_c [31]. By careful minimization of ambient magnetic fields, $\tau_c > 30$ μs have been reported [37]. In this work we choose $\delta t = 100$ ns in order to maximize the repetition rate of the protocol. The atomic spin wave operators are thus transferred into the detected idler filed modes

$$\begin{aligned} \hat{a}_{i,H}^{(out)} &= \hat{U}^\dagger \hat{a}_{i,H}^{(in)} \hat{U} \\ &= \cosh(\chi \cos\eta)\ \hat{a}_{i,H}^{(in)} - \sinh(\chi \cos\eta)\, \hat{a}_{s,H}^{(in)\dagger}, \end{aligned} \tag{110}$$

$$\begin{aligned} \hat{a}_{i,V}^{(out)} &= \hat{U}^\dagger \hat{a}_{i,V}^{(in)} \hat{U} \\ &= \cosh(\chi \sin\eta)\ \hat{a}_{i,V}^{(in)} - \sinh(\chi \sin\eta)\, \hat{a}_{s,V}^{(in)\dagger}, \end{aligned} \tag{111}$$

$$\begin{aligned} \hat{a}_{s,H}^{(out)} &= \hat{U}^\dagger \hat{a}_{s,H}^{(in)} \hat{U} \\ &= \cosh(\chi \cos\eta)\ \hat{a}_{s,H}^{(in)} - \sinh(\chi \cos\eta)\, \hat{a}_{i,H}^{(in)\dagger}, \end{aligned} \tag{112}$$

$$\begin{aligned} \hat{a}_{s,V}^{(out)} &= \hat{U}^\dagger \hat{a}_{s,V}^{(in)} \hat{U} \\ &= \cosh(\chi \sin\eta)\ \hat{a}_{s,V}^{(in)} - \sinh(\chi \sin\eta)\, \hat{a}_{i,V}^{(in)\dagger}. \end{aligned} \tag{113}$$

The idler field detected from ensemble A, retrieved by the read pulse with temporal mode $\varphi_A(t - z_A/c)$ and spatial mode φ_A is given by

$$\hat{E}_{i,\lambda,A}^{(+)} = \sqrt{\frac{\hbar k_i}{2\epsilon_0}} e^{-ick_i\left(t - \frac{z_A}{c}\right)} \phi_{i,A}(\mathbf{r})\, \varphi_A\left(t - \frac{z_A}{c}\right) \hat{a}_{i,\lambda,A}^{(out)}, \tag{114}$$

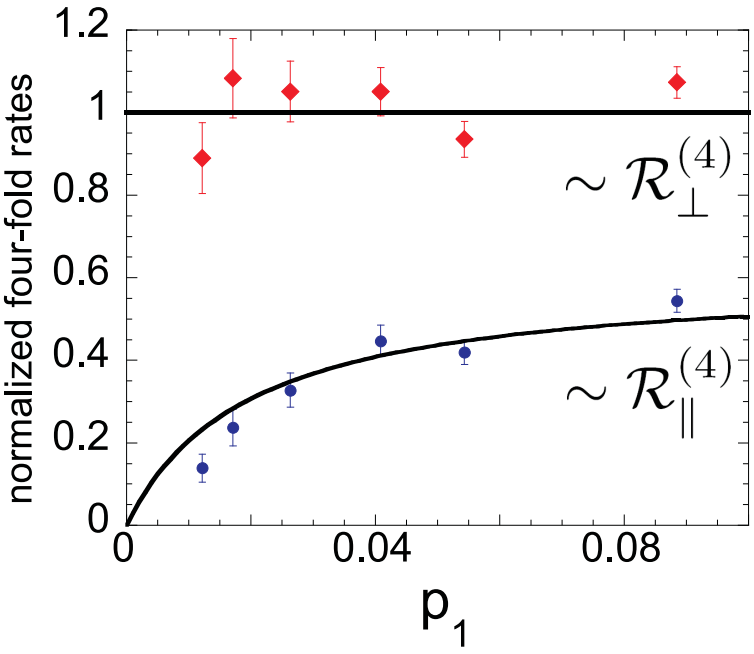

Figure 52: Integrated four-fold coincidence rates $\mathcal{R}_{\parallel}^{(4)}/\mathcal{W}_{\perp}^{(4)}$ and $\mathcal{R}_{\perp}^{(4)}/\mathcal{W}_{\perp}^{(4)}$ as a function of p_1. Experiment, dots, theory, solid line, assuming identical signal mode wavepackets from each ensemble. Uncertainties are based on the statistics of the photon counting events.

where z_A is the position coordinate and $\tilde{A}$ is a complex number depending on k_i, t, and z_A [33]. A similar expression is also valid for ensemble B.

The four-fold detection of the two idler and two signal fields involves HOM of the two signal fields and delayed coincidence detection of the idler fields at detectors D3 and D4, as shown in Fig. 50.

The four-fold coincidence rate is thus given by

$$\begin{aligned}\mathcal{R}_{\parallel}^{(4)} &\propto \langle \hat{E}_{i,B}^{-}(t)\hat{E}_{i,A}^{-}(t+\tau)\hat{E}_{s,1}^{-}(t)\hat{E}_{s,2}^{-}(t+\tau)\hat{E}_{s,2}^{+}(t+\tau)\hat{E}_{s,1}^{+}(t)\hat{E}_{i,A}^{+}(t+\tau)\hat{E}_{i,B}^{+}(t)\rangle \\ &\propto s_A^2 s_B^2 \left\{(R-T)^2(1+2s_A^2)(1+2s_B^2)\right. \\ &\quad \left. + 2RT\left(3s_A^4+3s_B^4+2s_A^2+2s_B^2\right)\right\}. \end{aligned} \tag{115}$$

We have again assumed identical wavepacket modes for both ensembles.

By inserting a half-wave plate into the path of the signal field from ensemble B as before (rotating polarization from H to V), we suppress the HOM interference

contributions, such that the four-fold coincidence rate becomes

$$\begin{aligned}\mathcal{R}_{\perp}^{(4)} &\propto \langle \hat{E}_{i,B}^{-}(t)\hat{E}_{i,A}^{-}(t+\tau)\hat{E}_{s,1}^{-}(t)\hat{E}_{s,2}^{-}(t+\tau)\hat{E}_{s,2}^{+}(t+\tau)\hat{E}_{s,1}^{+}(t)\hat{E}_{i,A}^{+}(t+\tau)\hat{E}_{i,B}^{+}(t)\rangle \\ &\propto s_A^2 s_B^2 \left\{(R^2+T^2)(1+2s_A^2)(1+2s_B^2)\right. \\ &\quad \left. + 2RT\left(3s_A^4+3s_B^4+2s_A^2+2s_B^2\right)\right\}. \end{aligned} \tag{116}$$

In separate sets of measurements we recorded photoelectric events with one, or other, of the two MOTs blocked, which allow us to determine the expected level of four-fold coincidences for orthogonal polarizations of the two signal fields $\mathcal{W}_{\perp}^{(4)}$ (i.e., in the absence of HOM). It is the sum of four possibilities of four-fold coincidences: Photons from MOT A registered on detectors D1, D2, and D3 and a photon from MOT B registered on detectors D4, photons from MOT B registered on detectors D1, D2, and D4 and a photon from MOT A registered on detectors D3, photons from MOT A registered on detectors D1 and D3 and photons from MOT B registered on detectors D2 and D4, and photons from MOT A registered on detectors D2 and D3 and photons from MOT B registered on detectors D1 and D4.

In Fig. 52 we plot $\mathcal{R}_{\parallel}^{(4)}/\mathcal{W}_{\perp}^{(4)}$ and $\mathcal{R}_{\perp}^{(4)}/\mathcal{W}_{\perp}^{(4)}$ along with the corresponding theoretical predictions. HOM interference is manifested in that $\mathcal{R}_{\parallel}^{(4)}/\mathcal{W}_{\perp}^{(4)} \to 0$ as $p_1 \to 0$. The highest observed visibility $V \equiv 1 - \mathcal{R}_{\parallel}^{(4)}/\mathcal{W}_{\perp}^{(4)} \approx 0.86 \pm 0.03$. As the theory and the experimental data agree within the statistical uncertainties, this indicates very good wave-packet overlap of the signals produced by the remote ensembles.

APPENDIX A

RUBIDIUM DATA

Table 5: Physical Property of Rubidium 85 [94]

Atomic Number	Z	37
Total nucleons	Z+N	85
Relative natural abundance	η	72.17(2)%
Nuclear Spin	I	5/2
Atomic Mass	m	84.911 789 732(14)u
Frequency D_1 line	ω_o	$2\pi\cdot$377.107 385690(46)THz
Frequency D_2 line	ω_o	$2\pi\cdot$384.230 406 373(14)THz
Vacuum wavelength D_2	λ_{D_2}	780.241 368 271(27)nm
Vacuum wavelength D_1	λ_{D_1}	794.979 014 933(96)nm
Lifetime $5^2P_{3/2}$	τ_{D_2}	26.2348(77)ns
Lifetime $5^2P_{1/2}$	τ_{D_1}	27.679(27)ns
Natural line width D_2	Γ_{D_2}	$2\pi\cdot$6.0666(18)MHz
Natural line width D_1	Γ_{D_1}	$2\pi\cdot$5.7500(56)MHz
Isotope shift of D_1	$\omega_o(^{85}Rb)$-$\omega_o(^{87}Rb)$	$2\pi\cdot$77.583(12)MHz
Isotope shift of D_2	$\omega_o(^{85}Rb)$-$\omega_o(^{87}Rb)$	$2\pi\cdot$78.095(12)MHz
Recoil Temperature D_1	T_r	356.86nK
Recoil Temperature D_2	T_r	370.47nK
Recoil Velocity D_1	v_r	5.9113 mm/s
Recoil Velocity D_2	v_r	6.0230 mm/s

Table 6: Physical Property of Rubidium 87 [94]

.

Atomic Number	Z	37
Total nucleons	Z+N	87
Relative natural abundance	η	27.83(2)%
Nuclear Spin	I	3/2
Atomic Mass	m	86.909180520(15)u
Frequency D_1 line	ω_o	$2\pi\cdot$377.107 463380(11)THz
Frequency D_2 line	ω_o	$2\pi\cdot$384.230 484 468 5(62)THz
Vacuum wavelength D_2	λ_{D_2}	780.241 209 686(13)nm
Vacuum wavelength D_1	λ_{D_1}	794.978 851 156(23)nm
Lifetime $5^2P_{3/2}$	τ_{D_2}	26.2348(77)ns
Lifetime $5^2P_{1/2}$	τ_{D_1}	27.679(27)ns
Natural line width D_2	Γ_{D_2}	$2\pi\cdot$6.0666(18)MHz
Natural line width D_1	Γ_{D_1}	$2\pi\cdot$5.7500(56)MHz
Isotope shift of D_1	$\omega_o(^{85}Rb)$-$\omega_o(^{87}Rb)$	$2\pi\cdot$77.583(12)MHz
Isotope shift of D_2	$\omega_o(^{85}Rb)$-$\omega_o(^{87}Rb)$	$2\pi\cdot$78.095(12)MHz
Recoil Temperature D_1	T_r	348.66nK
Recoil Temperature D_2	T_r	361.96nK
Recoil Velocity D_1	v_r	5.7754 mm/s
Recoil Velocity D_2	v_r	5.8845 mm/s

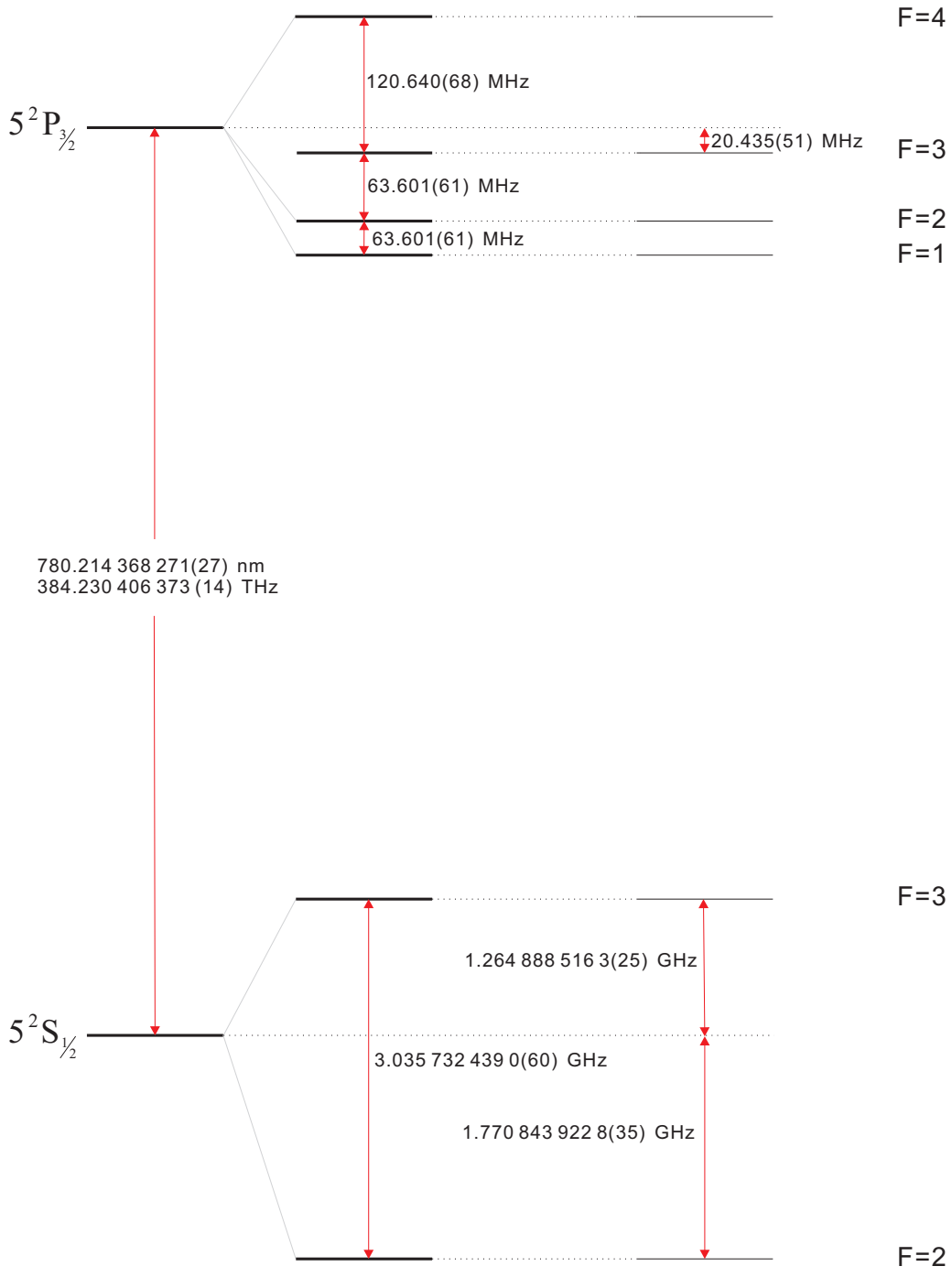

Figure 53: Rubidium 85 D_2 transition hyperfine structure, with frequency splittings between the hyperfine energy levels.

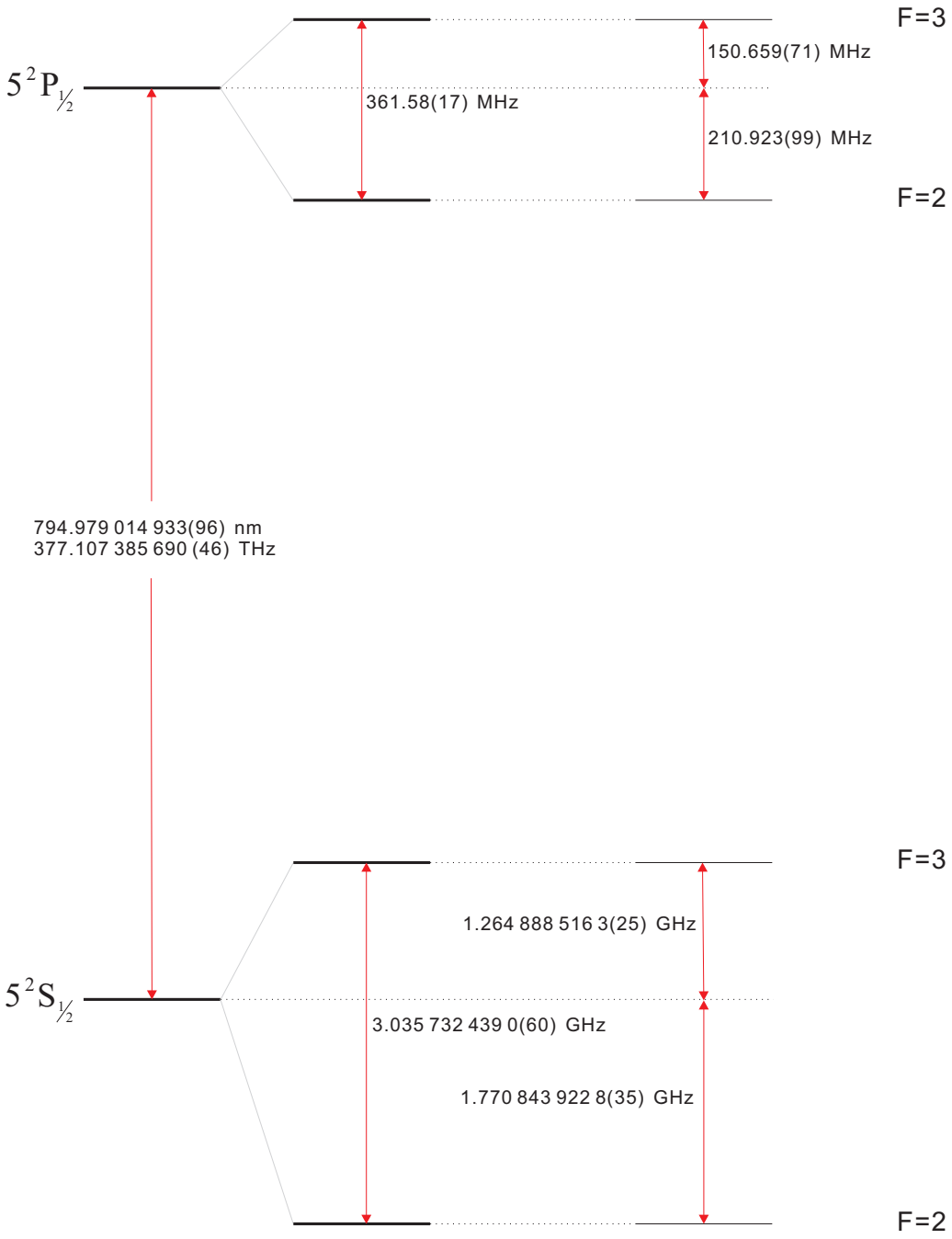

Figure 54: Rubidium 85 D_1 transition hyperfine structure, with frequency splittings between the hyperfine energy levels.

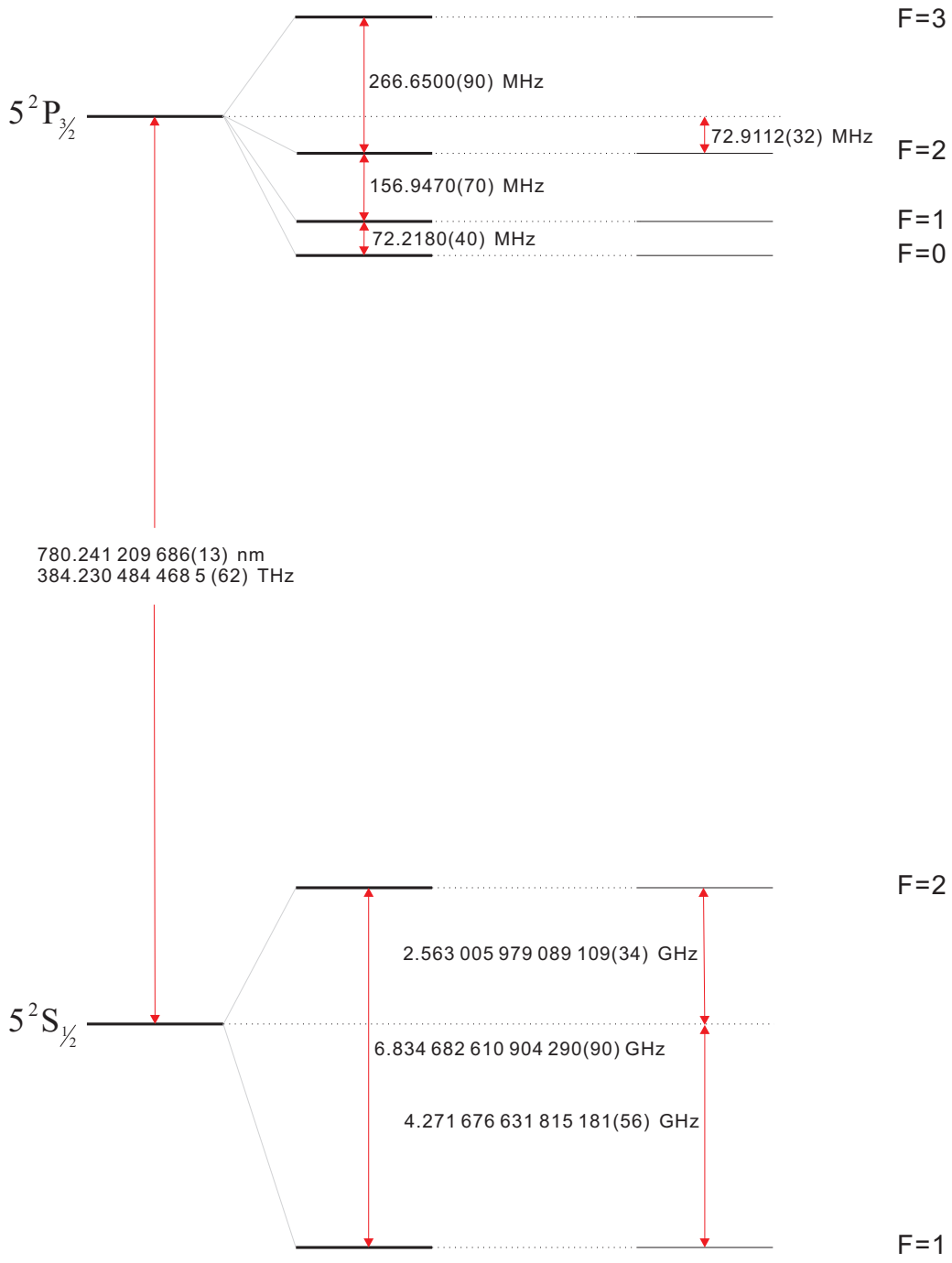

Figure 55: Rubidium 87 D_2 transition hyperfine structure, with frequency splittings between the hyperfine energy levels.

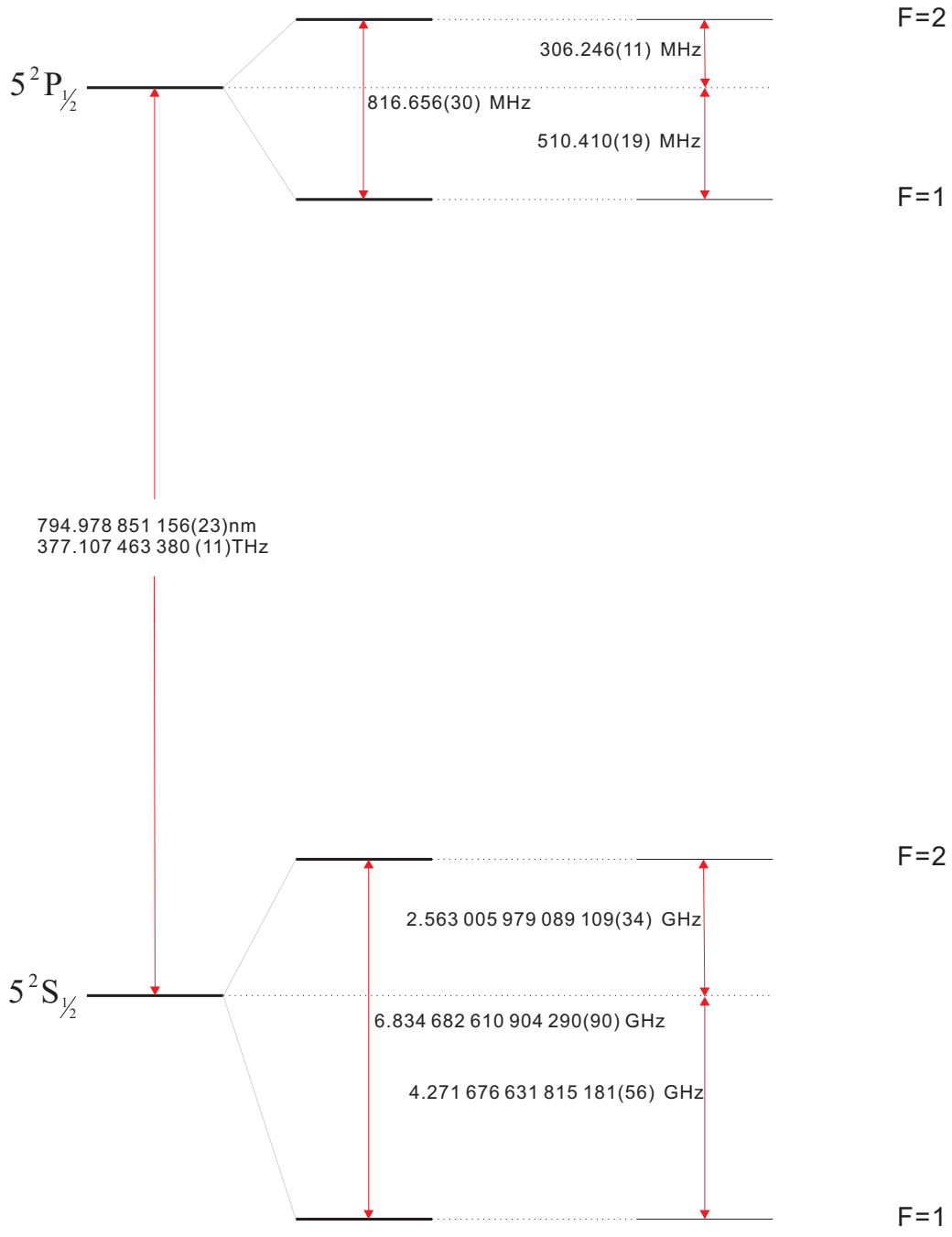

Figure 56: Rubidium 87 D_1 transition hyperfine structure, with frequency splittings between the hyperfine energy levels.

REFERENCES

[1] A. Einstein, B. Podolsky, and N. Rosen, "Can quantum-mechanical description of physical reality be considered complete?," *Phys. Rev.* **47**, 777 (1935).

[2] J. S. Bell, "On the Einstein-Podolsky-Rosen paradox," *Physics* **1**, 195 (1964).

[3] S.J. Freedman and J.F. Clauser, "Experimental test of local hidden-variable theories," *Phys. Rev. Lett.* **28**, 938 (1972).

[4] A. Aspect, P. Grangier, and G. Roger, "Experimental tests of realistic local theories via Bells theorem," *Phys. Rev. Lett.* **47**, 460 (1981).

[5] Z. Y. Ou and L. Mandel, "Violation of Bells inequality and classical probability in a two-photon correlation experiment," *Phys. Rev. Lett.* **61**, 50 (1988).

[6] Y. H. Shih and C. O. Alley, "New type of Einstein-Podolsky-Rosen-Bohm experiment using pairs of light quanta produced by optical parametric down conversion," *Phys. Rev. Lett.* **61**, 2921 (1988).

[7] S. D. Jenkins, D. N. Matsukevich, T. Chaneliere, S.-Y. Lan, T. A. B. Kennedy, and A. Kuzmich, "Quantum telecommunication with atomic ensembles," *JOSA B* **24**, 316 (2007).

[8] D. N. Matsukevich, P. Maunz, D. L. Moehring, S. Olmschenk, and C. Monroe, "Bell inequality violation with two remote atomic qubits," *Phys. Rev. Lett.* **100**, 150404 (2008).

[9] M. A. Rowe, D. Kielpinski, V. Meyer, C. A. Sackett, W. M. Itano, C. Monroe, and D. J. Wineland, "Experimental violation of a Bell's inequality with efficient detection," *Nature* **409**, 791 (2001).

[10] A. Aspect, P. Grangier, and G. Roger, "Experimental realization of Einstein-Podolsky-Rosen-Bohm gedankenexperiment : A new violation of Bells inequalities," *Phys. Rev. Lett.* **49**, 91 (1982).

[11] G. Weihs, T. Jennewein, C. Simon, H. Weinfurter, and A. Zeilinger, "Violation of Bells inequality under strict Einstein locality condition," *Phys. Rev. Lett.* **81**, 5039 (1998).

[12] C. Simon and W. T. M. Irvine, "Robust long-distance entanglement and a loophole-free Bell test with ions and photons," *Phys. Rev. Lett.* **91**, 110405 (2003).

[13] Michael A. Nielsen and Isaac L. Chuang, *Quantum Computation and Quantum Information* (Cambridge University Press, 2000).

[14] J. F. Clauser, M. A. Horne, A. Shimony, and R. A. Holt, "Proposed experiment to test local hidden-variable theories," *Phys. Rev. Lett.* **23**, 880 (1969).

[15] D. F. Walls and G. J. Milburn, *Quantum Optics* (Springer, 1994).

[16] R. A. Bertlmann and A. Zeilinger, editors, *Quantum [Un]speakables - From Bell to Quantum Information* (Springer, 2002).

[17] W. K. Wootters and W. H. Zurek, "A single quantum cannot be cloned," *Phys. Rev. Lett.* **299**, 802 (1982).

[18] C. H. Bennett and G. Brassard, in *Proceedings of the international conference on computers, systems and signal processing Indian Institute of Science*, Bangalore, India (1984).

[19] Corning Incorporated.

[20] A. Ekert, "Quantum Cryptography based on Bell's theorem," *Phys. Rev. Lett.* **67**, 661 (1991).

[21] D. Bouwmeester, J.-W. Pan, K. Mattle, M. Eibl, H. Weinfurter, and A. Zeilinger, "Experimental quantum teleportation," *Nature* **390**, 575 (1998).

[22] J.-W. Pan, D. Bouwmeester, H. Weinfurter, and A. Zeilinger, "Experimental entanglement swapping: Entangling photons that never interacted," *Phys. Rev. Lett.* **80**, 3891 (1998).

[23] S. L. Braunstein, A. Mann, and M. Revzen, "Maximal violation of Bell inequalities for mixed states," *Phys. Rev. Lett.* **68**, 3259 (1992).

[24] H.-J. Briegel, W. Dür, J. I. Cirac, and P. Zoller, "Quantum repeaters: The role of imperfect local operations in quantum communication," *Phys. Rev. Lett.* **81**, 5932 (1998).

[25] W. Dür, H.-J. Briegel, J. I. Cirac, and P. Zoller, "Quantum repeaters based on entanglement purification," *Phys. Rev. A* **59**, 169 (1999).

[26] L.-M. Duan, M. D. Lukin, J. I. Cirac, and P. Zoller, "Long-distance quantum communication with atomic ensembles and linear optics," *Nature* **414**, 413 (2001).

[27] C. Langer, R. Ozeri, J. D. Jost, J. Chiaverini, B. DeMarco, A. Ben-Kish, R. B. Blakestad, J. Britton, D. B. Hume, W. M. Itano, D. Leibfried, R. Reichle, T. Rosenband, T. Schaetz, P. O. Schmidt, and D. J. Wineland, "Long-lived qubit memory using atomic ions," *Phys. Rev. Lett.* **95**, 060502 (2005).

[28] D. Matsukevich and A. Kuzmich, "Quantum state transfer between matter and light," *Science* **306**, 663 (2004).

[29] V. Balić, D. A. Braje, P. Kolchin, G. Y. Yin, and S. E. Harris, "Generation of paired photons with controllable waveforms," *Phys. Rev. Lett.* **94**, 183601 (2005).

[30] D. N. Matsukevich, T. Chanelière, M. Bhattacharya, S.-Y. Lan, S. D. Jenkins, T. A. B. Kennedy, A. Kuzmich, "Entanglement of a photon and a collective atomic excitation," *Phys. Rev. Lett.* **95**, 040405 (2005).

[31] T. Chanelière, D. N. Matsukevich, S. D. Jenkins, S.-Y. Lan, T. A. B. Kennedy, and A. Kuzmich, "Storage and retrieval of single photons transmitted between remote quantum memories," *Nature* **438**, 833 (2005).

[32] D. N. Matsukevich, T. Chanelière, S. D. Jenkins, S.-Y. Lan, T. A. B. Kennedy, and A. Kuzmich, "Observation of dark state polariton collapses and revivals," *Phys. Rev. Lett.* **96**, 033601 (2006).

[33] S. D. Jenkins, D. N. Matsukevich, T. Chanelière, A. Kuzmich, and T. A. B. Kennedy, "Theory of dark-state polariton collapses and revivals," *Phys. Rev. A* **73**, 021803(R) (2006).

[34] M. Eisaman, A. Andre, F. Massou, M. Fleischhauer, A. S. Zibrov, and M. D. Lukin, "Electromagnetically induced transparency with tunable single-photon pulses," *Nature* **438**, 837 (2005).

[35] D. N. Matsukevich, T. Chanelière, S. D. Jenkins, S.-Y. Lan, T. Kennedy, and A. Kuzmich, "Entanglement of remote atomic qubits," *Phys. Rev. Lett.* **96**, 030405 (2006).

[36] T. Chanelière, D. N. Matsukevich, S. D. Jenkins, T. A. B. Kennedy, M. S. Chapman, and A. Kuzmich, "Quantum telecommunication based on atomic cascade transitions," *Phys. Rev. Lett.* **96**, 093604 (2006).

[37] D. N. Matsukevich, T. Chanelière, S. D. Jenkins, S.-Y. Lan, T. A. B. Kennedy, and A. Kuzmich, "Deterministic single photons via conditional quantum evolution," *Phys. Rev. Lett.* **97**, 013601 (2006).

[38] J. Thompson, J. Simon, H. Loh, and V. Vuletic, "A high-brightness source of narrowband, identical-photon pairs," *Science* **313**, 74 (2006).

[39] Y.-A. Chen, S. Chen, Z.-S. Yuan, B. Zhao, C.-S. Chuu, J. Schmiedmayer, and J.-W. Pan, "Memory-built-in quantum teleportation with photonic and atomic qubits," *Nature Physics* **4**, 103 (2008).

[40] Z.-S. Yuan, Y.-A. Chen, B. Zhao, S. Chen, J. Schmiedmayer, and J.-W. Pan, "Experimental demonstration of a BDCZ quantum repeater node," *Nature* **454**, 1089 (2008).

[41] D. L. Moehring, P. Maunz, S. Olmschenk, K. C. Younge, D. N. Matsukevich, L.-M. Duan, and C. Monroe, "Entanglement of single-atom quantum bits at a distance," *Nature* **449**, 68 (2007).

[42] E. Hagley, X. Maitre, G. Nogues, C. Wunderlich, M. Brune, J. M. Raimond, and S. Haroche, "Generation of Einstein-Pololsky-Rosen pairs of atoms," *Phys. Rev. Lett.* **79**, 1 (1997).

[43] J. Volz, M. Weber, D. Schlenk, W. Rosenfeld, J. Vrana, K. Saucke, C. Kurtsiefer, and H. Weinfurter, "Observation of entanglement of a single photon with a trapped atom," *Phys. Rev. Lett.* **96**, 030404 (2006).

[44] C. Simon, H. de Riedmatten, M. Afzelios, N. Sangouard, H. Zbinden, and N. Gisin, "Quantum repeaters with photon pair sources and multimode memories," *Phys. Rev. Lett.* **98**, 190503 (2007).

[45] R. H. Dicke, "Coherence in spontaneous radiation processes," *Phys. Rev.* **93**, 99 (1954).

[46] A. Kuzmich, K. Molmer, and E. S. Polzik, "Spin squeezing in an ensemble of atoms illuminated with squeezed light," *Phys. Rev. Lett.* **79**, 4782 (1997).

[47] R. Molmer, "Twin-correlations in atoms," *Eur. Phys. J. D* **5**, 301 (1999).

[48] G. Smith, S. Chaudhury, and P. Jessen, "Faraday spectroscopy in an optical lattice: a continuous probe of atom dynamics," *J.Opt. B: Quant. Semiclass. Opt.* **5**, 323 (2003).

[49] S. L. Braunstein and P. van Loock, "Quantum information with continuous variables," *Rev. Mod. Phys.* **77**, 513 (2005).

[50] A. Kuzmich and E. S. Polzik, "Atomic continuous variables processing and light-atoms quantum interface", in *Quantum information with continuous variables*, edited by S. L. Braunstein and A. K. Pati Kluwer 2003.

[51] M. Bajcsy, A. Zibrov, and M. D. Lukin, "Stationary pulses of light in an atomic medium," *Nature* **426**, 638 (2003).

[52] A. S. Zibrov, A. B. Matsko, O. Kocharovskaya, Y. V. Rostovtsev, G. R. Welch, and M. O. Scully, "Transporting and time reversing light via atomic coherence," *Phys. Rev. Lett.* **88**, 103601 (2002).

[53] D. F. Phillips, A. Fleischhauer, A. Mair, R. L. Walsworth, and M. D. Lukin, "Storage of light in atomic vapor," *Phys. Rev. Lett.* **86**, 783 (2001).

[54] C. Liu, Z. Dutton, C. H. Behroozi, and L. V. Hau, "Observation of coherent optical information storage in an atomic medium using halted light pulses," *Nature* **409**, 490 (2001).

[55] M. Johnsson and K.Molmer, "Storing quantum information in a solid using dark-state polaritons," *Phys. Rev. A.* **70**, 032320 (2004).

[56] M. Lukin, "Colloquium: Trapping and manipulating photon states in atomic ensembles," *Rev. Mod. Phys.* **75**, 457 (2003).

[57] S. E. Harris, "Electromagnetically induced transparency," *Physics Today* **50**, 36 (1997).

[58] M. Fleischhauer and M. D. Lukin, "Dark-State polaritons in electromagnetically induced transparency," *Phys. Rev. Lett.* **84**, 5094 (2000).

[59] S. D. Jenkins, *Theory of Light - Atomic Ensemble Interactions: Entanglement, Storage, and Retrieval*, PhD thesis Georgia Institute of Technology 2006.

[60] S. Chen, Y.-A. Chen, B. Zhao, Z.-S. Yuan, J. Schmiedmayer, and J.-W. Pan, "Demonstration of a stable atom-photon entanglement source for quantum repeaters," *Phys. Rev. Lett.* **99**, 180505 (2007).

[61] E. L. Raab, M. Prentiss, Alex Cable, Steven Chu, and D. E. Pritchard, "Trapping of neutral sodium atoms with radiation pressure," *Phys. Rev. Lett.* **59**, 2631 (1987).

[62] H. J. Metcalf and P. van der Straten, *Laser Cooling and Trapping* (Springer, 1999).

[63] A. E. Siegman, *Lasers* (University Science Books, 1986).

[64] S.-Y. Lan, S. D. Jenkins, T. Chanelière, D. N. Matsukevich, C. J. Campbell, R. Zhao, T. A. B. Kennedy, and A. Kuzmich, "Dual-species matter qubit entangled with light," *Phys. Rev. Lett.* **98**, 123602 (2007).

[65] G. D. Telles, L. G. Marcassa, S. R. Muniz, S. G. Miranda, A. Antunes, C. Westbrook, and V. S. Bagnato, "Inelastic cold collisions of a Na/Rb mixture in a magneto-optical trap," *Phys. Rev. A* **59**, 1 (1999).

[66] G. D. Telles, W. Garcia, L. G. Marcassa, V. S. Bagnato, D. Ciampini, M. Fazzi, J. H. Müller, D. Wilkowski, and E. Arimondo, "Trap loss in a two-species Rb-Cs magneto-optical trap," *Phys. Rev. A* **63**, 033406 (2001).

[67] V. Wippel, C. Binder, and L. Windholz, "Cross-section for collisions of ultracold ^{7}Li with Na," *Eur. Phys. J. D* **21**, 101 (2002).

[68] Sven Hensler, Axel Griesmaier, Jörg Werner, Axel Görlitz, and Tilman Pfau, "A two species trap for chromium and rubidium atoms," *Eur. Phys. J. D* **51**, 1807 (2004).

[69] A. G. Truscott, K. E. Strecker, W. I. McAlexander, G. B. Partridge, and R. G. Hulet, "Observation of Fermi pressure in a gas of trapped atoms," *Science* **291**, 2527 (2001).

[70] F. Schreck, L.Khaykovich, K. L.Corwin, G. Ferrari, T. Bourdel, J. Cubizolles, and C. Salomon, "A quasi-pure Bose-Einstein condensate immersed in a Fermi sea," *Phys. Rev. Lett.* **87**, 080403 (2001).

[71] S. Inouye, J. Goldwin, M. L. Olsen, C. Ticknor, J. L. Bohn, and D. S. Jin, "Observation of heteronuclear feshbach resonances in a mixture of bosons and fermions," *Phys. Rev. Lett.* **93**, 18 (2004).

[72] A. Yariv and D. M. Pepper, "Amplified reflection, phase conjugation, and oscillation in degenerate four-wave mixing," *Opt. Lett.* **1**, 16 (1977).

[73] D. A. Braje, V. Balić, S. Goda, G. Y. Yin, and S. E. Harris, "Frequency mixing using electromagnetically induced transparency in cold atoms," *Opt. Lett.* **93**, 183601 (2004).

[74] C. C. Davis, *Lasers and Electro-Optics : Fundamentals and Engineering* (Cambridge University Press, 1996).

[75] O. A. Collins, S. D. Jenkins, A. Kuzmich, and T. A. B. Kennedy, "Multiplexed memory-insensitive quantum repeaters," *Phys. Rev. Lett.* **98**, 060502 (2007).

[76] D. C. O'Shea, *Elements of Modern Optical Design* (John Wiley and Sons, 1985).

[77] Y.-A. Chen, S. Chen, Z.-S. Yuan, B. Zhao, C.-S. Chuu, Jörg Schmiedmayer, and J.-W. Pan, "Memory-built-in quantum teleportation with photonic and atomic qubits," *Nature Physics* **4**, 103 (2007).

[78] J. Simon, H. Tanji, S. Ghosh, and V. Vuletic, "Single- photon bus connecting spin-wave quantum memories," *Nature Physics* **3**, 765 (2007).

[79] J. Laurat, K. S. Choi, H. Deng, C. W. Chou, and H. J. Kimble, "Heralded entanglement between atomic ensembles: preparation, decoherence, and scaling," *Phys. Rev. Lett.* **99**, 180504 (2007).

[80] K. S. Choi, H. Deng, J. Laurat, and H. J. Kimble, "Mapping photonic entanglement into and out of a quantum memory," *Nature* **452**, 67 (2008).

[81] T. Isayama, Y. Takahashi, N. Tanaka, K. Toyoda, K. Ishikawa, and T. Yabuzaki, "Observation of Larmor spin precession of laser-cooled Rb atoms via paramagnetic Faraday rotation," *Phy. Rev. A* **59**, 4836 (1999).

[82] L. Jiang, J. M. Taylor, and M. D. Lukin, "Fast and robust approach to long-distance quantum communication with atomic ensembles," *Phys. Rev. A* **76**, 012301 (2007).

[83] B. Zhao, Z.-B. Chen, Y.-A. Chen, Jörg Schmiedmayer, and J.-W. Pan, "Robust Creation of Entanglement between Remote Memory Qubits," *Phys. Rev. Lett.* **98**, 240502 (2007).

[84] T. Chanelière, D. N. Matsukevich, S. D. Jenkins, S.-Y. Lan, R. Zhao, T. A. B. Kennedy, and A. Kuzmich, "Quantum interference of electromagnetic fields from remote quantum memories," *Phys. Rev. Lett.* **98**, 113602 (2007).

[85] E. Knill, R. Laflamme, and G. J. Milburn, "Quantum interference of electromagnetic fields from remote quantum memories," *Phys. Rev. Lett.* **409**, 46 (2001).

[86] C. K. Hong, Z. Y. Ou, and L. Mandel, "Measurement of subpicosecond time intervals between two photons by interference," *Phys. Rev. Lett.* **59**, 2044 (1987).

[87] L. Mandel and E. Wolf, *Optical Coherence and Quantum Optics* (Cambridge University Press, 1995).

[88] L. Mandel, "Quantum effects in one-photon and two-photon interference," *Rev. Mod. Phys.* **71**, S274 (1999).

[89] A. Zeilinger, "Experiment and the foundations of quantum physics," *Rev. Mod. Phys.* **71**, S288 (1999).

[90] C. Santori, D. Fattal, J. Vuckovic, G. S. Solomon, and Y. Yamamoto, "Indistinguishable photons from a single-photon device," *Nature* **410**, 594 (2002).

[91] T. Legero, T. Wilk, M. Hennrich, G. Rempe, and A. Kuhn, "Quantum beat of two single photons," *Phys. Rev. Lett.* **93**, 070503 (2004).

[92] J. Beugnon, M. Jones, J. Dingjan, B. Darquié, G. Messin, A. Browaeys, and P. Grangier, "Quantum interference between two single photons emitted by independently trapped atoms," *Nature* **440**, 779 (2006).

[93] P. Maunz, D. L. Moehring, S. Olmschenk, K. C. Younge, D. N. Matsukevich, and C. Monroe, "Quantum interference of photon pairs from two trapped atomic ions," *Nature Physics* **3**, 538 (2007).

[94] D. A. Steck, "Rubidium D Line Data," http://steck.us/alkalidata 2008.